2020

Mechanisms of Evasion: Anti-Tumor Immune Suppression & TRNA-Dependent Growth in Cancer Metastasis

Lisa Brooke Noble

MECHANISMS OF EVASION: ANTI-TUMOR IMMUNE SUPPRESSION & TRNA-DEPENDENT GROWTH IN CANCER METASTASIS

A Thesis Presented to the Faculty of

The Rockefeller University

in Partial Fulfillment of the Requirements for

the degree of Doctor of Philosophy

by

Lisa Brooke Noble

June 2020

MECHANISMS OF EVASION: ANTI-TUMOR IMMUNE SUPPRESSION & TRNA-DEPENDENT GROWTH IN CANCER METASTASIS

Lisa Brooke Noble, Ph.D.
The Rockefeller University 2020

Metastatic disease presents diverse therapeutic challenges for cancer patients, clinicians, and scientists. Cancer cells have developed sophisticated mechanisms of evasion to survive the selective pressures provided by the metastatic cascade. Two themes of success encompass modulating their surrounding microenvironment, or manipulating cell autonomous regulatory programs not intended for differentiated somatic cells. Both challenges are addressed in this body of work which focus on gastrointestinal and breast cancer metastasis. During cancer progression, tumour cells employ mechanisms that suppress both adaptive and innate immune responses. While our understanding of the molecular basis of adaptive immune suppression by cancer cells has led to the development of transformative immune checkpoint therapies, our knowledge of the molecular basis of innate immune suppression is less developed. Such innate immune suppressive mechanisms are thought to be especially active in gastrointestinal cancers—prevalent malignancies that are overall highly refractory to approved immune therapies. We describe an elegant molecular mechanism employed by pancreatic and colorectal cancer cells for repression of innate anti-tumour immunity. We observe that the creatine kinase brain-type (CKB) enzyme, which is over-expressed by colorectal cancer cells suppresses anti-tumor immunity. CKB localizes to the surface of cancer cells and can also be released into the extracellular space. This kinase enzymatically consumes extracellular ATP—a potent immune stimulatory Danger Associated Molecular Pattern (DAMP) molecule—from the tumor microenvironment. ATP hydrolysis by CKB generates ADP, an immune suppressive molecule. The action of this enzyme can thus concomitantly deplete an immune stimulatory molecule and generate an immune suppressive metabolite. Consistent with this, tumoral CKB suppresses dendritic cell activation, T-cell activation and B cell infiltration. Moreover, CKB suppresses immunity against primary and metastatic pancreatic tumors and impairs establishment of immunological anti-tumoral memory.

To uncover new modalities of cell autonomous regulation by cancer cells, in the midst of technical development to measure small RNA species, tRNAs have emerged as significant regulators of gene expression. The human genome contains 61 codons that are recognized by distinct transfer RNAs (tRNAs). We report the surprising observation that two isoacceptor tRNAs that decode synonymous codons become modulated in opposing directions during breast cancer progression. Specifically, $tRNA^{Ile}_{UAU}$ is upregulated whereas $tRNA^{Ile}_{GAU}$ is repressed as breast cancer cells attain enhanced metastatic capacity. $TRNA^{Ile}_{UAU}$ promoted and $tRNA^{Ile}_{GAU}$ suppressed metastatic colonization. These effects were mediated by codon-dependent translation of growth promoting or suppressing genes via cognate codon-dependent interactions. We also make the surprising observation that one isoleucyl tRNA can competitively impair translational decoding of synonymous codons by the other tRNA. Our findings uncover a specific isoacceptor tRNA pair that act in opposition—modulating distinct gene networks that contribute to an organismal phenotype. The degeneracy of the genetic code can thus be biologically exploited by human cancer cells via tRNA isoacceptor shifts and tRNA-mediated translational antagonism at the ribosome. Investigating fundamental cellular programs and tumor microenvironment interactions will enable more opportunity through knowledge to therapeutically target metastatic disease.

To patients & their families

ACKNOWLEDGMENTS

Firstly, I would like to thank and recognize my mentor Sohail Tavazoie for providing the opportunity for intellectual freedom and growth in his laboratory throughout my PhD. I would like to personally acknowledge and thank several members of the Tavazoie laboratory that were instrumental to the success of the studies discussed here – most significantly Doowon Huh and Benjamin Ostendorf. Hani Goodarzi was a significant mentor during my PhD studies, helping to conceive the tRNA project and constantly intellectually contributing through discussion and analysis of all high throughput sequencing experiments. I would like to thank Christopher Rouya and Doowon Huh for helpful discussions advice and technical assistance on the isoleucyl tRNA project. Importantly I would like to acknowledge all present and previous members of the Tavazoie laboratory that helped conduct or assist with experiments: Maria Liberti, Juliane Bräuer, who contributed significantly to the CKB project, and Dennis Hsu and Nandan Mandayam to the tRNA project. Ethan Weinberg, Hoang Ngyuen, Bernardo Tavora, Masoud Tavazoie, Zander Nguyen, and Nils Halberg - I would like to thank for their help in training me to perform *in vivo* experiments, namely all discussed xenograft and syngeneic experiments. I would like to extend recognition and gratitude to Alison Ashbrook in Charlie Rice's laboratory for teaching me how to do polysome profiling, and always having a great attitude! I would also like to acknowledge Benjamin Ostendorf, Bernardo Tavora, Masoud Tavazoie, Claudio Alarcon, Zander Nguyen and especially Jia Min Loo for discussions and advice regarding the CKB project throughout my studies. I greatly appreciate other members who were always willing to offer a helping hand in times of need, specifically Maria Passarelli, Hoang Nguyen, Ben Ostendorf, Ethan Weinberg, and Ilana Pollack. I would also like to thank those that spent time on parallel

efforts regarding tRNA studies, namely Robbie Myers & Logan Mendez. I would like to offer significant appreciation to Eiko Nishiuchi for ensuring a positive laboratory environment through organization and humor!

I would like to acknowledge the efforts of the Tri-Institutional MD PhD Program for their support and infrastructure, namely Olaf Andersen, Ruth Gotian, and the staff in the MD PhD office. I would like to thank the Rockefeller University Graduate School Dean's office for all of their help and guidance. I would like to thank my committee members – Sandy Simon, Paul Bienasz, and Luke Dow – for their comments, questions, and feedback over the years. I would also like to acknowledge Andy Minn for his time and efforts as an external examiner.

On a more personal note, I would like greatly acknowledge my family for their undeniable support and encouragement throughout the years. I would like to acknowledge my husband Nate Earnest for his understanding and encouragement, and his sense of humor – especially when being at the bench always takes at least 30 more minutes than you expect. I would like to thank my parents Stewart and Lydia Noble for teaching me to be brave resilient and curious, all characteristics that are necessary to undergo and complete a PhD. I would like to thank my brother Spencer Noble for always cheering me on, whose proximity always brought me comfort and made me feel like home. I would like to thank my friends and MD PhD peers, especially Raul Martinez-McFaline, Doowon Huh, Alexander Reinaldo Perez, and Jimmy Castellanos, for their support, reconciliation, scientific advice, and significant reminders to enjoy life outside of lab.

TABLE OF CONTENTS

LIST OF ILLUSTRATIONS

Chapter I

Chapter III

LIST OF FIGURES

Chapter II:

Chapter III:

LIST OF TABLES

Materials and Methods

Chapter I: Introduction

Gastrointestinal Cancer: Limited Therapeutic Options for Metastatic Disease

Colorectal cancer is a prevalent disease, with an estimated 145,600 new diagnosed cases in the United States this year. While early detection of colorectal cancer through colonoscopy has contributed to a decrease in mortality from colorectal cancer by 2.2% per year since 1990, the mortality caused by colorectal cancer remains the third most common cause of cancer death with 51, 020 deaths each year in the United States[1]. Pancreatic cancer is less common with 56,770 new diagnosed cases a year, but with 45,750 estimated deaths per year. One of the most significant causes of this persistence in mortality is the presence of metastatic disease at diagnosis, which is approximated as 22% of patients at the time of presentation in colorectal cancer, and 53% in pancreatic cancer. Therapeutic options for patients with metastatic gastrointestinal cancer include surgical resection of metastases localized to liver, or chemotherapy in non-resectable cases. The 5-year relative survival of patients with colorectal cancer Stage IV disease is 14.2%, and a mere 2.9% for pancreatic cancer patients with distant disease.

Therapeutic options for patients that present with metastatic disease from colorectal and pancreatic cancer with significant survival benefit remain limited. Treatment for the majority of patients with Stage IV metastatic colorectal or pancreatic cancer is mainly palliative and not curative. An increasing number of active chemotherapeutic agents now exist for nonoperable metastatic colorectal cancer, including irinotecan (a topoisomerase inhibitor), oxaliplatin, cetuximab and pantiumamb (monoclonal antibodies against epidermal growth factor receptor EGFR) and agents targeting vascular endothelial growth factor (VEGF) in addition to the standard of care treatment 5- fluoruracil (5-FU). While the recent emergence of targeted therapy has expanded therapeutic options for patients and increased the median survival benefit from 10-11 months with 5-FU to longer than three years[2], a rigorous combination and sequence of agents has not yet been

established. Pancreatic cancer patients with unresectable disease and normal bilirubin are now treated with a FOLFIRINOX (oxaliplatin, irinotecan, fluorouracil, and leucovorin) regimen with gemcitabine or gemcitabine plus nab-paclitaxel, as FOLFIRINOX treated patients in a clinical trial had a median overall survival of 11.1 months compared to 6.8 months on gemcitabine[3]. FOLFIRINOX treated patients do experience more toxicity, and patients with high bilirubin are treated with single agent therapy gemcitabine, which is mostly to increase clinical benefit and does not extend life more than six months. While targeted therapy has improved overall survival, they do require the appropriate stratification of patients that will respond to therapy. EGFR targeted therapy provides challenges in that tumors with amplifications and mutations in downstream signaling, most prominently KRAS, will not respond to therapy. As EGFR downstream signaling also interacts with other prominent molecular players, including p53, PTEN, PI3K, and BRAF, significant molecular testing is necessary to identify patients that will benefit from targeted therapy. Identification of patients with such mutations in metastatic lesions is practically challenging as biopsy of liver lesions is invasive and genetic testing remains expensive. Intra-tumoral heterogeneity within metastases can also prove difficult to stratify responders and non-responders[4]. Primary tumors are more accessible for testing as they are removed as polyps during colonoscopy, but the genetic heterogeneity of metastatic derivatives compared to the primary tumor is significant and results in inaccurate representation of the metastases from the primary tumor genotyping[5].

Surgical resection of liver metastases is one of the few treatments with a survival benefit. Surgical case series report that five-year survival rates after resection of metastatic disease range from 24-58% with an average of 40%[6-8], compared to 10-11% 5-year survival with systemic chemotherapy regimens[9]. The combination of chemotherapy and surgical

resection remains complicated as some chemotherapeutic agents cause liver toxicity and cases of perioperative morbidity have been reported[10].

The emerging immunotherapy drugs provide a new avenue of treatment, to instead focus on optimizing a patient's immune response to its tumor cells, instead of blasting cancer cells with chemotherapy (Figure 1.1). The initial therapies, known as checkpoint inhibitors, have shown remarkable responses in some patients, namely PD-1 inhibitors (pembrolizumab, nivolumab, cemiplimab), PD-L1 inhibitors (atezolizumab, avelumab, durvalumab) and a CTLA-4 blocking antibody (Ipilimumab). These drugs unleash already primed immunity against tumors. Patients that had successful responses to checkpoint blockade treatment had mounted an initial immune response against their tumors, but then faced blockade by PD-1 or other evasive molecular strategies on the tumor's behalf[11-13]. These endogenous mounted immune responses have been crucial to the success of current immunotherapies on the market, and promote a need to stratify tumor types based on their primed anti-tumour immune responses. The relative immunogenicity of a tumor is distinct for different tumor types and is dependent on multiple factors, including antigen diversity, the presence of neo-antigens (both driven by DNA damage and genomic instability of a tumor type), and the composition of the tumor microenvironment. Melanoma, one of the most responsive cancers to checkpoint inhibitors, has a very immunogenic profile, in terms of antigen diversity and mutational burden[14]. Colorectal and pancreatic cancers do not elicit such successful responses because they typically have low mutational burdens and have immunosuppressive microenvironments. The PD-1 inhibitor pembrolizumab has been tested in metastatic colorectal cancer patients and showed efficacy for mismatch repair (MMR) deficient

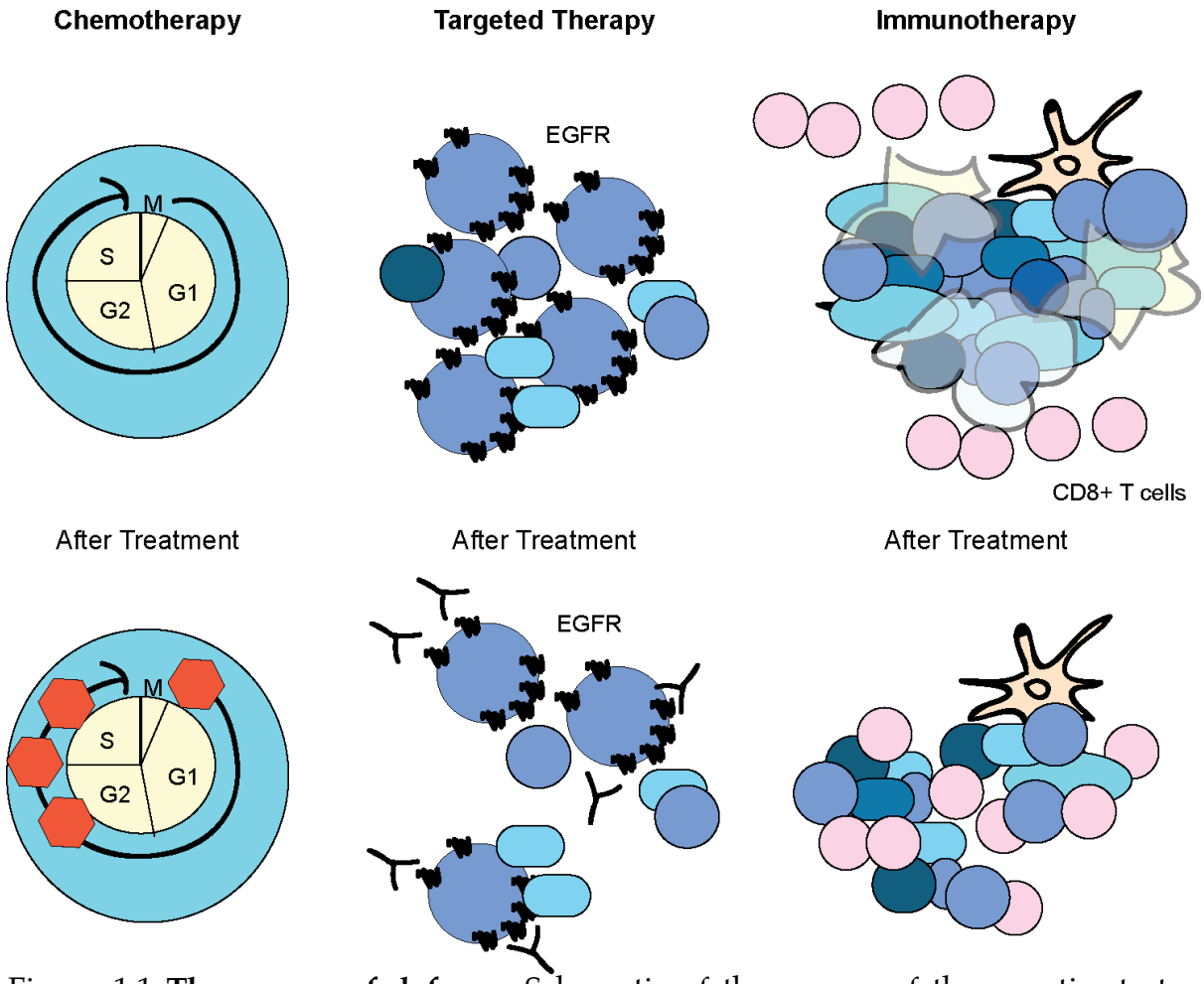

Figure 1.1 **Three arms of defense**. Schematic of three arms of therapeutic strategy – detailing the therapeutic goals of chemotherapy, targeting therapy, and immunotherapy.

tumors, with an immune-related progression-free survival rate of 78% (n=9). This small study is promising for MMR deficient cases, although no MMR proficient patients responded[15]. More recent studies have reported 30-50% response rates in microsatellite unstable/deficient mismatch repair colorectal cancer patients in clinical trials, and these immunotherapies are now FDA approved for treatment alone or in combination with anti-CTLA4 therapy. This has thought to be due to mismatch repair deficient tumors having a higher mutational burden, with more tumor-specific antigens for activated lymphocytes to target that wouldn't be silenced due to immune tolerance mechanisms. Pancreatic cancer has been extensively tested with checkpoint blockade

immunotherapies, such as anti PD-1 and anti-CTLA4, along with more sophisticated combinations, but unfortunately they have been largely unsuccessful at mounting an anti-tumor immune response that increases overall survival of patients in clinical trials[16]. Studies of the pancreatic cancer microenvironment have revealed from an early stage an immunosuppressive environment, comprised of type 2 macrophages (the pro-inflammatory or alternatively activated subtype), myeloid derived suppressor (MDSC) cells, and low levels of T cell infiltration[17]. Most pancreatic tumors also have low antigen diversity, or mutational burden. The few patients that have elicited long-term anti-tumour responses have been identified to have potent neo-antigens (i.e. MUC16) that have helped elicit T cell reactivity[18]. Some studies have developed a multi-step strategy and been successful in eliciting immune responses with checkpoint inhibitors and therapies that promote T-cell priming and activation, such as CD40 agonists combined with chemotherapy in an animal model[19]. Radiation therapy has been shown to increase immunogenic cell death of cancer cells that elicits myeloid recognition and CD8 T-cell priming and immunity in animal model studies[20]. Current efforts to combine immunotherapy with different regimens of radiotherapy are ongoing to determine whether this will be an effective strategy to activate both arms of the immune system[21,22]. More investigation into the composition of the tumor microenvironment and tumor mechanisms to evade immune detection and initiation of an immune response will be crucial to identifying and developing immunotherapies that will work in the clinic for gastrointestinal cancers.

Metastatic Breast Cancer: Clinical Challenges

Breast cancer is a very common disease in women, with 268,600 new diagnosed cases in the United States annually. Basic and clinical research of breast cancer has led to

enormous benefits for patients, through hormone stratification and subsequent therapy development and implementation. Many recently developed targeted therapies are very effective, such as trastuzumab for HER-2 positive patients. With increased screening and 62% of patients with localized disease at diagnosis, the 5-year survival rate of breast cancer is remarkably 89.9%. While only 6% of patients have distant disease at diagnosis, the survival rate for patients with late stage breast cancer is 27.4% with limited therapeutic options. Studies have demonstrated that overall survival of patients with metastatic breast cancer has improved over the past two decades and median overall survival approaches 2 years[23-25]. Many patients without good therapeutic options have breast cancer that is triple negative (hormone receptor ER and PR negative, and HER-2 negative) because these targeted therapies are not effective or applicable[26]. Patients with genetic BRCA mutations are treated with PARP inhibitors and see some benefit. Immunotherapy, specifically the inhibitor atezolizumab, is FDA approved and recommended in combination with the chemotherapeutic agent nab-paclitaxel for metastatic disease with positive PD-L1 expression, because the IMpassion 130 trial demonstrated statistically significant but relatively minimal benefit in overall survival (although patients with good intratumoral immune infiltration had a large OS benefit – 25 vs 15.5 months)[27]. Longer-term studies will demonstrate whether PD-1 inhibitors are effective in larger cohorts of patients with metastatic breast cancer. Chemotherapy remains the mainstay for metastatic triple negative breast cancer patients without PD-L1 expression, namely taxanes, capecitabine, or a combination regimen, depending on the patient's disease spread, previous treatment history and co-morbidities. Patients with diffuse metastatic disease, such as in lung metastasis, are treated with systemic chemotherapy. Further investigation of what drives metastatic triple negative breast

cancer will hopefully elucidate therapeutic targets for more effective treatments for future patients.

Metastatic Biology: Common Themes and Principles

Cancer cells face a significant number of diverse barriers to survive proliferate and colonize distant metastatic sites. These selective barriers, which include intravasation, survival in the circulation, extravasation, initiation and colonization of the end organ, and immune evasion, push malignancy to access molecular programs not intended for their cell of origin. While many conserved pathways highly mutated in human cancers that enable cancer cell proliferation and survival have been identified and are well studied (such as the Wnt/β-catenin EGFR/KRAS, MTOR, AKT, & PI3K pathways), some have been more elusive to target than initially anticipated (i.e. KRAS)[28-30]. Other mechanisms within the same targeted pathway arise quickly and manifest as resistance. Having multiple avenues of targeting tumors will hopefully enable overall better responses. Many unexpected mechanisms have been revealed utilizing screening methods, including whole genome CRISPR libraries, in different contexts and new biology is constantly being uncovered by studying how cancer cells increase their fitness[31,32]. One important tool has been in vivo selection, pioneered by Fidler, to enhance this selection of cancer cells in a mouse, mimicking the selective pressures of human disease[33]. This process of in vivo selection has been successful at identifying novel and robust regulators of the metastatic process[34-38]. Single cell RNA sequencing has illuminated how diverse and heterogeneous cancer cell populations are, and how this can lead to increased capability to metastasize[39]. Highlighted below are several avenues by which cancer cells have adapted to survive and flourish in a nutrient-poor microenvironment, surrounded

by a diverse set of cell types that could potentially be harmful or helpful. Pertinent to studies here include tumor-immune cell interactions and mechanisms of evasion and tolerance, as well as cell-autonomous phenotypes that are enhanced by molecular rigging of conserved regulatory programs driven via small RNA species.

Immune Evasion and the Tumor Microenvironment

A multitude of research is occurring to better understand the dynamics of the tumor microenvironment at early and late stages of disease. Tumor cells have been shown to secrete chemokines and cytokines that not only enable recruitment of immune cells but also alter their programming to enable cooperation in tumor growth. A tumor specific alteration of immature myeloid cells – myeloid derived suppressor cells (MDSCs) – have been characterized of two types, granulocytic and monocytic, that suppress a concerted anti-tumor immune response, and also have been shown to enable cancer cell proliferation, invasion and migration[40-42]. Altered programming of macrophages and fibroblasts has also been identified by tumor secreted factors, allowing tumor cells to benefit from the wound healing properties of these cell types, which actively secrete

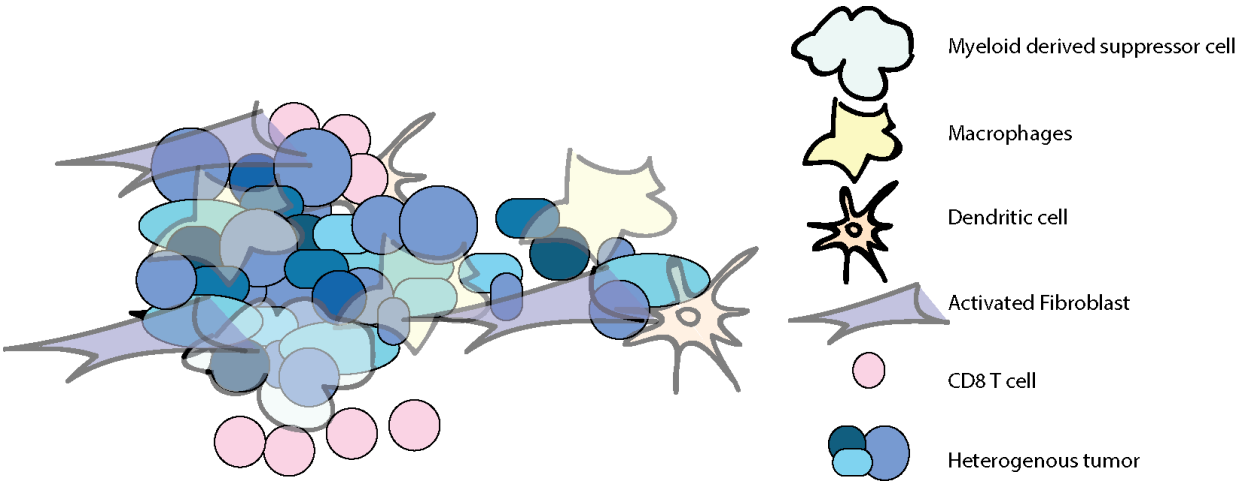

Figure 1.2. **A tumor suppressive microenvironment.**

growth factors that enable tumor growth and metastasis[43].

While cancer cells have been shown to manipulate innate immune cells to their advantage, there exists also many adaptions to evade recognition and activation of adaptive immunity. This evasive effort is compounded by tumor associated macrophages and MDSCs, which also work to suppress CD8+ T cell infiltration and anti-tumor immunity, utilizing PD-L1 and other mechanisms initially developed for tolerance to prevent auto-immunity. The concerted effort of an immunosuppressive tumor microenvironment is a difficult cycle to break, explaining why current immunotherapies, which focus on inhibiting one negative CD8+ T cell signal (PD-1 or PD-L1), are not effective in all patients. Studies that enable interruption of these tumor suppressive mechanisms are significant and hopefully will introduce a larger therapeutic window for immunotherapy. The LXR agonist, which promotes ApoE expression, was found to reduce survival of g-MDSCs in multiple tumor types, allowing for CD8+ T-cell activation[44].

Investigation of successful anti-tumor responses in patients and animal models has been just as elucidating. Particular subsets of dendritic cells – namely CD103+ - have been identified as the subset that most efficiently traffics and delivers tumor antigens to lymphocytes in the lymph node, enabling robust immune activation[45]. Strategies to increase expansion of CD103+ DCs in the context of PD-L1 therapy in animal models via FMS-like tyrosine kinase 3 ligand (FLT3L) administration had synergistic effects in melanoma models[46]. Optimal activation of CD103+ dendritic cells can occur after immunogenic cell death – a type of cell death that successfully allows secretion of ATP, a critical damage-associated molecular pattern receptor (DAMP), as well as IL-1β. Release

of the chromatin binding protein HMGB1 has also been found to elicit dendritic cell activation and antigen processing[47].

Common Themes of Metastatic Liver Colonization

For gastrointestinal cancer cells that successfully intravasate, the liver is one of first capillary beds cancer cells traveling in the venous circulation encounter via the portal circulation. The expression of several adhesion molecules such as the integrin family, and the chemokine ligand and receptor family, namely CCR6 and CXCR4, have been shown to have increased expression on metastatic colorectal cancer cells relative to primary tumors, and their expression negatively correlates with patient survival[48]. This aberrant secretion of chemokines not only enables colorectal cancer cells to home to metastatic distal organs, but also allows them to inappropriately communicate and stimulate immune cells and fibroblasts. Metabolic demand of disseminated colorectal cancer cells represents a key barrier to survival. The ability to harness metabolites from the tissue environment to increase survival provides a significant advantage for colorectal cancer cells arriving in the liver. Due to the nutrient depleted blood from the portal circulation and the efficiency by which hepatocytes import metabolites and oxygen, resources such as oxygen and pyruvate are at very low levels. Previous studies from our lab and others have demonstrated how cancer cells adapt to compensate for such metabolic demands and protect themselves from oxidative stress[49-51]. Nguyen and colleagues identified pyruvate kinase – liver and red blood cell type (PKLR) as a driver of colorectal cancer metastasis in a xenograft model, which increases glutathione levels to protect colorectal cancer cells from oxidative stress experienced under a combination of stresses that occur *in vivo*, namely high density, low glucose, and hypoxia[49].

Creatine Kinase Brain Promotes Gastrointestinal Metastasis

To identify key regulators of colorectal cancer progression at the prominent site of metastasis, the liver, two robust orthogonal approaches were taken. The KRAS mutant xenograft colorectal cancer line, LS-174T was in vivo selected by performing multiple rounds of intrahepatic injections and harvesting successful metastatic nodules that colonized the liver more efficiently than the previous round. Simultaneously, two distinct xenograft lines, WiDR and SW620, were transfected with a micro-RNA library and injected intrahepatically. Profiling of micro-RNAs of extracted tumors was conducted to identify differential micro-RNAs that could potentially play a role in metastatic progression. MiR-483-5p and miR-551a were silenced in the micro-RNA pool of extracted WiDR and SW620, as well as endogenously in the highly metastatic LS174T LVM3a and LVM3b in vivo selected lines compared to LS174T parental cells. Loss-of-function and gain-of-function experiments revealed that suppression of these micro-RNAs increased metastasis *in vivo* through intrasplenic injections of colorectal cancer xenografts in immunocompromised mice. MicroRNA inhibition was then found to affect metastatic colorectal cancer cell survival during the early phase of colonization using an *in vitro* liver organotypic slice culture system. Cleaved caspase 3/7 activity was used as a measure of apoptosis and survival. Transcriptomic profiling of CRC cells overexpressing miR-483-5p and miR-551a identified Creatine Kinase, Brain (CKB) as a downstream effector candidate. Mutagenesis and epistasis studies in vitro and in vivo studies revealed that CKB expression is regulated by miR-483-5p and miR-551a[52]. Loss-of-function via shRNA targeting and gain-of-function experiments of Creatine Kinase, Brain confirmed its role as a promoter of metastatic colorectal cancer cell survival under hypoxia conditions and in vivo metastasis assays.

The identification of a metabolic enzyme as an extracellular driver of metastatic colorectal cancer progression sheds significant light on the intense selective pressure within the liver microenvironment. Phosphocreatine and ATP levels were measured upon CKB knockdown and overexpression, confirming previously identified products of CKB's enzymatic activity in colorectal cancer cells. Cyclocreatine, a creatine kinase inhibitor that depletes phosphocreatine, was used in a pre-treatment metastasis study and found to significantly decrease metastatic colonization. The ability of colorectal cancer cells to utilize CKB to produce high-energy phosphocreatine was confusing, as ATP levels are depleted in colon cancer cells arriving in the liver nutrient poor[53-55]. Previous reports of extracellular ATP and high production of creatine by hepatocytes led to the hypothesis that CKB's survival advantage was localized in the extracellular space[56,57]. Indeed, CK-B was found to be secreted by western blot of conditioned media of colorectal cancer cells *in vitro*, as well as by western of the serum of tumor bearing mice. The possibility of CKB released by only apoptotic or dead cells was nullified by the expression of CK-B with a flag tag and a cleaved caspase domain (amino acid residues DEVD). The ability to harness metabolites from the tissue environment to increase survival would provide a significant advantage for colorectal cancer cells arriving in the liver. The creatine compound transporter SLC6A8 on metastatic colorectal cells that imports phosphocreatine into the cell was discovered to be downstream of CKB's extracellular activity. Stable knockdown of SLC6A8 reduced the survival advantage that Creatine Kinase Brain or pre- incubation with phosphocreatine provided under conditions of hypoxia *in vitro* and reduced liver metastasis *in vivo*. These findings implicate SLC6A8 to be downstream of CKB functionally.

CKB catalytic activity was also found to significantly decrease the local extracellular ATP concentration, measured by a luciferase reporter. While pre-incubation of cells with

phosphocreatine increases the survival of metastatic colorectal cancer cells *in vitro* and *in vivo*, phosphocreatine administration in the context of stable knockdown of CK-B rescues approximately half of metastatic capacity. We hypothesized there exists another biologically relevant phenotype caused by extracellular CK-B. The utilization of ATP by CK-B in the extracellular environment could benefit the cancer cells as small perturbations in extracellular ATP modulate the reactivity of immune cells. Extracellular ATP concentrations have been well documented to affect the activation states of immune cells and impact immune responses to cancer cells[58,59]. Further investigation of CKB in an immunocompetent system is warranted and a goal of this thesis work.

Small RNA Regulation of Breast Cancer Metastasis

By focusing studies on small RNAs that regulate a vast number of genes through downstream networks, evidence has revealed that breast cancer cells are able to easily direct whole concerted molecular programs to their advantage. In vivo selection of two independent triple negative breast cancer cell lines MDA-231 and CN34, and micro-RNA profiling, revealed that loss of miR-335 and miR-126 promote breast cancer colonization of the metastatic site the lung[60]. Downstream studies of targets of miR-335 and miR-126 revealed robust regulation of cellular phenotypes crucial to overcome physical barriers in lung metastasis, such as invasion and endothelial recruitment[38,60-66]. While micro-RNAs represent one type of small RNA that regulates downstream gene expression via RNA stability and translation, more expansive studies with small-RNA high throughput deep sequencing revealed other small RNA species that could regulate metastasis, i.e. fragments of tRNAs[67]. This non-canonical function of tRNA species is concordant with other studies that have found tRNA fragments to be generated in multiple species, and have specific roles in cell differentiation or stress responses[68-70]. Finding that such

phenotypes are dependent on tRNA fragments prompted study of full length and mature tRNAs in the in vivo selected breast cancer cell lines.

tRNAs have historically been difficult to quantify due to their heavy modifications and highly conserved secondary structure. These qualities make reverse transcription, the mainstay of sequencing strategies and efforts, inaccurate and unreliable for tRNA quantification, as reverse transcriptase will fall off of modified or bulky RNA structures. In recent years, multiple new technologies have been developed to overcome these obstacles, especially as preliminary studies suggest that codon-specific mature tRNA abundances are distinct in different contexts[71-73]. Probe based hybridization methods, specifically one developed in our laboratory, enable comparison between different cell types of many tRNA species through high throughput sequencing. Current methods focus on relative quantification of distinct tRNA species but it is still difficult to assess relative differences between tRNA species, due to technical constraints such as ligation or hybridization biases.

Transfer RNAs have long been considered static adaptor molecules playing the critical role of converting the genetic code to an amino acid code. Because of the degeneracy of the genetic code, multiple transfer RNAs (tRNAs) bearing distinct anticodons can accept a common amino acid for incorporation into the growing polypeptide chain during translation[74,75]. Such tRNA isoacceptors recognize 'synonymous codons'. The term 'synonymous codon' is ubiquitously used across biology, with major conceptual and practical implications for basic and disease studies. This static notion has been revised in recent years with observations of altered expression of tRNAs in the context of disease as well as demonstrated roles for certain over-expressed tRNAs in enhancing tumourigenic phenotypes[76,72]. tRNA abundances have also been found to differ significantly depending on cell type or cell state, i.e. proliferating or differentiated cells[72,76,77]. Analagous to these

observations, amino acid charging enzymes have also been shown to play non-canonical roles[78] and recent work has demonstrated significant cancer progression roles for specific charging enzymes[79,80]. Further experiments have shown that changes in tRNA abundance in poorly and highly metastatic breast cancer can have substantial effects on metastatic capacity of cancer cells through modulating the translation of downstream proteins that confer metastatic advantage *in vivo*[72]. These observations raise a number of questions including whether transcriptional deregulation in the absence of tRNA genomic copy number alterations can drive cancer progression as well as whether there exist metastasis suppressor tRNAs in human cancer. These findings unveil a new creative mechanism of increased cancer fitness, and most likely broadly apply among conserved cellular programs.

Chapter II: Modulation of Innate Immune Dynamics by Creatine Kinase Brain in Metastatic Gastrointestinal Cancer

CKB Promotes Adaptive Immune Dependent Tumor Progression

The metabolic enzyme Creatine Kinase Brain (CKB) was previously identified as a promoter of colorectal cancer metastatic colonization[52]. CKB was found to become over-expressed in human metastatic colorectal cancer as a result of silencing of two CKB-targeting microRNAs. Studies in immune-deficient mice revealed that CKB release from cancer cells promoted survival under hypoxia, an effect mediated by CKB phosphorylation of extracellular creatine to phosphocreatine. The phosphocreatine product was imported into cells and its gamma phosphate used to phosphorylate ADP to generate ATP - enabling survival during metabolic stress within the hepatic microenvironment. The finding that a kinase could be released from cells into the extracellular space and elicit phenotypic consequences raised a number of questions such as, whether CKB release is molecularly regulated or is simply a passive process, whether

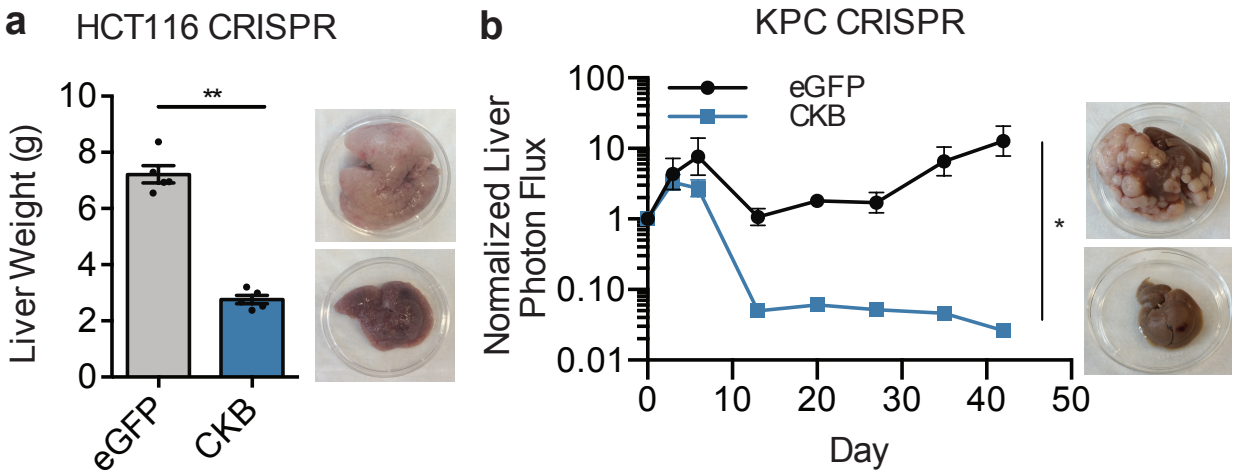

Figure 2.1 | **Genetic knockout of CKB via CRISPR reduces metastatic liver colonization.**
(a) Liver metastasis in mice injected with $5x10^5$ HCT116 cells into the portal circulation of immunocompromised NSG mice. Mice were euthanized at three weeks and livers were extracted for gross histology.
(b) Liver metastasis in mice injected with $5x10^5$ KPC cells into the portal circulation of immunocompetent B6129SF1/J mice. Mice were euthanized at 7 weeks and livers were extracted for gross histology. Unpaired Mann Whitney and 2-way ANOVA performed, p-value of $p<0.05$, $p<0.01$ indicated as *, **, respectively.

metabolic modulation of the extracellular space could have immunological consequences, and whether beyond cancer, CKB regulates organismal physiology. To begin to address these questions, we first employed genetic inactivation to determine the impact of complete CKB loss on colorectal cancer metastatic colonization.

CRISPR-Cas9-mediated targeting of CKB in the HCT116 human xenograft colorectal cancer cell line dramatically reduced liver metastatic colonization (267% reduction in liver weight)—largely precluding visualization of macroscopic nodules upon ex-vivo survey of livers (Fig. 2.1a).

To study the extent to which CKB interacts with the immune and tumor microenvironment in gastrointestinal cancer metastasis, we used the syngeneically transplantable KPC pancreatic cancer cell line, originally derived from a genetic model of KRAS/p53 mutant pancreatic cancer[81,82]. To avoid clonal drift, we used CRISPR-Cas9 to generate ten CKB KO clones, which were verified by western blot and re-pooled. KPC KO cells exhibited 480-fold reduced metastatic colonization capacity relative to control eGFP KO cells (Fig. 2.1b). Subcutaneous tumour growth studies revealed a similar robust suppression of progression in cells lacking CKB relative to control cells

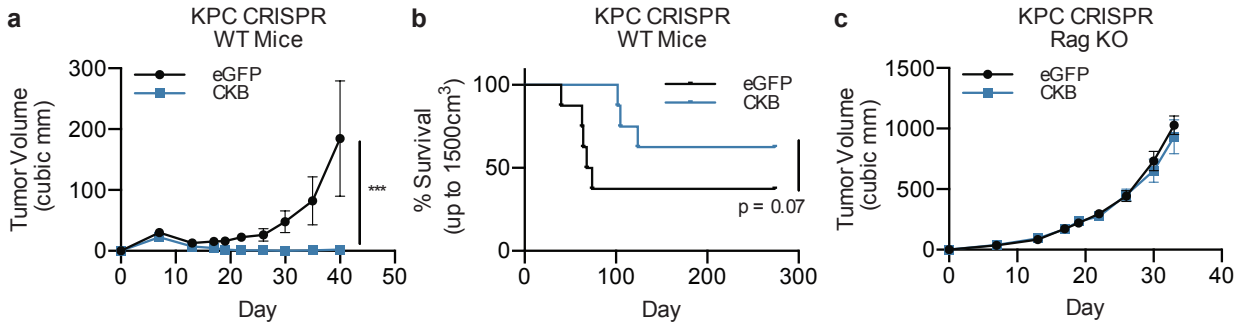

Figure 2.2 | **CKB tumour growth advantage is dependent on adaptive immunity.**
(a) Tumor growth from subcutaneous injections of either 1 million KPC CRISPR eGFP or CRISPR CKB KO cells in immunocompetent mice (n=8).
(b) Survival curves of mice injected in (a), with survival representing tumor volumes at a maximum of 1500cm^3 consistent with IACUC guidelines.
(c) Tumor growth from subcutaneous injections of either 1 million KPC CRISPR eGFP or CRISPR CKB KO cells in Rag KO mice (n=5). $p<0.001$ indicated as ***, 2-way ANOVA.

(Fig. 2.2a). This was associated with a separation of the plateau of the survival curve (p=0.07; Fig. 2.2b). Our prior studies had not revealed CKB to regulate growth at the primary tumour site in an immunodeficient model, suggesting the possibility of an immune-dependent effect of CKB on cancer progression. To directly test this, we implanted control or CKB KO KPC cells into Rag KO mice, which lack adaptive immunity. The reduced growth rate observed at the primary tumour site was completely abrogated in Rag KO mice, consistent with repression of cancer progression in CKB KO tumour-bearing mice being mediated by the adaptive immune response (Fig. 2.2c). Overexpression of CKB was sufficient to conversely promote primary tumor growth and metastatic colonization by KPC pancreatic cancer cells (Fig. 2.3a,b). These findings reveal CKB to be a robust driver of colorectal and pancreatic cancer progression and uncover an immune suppressive role for CKB during cancer progression.

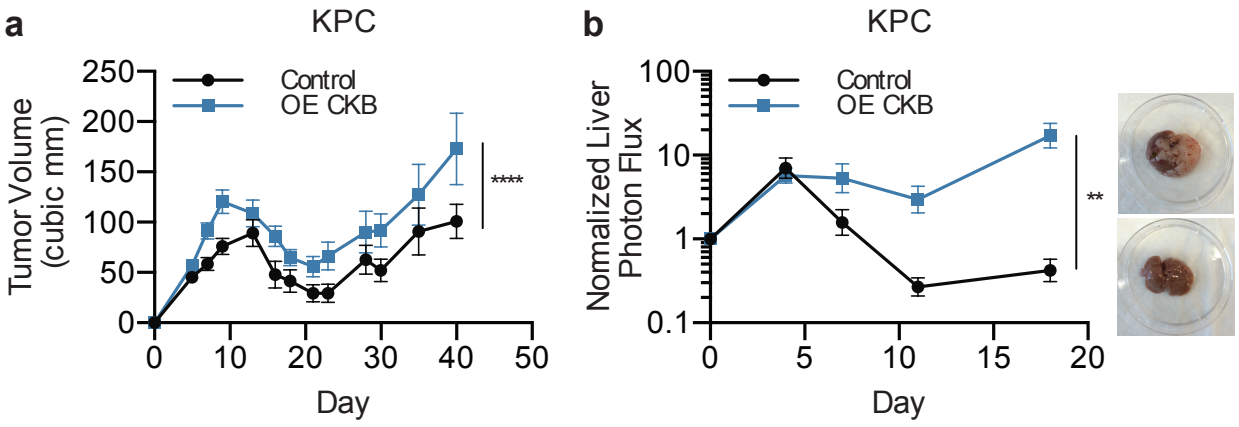

Figure 2.3 | **Overexpression of CKB in KPC cells increases primary tumor and metastatic growth.**
(a) Tumor growth from subcutaneous injections of either 1 million KPC control or OE CKB cells in immunocompetent mice (n=8).
(b) Liver metastasis in mice injected with $5x10^5$ KPC control or OE CKB cells into the portal circulation of immunocompetent B6129SF1/J mice. Mice were euthanized at three weeks and livers were extracted for gross histology. Two-way ANOVAs performed, p-values $p<0.01$, $p<0.001$ represented as **, ****, respectively.

CKB mediated shift in metabolites alters immune landscape

We next sought to determine the mechanism by which CKB modulates anti-tumour immunity. We previously demonstrated that metastatic colon cancer cells generate phosphocreatine in a CKB-dependent manner using extracellular ATP (approximated previously to be in the ~100uM range in the tumour microenvironment) and creatine (reported in the serum to be ~50-100uM)[52,56]. ATP is a DAMP that can potently activate immune cells[58,59,83,84]. Conversely, the product of ATP consumption, ADP and its hydrolyzed product adenosine are immunosuppressive. We hypothesized that CKB by consuming ATP may shift the extracellular ATP to ADP ratio and as such shift the balance from immune activation to immune suppression. To test this, we sought to measure extracellular concentrations of ATP and ADP from the circulation using metabolite profiling. Mice bearing CKB over-expressing tumours exhibited a marked reduction in circulating plasma ATP/ADP ratios relative to control mice (Fig. 2.4a). To determine if CKB can modulate ATP levels in the extracellular microenvironment of cancer cells in an

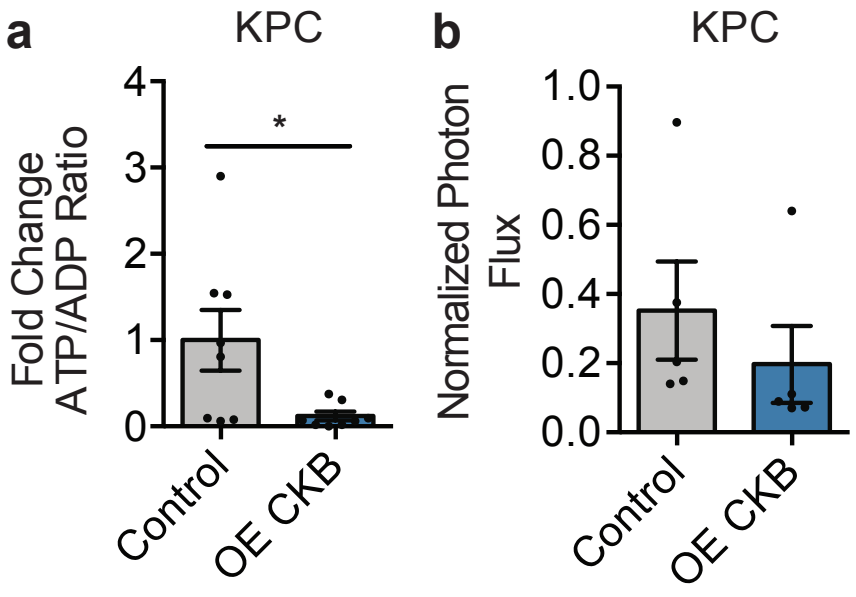

Figure 2.4 | **Extracellular ATP is depleted in KPC OE CKB bearing mice.** (a) ATP/ADP ratios from serum collected at Day 8 from tumor bearing mice with either KPC control or OE CKB metastatic liver nodules post intrasplenic injections. (b) Bioluminescence imaging of pME Luciferase transduced KPC Control or OE CKB metastatic livers on Day 8 (n=5-8 mice). Two-sided un-paired student's t-test performed, p-values represented * as $p<0.05$.

immune competent model, we transduced KPC cells with a plasma membrane anchored luciferase reporter[52,85]. CKB over-expression reduced the *in vivo* luciferase signal emanating from the surface of metastatic KPC cancer cells within the hepatic microenvironment upon CKB over-expression (Fig. 2.4b). We next sought to determine if this CKB-dependent metabolic shift impacts the activities or abundances of immune cells. Primary KPC tumours over-expressing CKB contained significantly less dendritic cells (DCs) relative to control tumours (Fig. 2.5a). Moreover, draining lymph nodes of CKB over-expressing tumours contained DCs that were less activated than control tumours, as assessed by reduced expression of CD86 and CD40 activation markers (Fig. 2.5b). These findings reveal that in the context of CKB-dependent ATP/ADP repression,

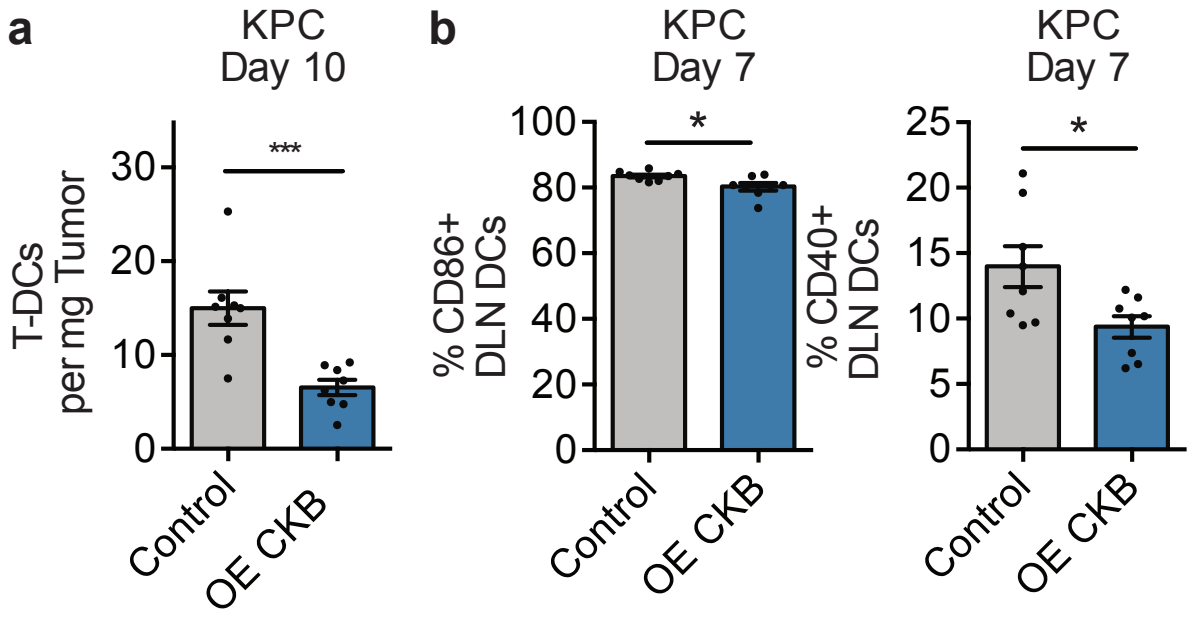

Figure 2.5 | **Dendritic cell infiltration and activation decreased with overexpression of CKB.**
(a) Quantification of dendritic cells infiltrating subcutaneous KPC control or OE CKB tumors extracted at Day 10, shown as number of DCs/mg tumor tissue.
(b) Dendritic cells in tumour draining lymph nodes with CD86+ and CD40+ expression, extracted at Day 7 (n=8 mice). Two-sided un-paired student's t-tests performed, p-values represented *, *** as $p<0.05$ and $p<0.001$, respectively.

DC activation becomes impaired. Dendritic cells are critical innate regulators of multiple immune cell types. We thus surveyed the tumoural abundance of various immune effector cells by flow-cytometry. Immune profiling revealed striking and coherent reductions in infiltrating T cells (both CD4+ and CD8+), NK cells, and B cells in CKB over-expressing tumours (Fig. 2.6a). *Ex vivo* stimulation of tumor infiltrating lymphocytes revealed reduced expression of anti-tumour effectors such as IFN-γ and Granzyme-B, as well as diminished markers of activation (CD69 and PD-1) on CD8+ tumour infiltrating T-cells (Fig. 2.6b). Conversely, KPC KO tumours implanted subcutaneously contained more migrating DCs in tumour draining lymph nodes (Fig. 2.7a), enhanced DC activation (CD86+ expression) (Fig. 2.7b) as well as reduced CD11b+ Ly6G+ myeloid cells (Fig. 2.7c),

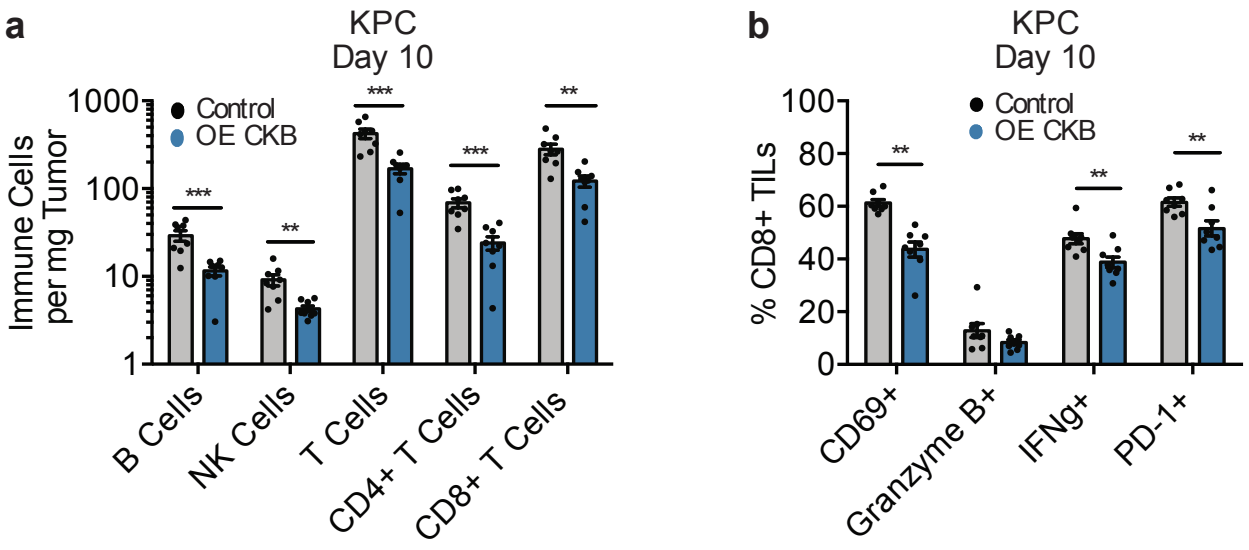

Figure 2.6 | **Overexpression of CKB downregulates adaptive infiltrating immune cells along with activation.**
(a) Quantification of adaptive immune infiltrating populations of subcutaneous KPC control or OE CKB tumors extracted at Day 10, shown as number of cell types/mg tumor tissue (n=8 mice).
(b) Activation markers of CD8+ T-cell tumor infiltrating lymphocytes as described in (a) post 2.5 hour ex vivo stimulation. Two-sided un-paired student's t-tests performed, p-values represented *, **, *** as $p<0.05$, $p<0.01$, and $p<0.001$, respectively.

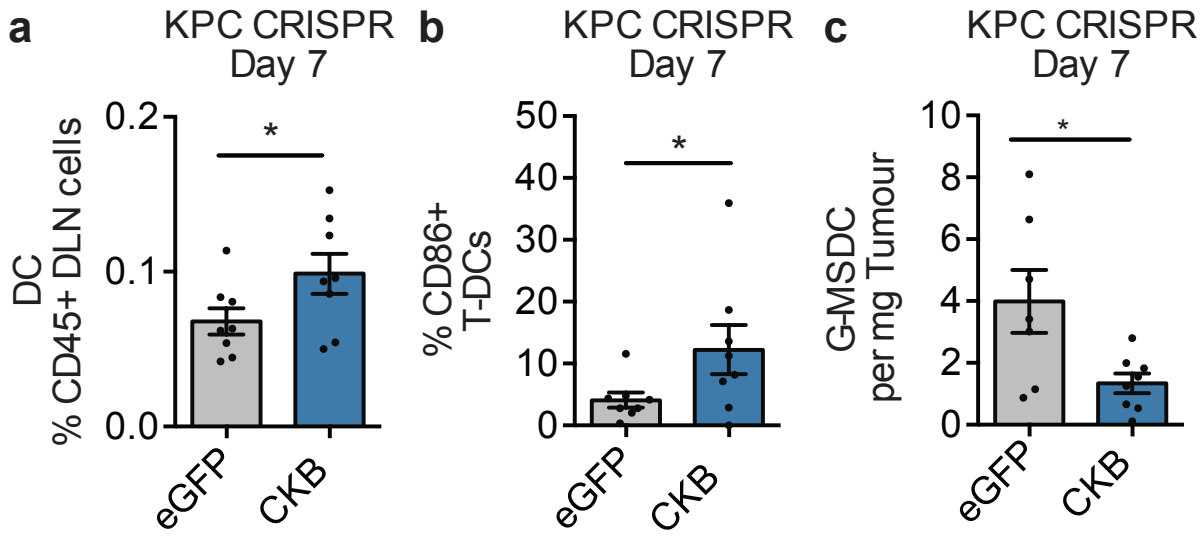

Figure 2.7 | **CKB Knockout tumors have increased dendritic cell activation and less suppressive infiltrates.**
(a) Quantification of dendritic cells present in tumor draining lymph nodes on Day 7.
(b) CD86+ expression of tumor infiltrating dendritic cells on Day 7 in KPC CRISPR eGFP or CKB tumors.
(c) Quantification of CD11b+ Ly6G+ granulocytic myeloid derived suppressor cells infiltrating subcutaneous KPC CRISPR eGFP or CKB tumors extracted at Day 7, shown as number of cells/mg tumor tissue (n=8 mice). Two-sided un-paired student's t-tests performed, p-values represented * as $p<0.05$.

which are known to be immunosuppressive. Collectively these findings reveal a CKB-mediated shift towards a suppressive anti-tumour immune profile. We next analyzed immune populations in the liver, the primary site of distal metastatic colonization by pancreatic and colorectal cancers. CD103+ DCs, the dendritic cell subpopulation that initiates CD8+ T cell anti-tumour immune responses[46], were significantly more abundant in the livers of CKB KO KPC tumor bearing mice relative to control livers (Fig. 2.8a). B cells were also more abundant in CKB KO livers relative to controls, demonstrating enhanced adaptive immune infiltration in metastatic liver nodules upon CKB inactivation (Fig. 2.8b). To determine if CKB mediates similar immune effects in an independent gastrointestinal cancer line, we generated CKB KO cells in MC38 murine colorectal cancer cells. MC38 CKB KO primary tumors grew significantly less efficiently

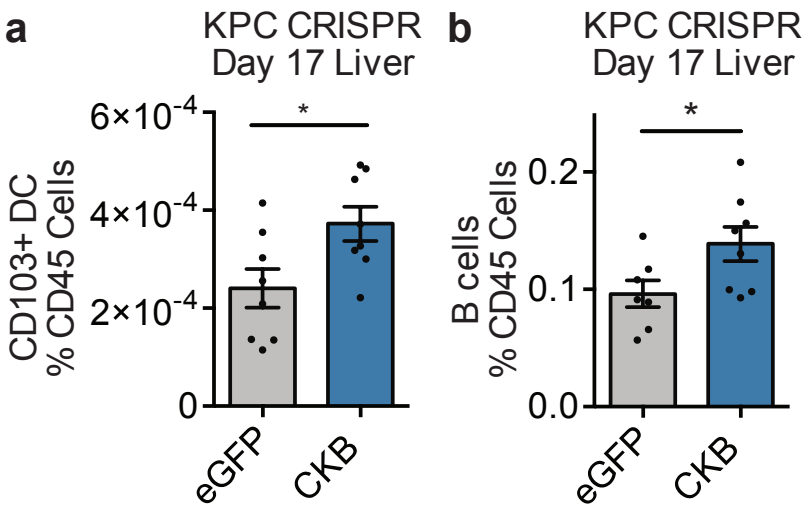

Figure 2.8 | **Immune infiltrates in KPC CRISPR CKB metastatic livers.** (a,b) Quantification of CD103+ dendritic cells (a) or B cells (b) in metastatic livers of mice intrasplenically injected with KPC CRISPR eGFP or CKB cells, extracted on Day 17. Two-sided un-paired student's t-tests performed, p-values represented * as $p<0.05$.

at the subcutaneous site than control tumors (Fig 2.9a,b). Consistent with this, MC38 CKB KO tumors contained significantly enhanced immune infiltration (CD45+ cells) relative to control tumors (Fig. 2.9c), enhanced CD103+ DC infiltration and reduced abundance of CD11b+ Ly6G+ myeloid suppressive cells (Fig. 2.9d), and greater activation of CD8+ TILs (Fig. 2.9e-f). These findings reveal that CKB broadly shifts the immune profiles of colorectal and pancreatic cancers at the primary and metastatic sites towards a repressed state that favors cancer progression.

To investigate whether CKB's extracellular activity directly regulates immune cell activation, we conducted in vitro studies using conditioned media from HCT116 human colorectal cells, which over-express CKB, as well as isogenic HCT116 CKB KO cells. Bone marrow derived DCs cultured with conditioned media from colon cancer cells expressing CKB were less activated than bone marrow derived DCs conditioned with CKB KO conditioned media (Fig. 2.10a). IL-12 is a key cytokine secreted by dendritic cells and known to be induced by extracellular ATP[86]. CKB KO conditioned media significantly enhanced IL-12 expression in DCs relative to control conditioned media (Fig. 2.10b).

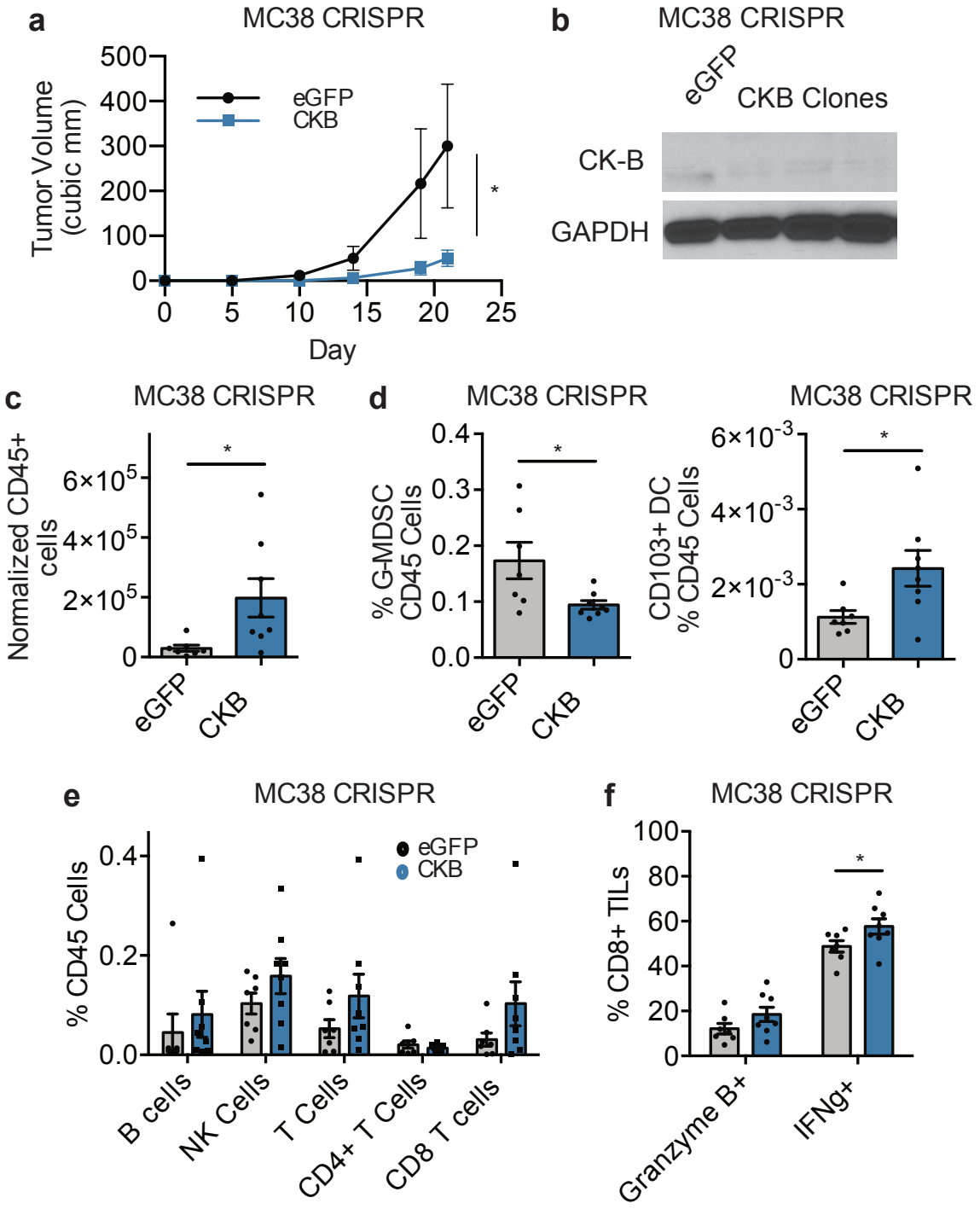

Figure 2.9 | **MC38 CRISPR CKB tumors demonstrate enhanced anti-tumor immunity via increased anti-tumour myeloid and adaptive immune infiltration.**
(a) Tumor growth from subcutaneous injections of either 1 million MC38 CRISPR eGFP or CRISPR CKB KO cells in immunocompetent mice (n=8).
(b) Representative Western blot of MC38 eGFP or CRISPR CKB clones.
(c) Quantification of all immune CD45+ tumor infiltrates normalized to tumor volume of MC38 CRISPR eGFP or CKB tumors extracted on Day 21.

(d) Quantification of CD11b+ Ly6G+ granulocytic myeloid derived suppressor cells and CD103+ dendritic cells infiltrating subcutaneous MC38 CRISPR eGFP or CKB tumors extracted at Day 21, represented as % CD45 cells.
(e) Quantification of adaptive immune infiltrating populations of subcutaneous MC38 CRISPR eGFP or CKB tumors extracted at Day 21, shown as % CD45 cells.
(f) Activation markers of CD8+ T-cell tumor infiltrating lymphocytes as described in (c) post 2.5 hour ex vivo stimulation. Two-sided un-paired student's t-tests performed, p-values represented * as $p<0.05$.

Rescuing CKB expression in KO cells repressed DC IL-12 levels to a level comparable to control conditioned media (Fig. 2.10b). Finally, expression of the N-terminus deletion of CKB in CKB KO cells, which blocks its extracellularization, as described below, enhanced DC IL-12 expression to a level comparable to CKB deletion. These findings reveal that extracellular CKB impairs activation of DCs, key innate regulators of immunity.

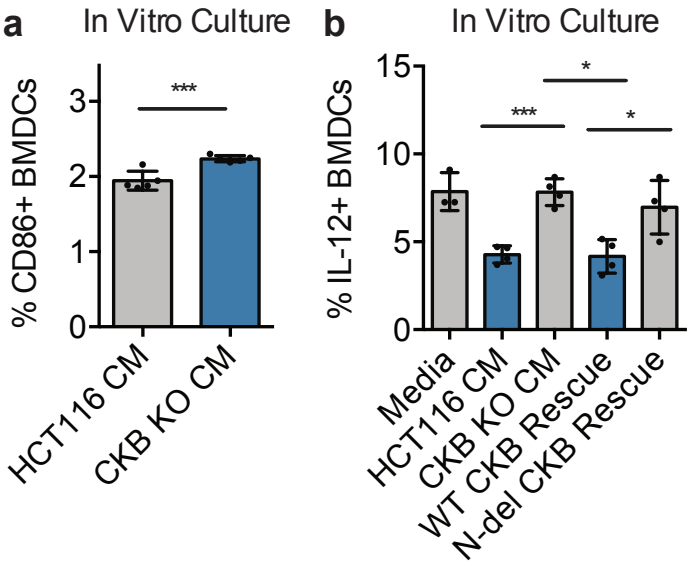

Figure 2.10 | **Bone marrow derived dendritic cells (DCs) show increased activation with CKB KO conditioned media *in vitro*.**
(a) CD86+ expression of BMDCs after 8 days culture and 24 hours incubation with HCT116 conditioned media (n=5). (b) IL-12+ expression of BMDCs after 8 days of culture post incubation with HCT116 conditioned media and 4 hours incubation of Brefeldin A treatment.
Two-sided un-paired student's t-tests performed, p-values represented *, **, *** as $p<0.05$, $p<0.01$, and $p<0.001$, respectively.

To understand whether these changes in a broad anti-tumour immune profile can impart a sustained memory response to future tumour challenge, mice were injected with KPC CRISPR CKB KO cells either at the metastatic site or subcutaneously. As previously observed (Figs. 2.1 & 2.2), these CKB deficient tumours regressed. These mice were then re-challenged at the same sites with primary or metastatic KPC Parental tumours, a more aggressive and heterogenous population than the CKB KO population. In both cases, the

re-challenged mice exhibited substantially reduced tumour (8.5-fold reduction) and metastatic (36.5-fold reduction) progression relative to naïve mice (Fig. 2.11a-b). These findings demonstrate a robust CKB-dependent regulation of anti-tumour immunological memory response at the primary and metastatic sites by a gastrointestinal malignancy.

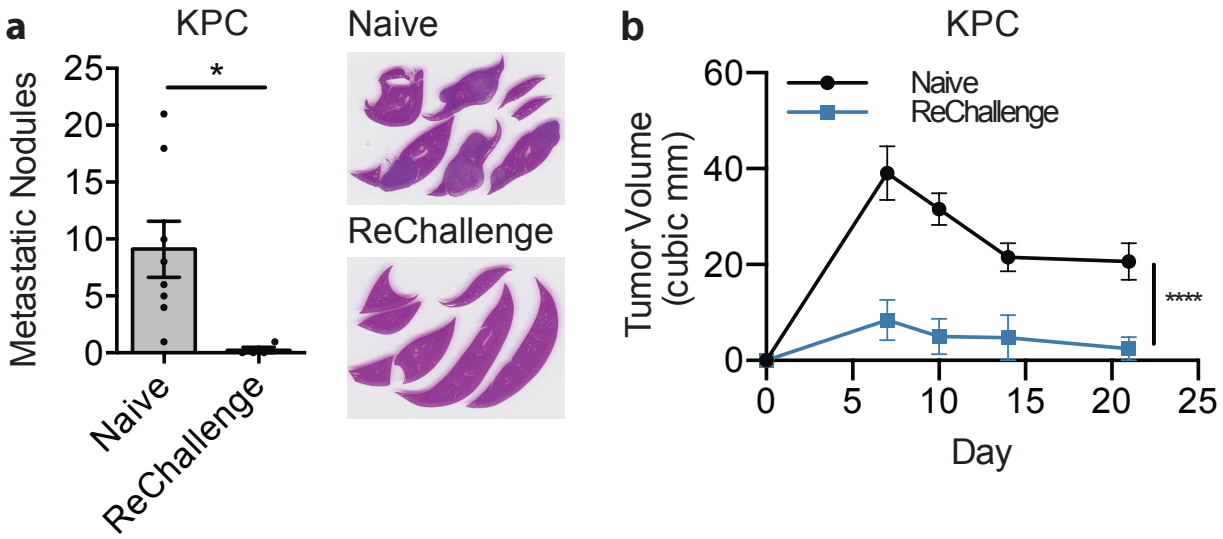

Figure 2.11 | **Successful re-challenge with KPC wildtype cells demonstrates KPC CRISPR CKB regression elicits long-term and sustained anti-tumour memory response**.
(a) Quantification of H&E histology of liver metastasis in mice injected with $2.5x10^5$ KPC Parental cells into the portal circulation of either naïve or mice previously injected with KPC CRISPR CKB cells intrasplenically 50 days prior which regressed. Mice were euthanized at nine weeks and livers were extracted for gross histology (n=4-8 mice).
(b) Tumor growth from subcutaneous injections of 1 million KPC Parental cells in either naïve or mice previously injected with KPC CRISPR CKB cells subcutaneously which regressed. Two-way unpaired student's's t-test and 2-way ANOVA performed, p-value of *, **** indicated as $p<0.05$, $p<0.0001$, respectively.

The N-terminus of CKB enables extracellular secretion mediated by phosphatidylserine+ ectosomes

We next sought to better understand the mechanism by which CKB accesses the extracellular space as a means of selectively impairing its extracellular function. CKB lacks a classic secretory signal. Moreover, inhibiting secretion with Brefeldin A did not inhibit CKB release into the conditioned media, excluding golgi-mediated secretion as a

potential pathway[87]. We hypothesized the CKB might be released via extracellular vesicles. Two major vesicle types have been increasingly characterized, with distinct biological mechanisms of formation. Exosomes are small vesicles (50-100 nm in diameter) that are formed within multivesicular bodies as part of the endosomal-lysosomal pathway. In contrast, ectosomes, also known as microvesicles, are larger (100-350 nm in diameter) vesicles that are directly generated from plasma membrane budding[88]. Ectosomes, being larger are unstable and can burst—releasing intracellular and membrane bound contents extracellularly. We transfected colon cancer cells with a construct expressing an N-terminal Flag tag, fused to a devd caspase cleavage motif cloned upstream of CKB[52]. The devd motif is cleavable by caspases that become activated in apoptotic cells. As such, apoptotic-cell derived CKB would lose its Flag tag via caspase-dependent cleavage, ensuring that visualized CKB is that arising from non-apoptotic cells. Immunofluorescence microscopy revealed substantial concentrated staining of Flag

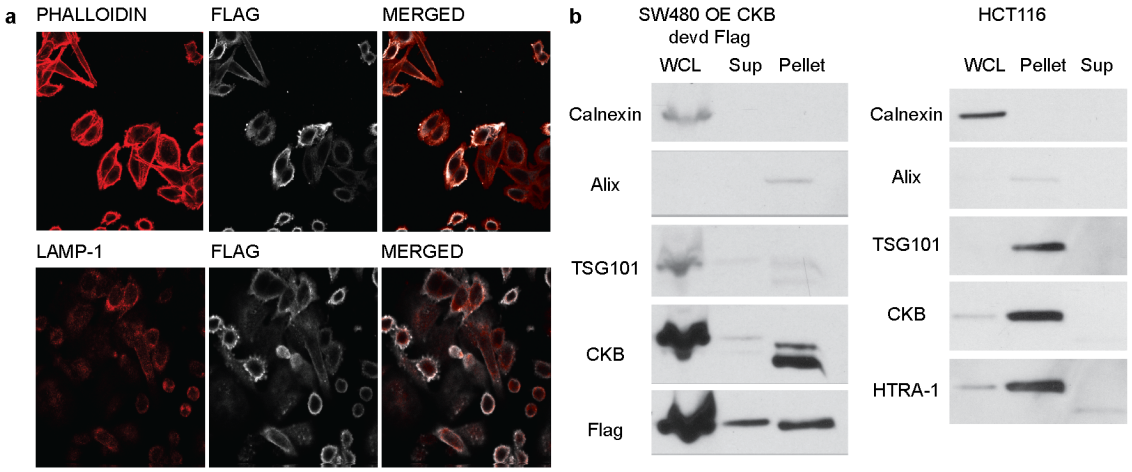

Figure 2.12 | **CKB localizes to plasma membrane and is concentrated in extracellular vesicles.**
(a) SW480 cells overexpressing CK-B with a DEVD domain and Flag tag were stained with Phalloidin in red and Flag in white (top). LAMP-1, a late endosomal marker, is in red in the bottom panel.
(b) Western blots of extracellular vesicle isolates from SW480 OE CK-B devd Flag and HCT116 cell lines.

tagged devd CKB at the plasma membrane of SW480 colorectal cancer cells, suggesting ectosomes as a potential mechanism of extracellularization and release. CKB co-localized with Phalloidin, a specific marker of F- actin but not with LAMP-1, an early lysosomal marker. These findings suggest ectosomes as carriers of CKB (Fig. 2.12a). Past studies have identified the externalization of phosphatidylserine and phosphatidylelanine on the surface of budding and formed ectosomes[89-92]. Such externalization has been observed in the absence of apoptosis. In contrast, exosomes are released into the extracellular space from within multivesicular bodies. While a multivesicular body must incorporate into the plasma membrane and manipulate its curvature, exosomes retain their structure and do not perturb their membrane by exposing phosphatidylserine. We next isolated extracellular vesicles from concentrated supernatant from colon cancer cells overexpressing CKB devd FLAG using a dehydrating agent. Isolation of vesicles was confirmed by western Blotting for vesicle contained proteins such as TSG101, a member of the ESCRT machinery, and Alix (PDCD6IP), a known accessory protein (Fig. 2.12b). To biochemically isolate ectosomes, we used Annexin V, a phosphatidylserine-binding protein, conjugated to biotin, to target selectively target phosphatidylserine on the surface of ectosomes (Fig. 2.13a). Western blot of phosphatidylserine positive purified vesicles revealed the presence of endogenous CKB (Fig. 2.13b). Moreover, unbiased mass spectrometry of these phosphatidylserine positive vesicles confirmed presence of endogenous CKB as well as gene set enrichment of extracellular vesicle-associated proteins (Fig. 2.13c-d). We next sought to determine if CKB is contained within ectosomes or whether it is present on the surface of these structures. Immunofluorescent staining without permeabilization of SW480 colorectal cancer cells expressing Flag-devd tagged and HCT116 cells expressing CKB revealed CKB localization on the extracellular surface of the plasma membrane (Fig. 2.14a). Plasma membrane CKB co-localized with

phosphatidylserine, as assessed by staining for its binding partner Annexin V, again suggesting ectosomal localization of CKB. To confirm this finding on live cells, we

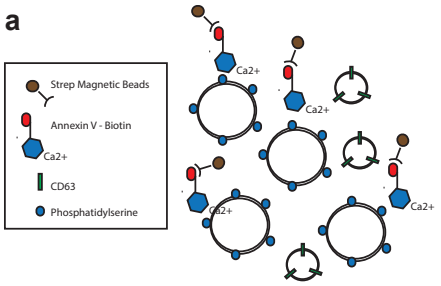

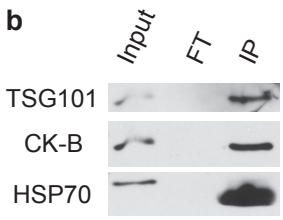

c Genes Enriched

Galectin-3-binding protein LG3BP
Actin, cytoplasmic 1 ACTB
Actin, cytoplasmic 2 ACTG
Isoform 2 of Nucleophosmin NPM
Protein S100-A6 S10A6
Actin, alpha cardiac muscle 1 OS ACTC
Heat shock protein HSP 90-alpha HS90A
Heat shock protein HSP 90-beta HS90B]
Creatine kinase B-type CKB

d

GO Term	Fold Enrichment	P-Value
Extracellular Membrane-Bounded Organelle	4.88	4.95E-133
Extracellular Vesicle	4.85	1.71E-132
Membrane-bound Vesicle	4.06	2.54E-122
Vesicle	3.93	2.67E-118

Figure 2.13 | **Purification of Ectosomes using Phosphatidylserine.**
(a) Schematic of purification strategy. Annexin V – Biotin conjugate is bound to Phosphatidylserine in a calcium dependent manner. Streptavidin magnetic beads are then used to isolate ectosomes from surrounding exosomes.
(b) Western Blot with 30% Input, Flow Through, and Immunoprecipitation of Phosphatidylserine, showing TSG101 as an expected member of ectosomes, CK-B, and other cytoplasmic proteins known to accumulate in ectosomes. 30ug Isolated Vesicles were used as starting material.
(c,d) Genes enriched in mass spectrometry of isolated vesicles (c) and subsequent GO term analysis (d).

performed Imagestream flow cytometric imaging to assess the localization of CKB on the extracellular membranes of non-fixed cells. Live imaging revealed endogenous CKB to be expressed on the extracellular surface of HCT116 colon cancer cells as well as on the surface of large ectosome-appearing vesicles (Fig. 2.14b). To determine if CKB is also localized on the exposed membrane of isolated vesicles, protease experiments were conducted. CKB levels reduced dramatically upon trypsin treatment as assessed by

Western blotting of isolated vesicles from SW480 cells (Fig. 2.14c), suggesting localization of CKB on the extracellular surface of vesicles. These findings reveal that CKB localizes

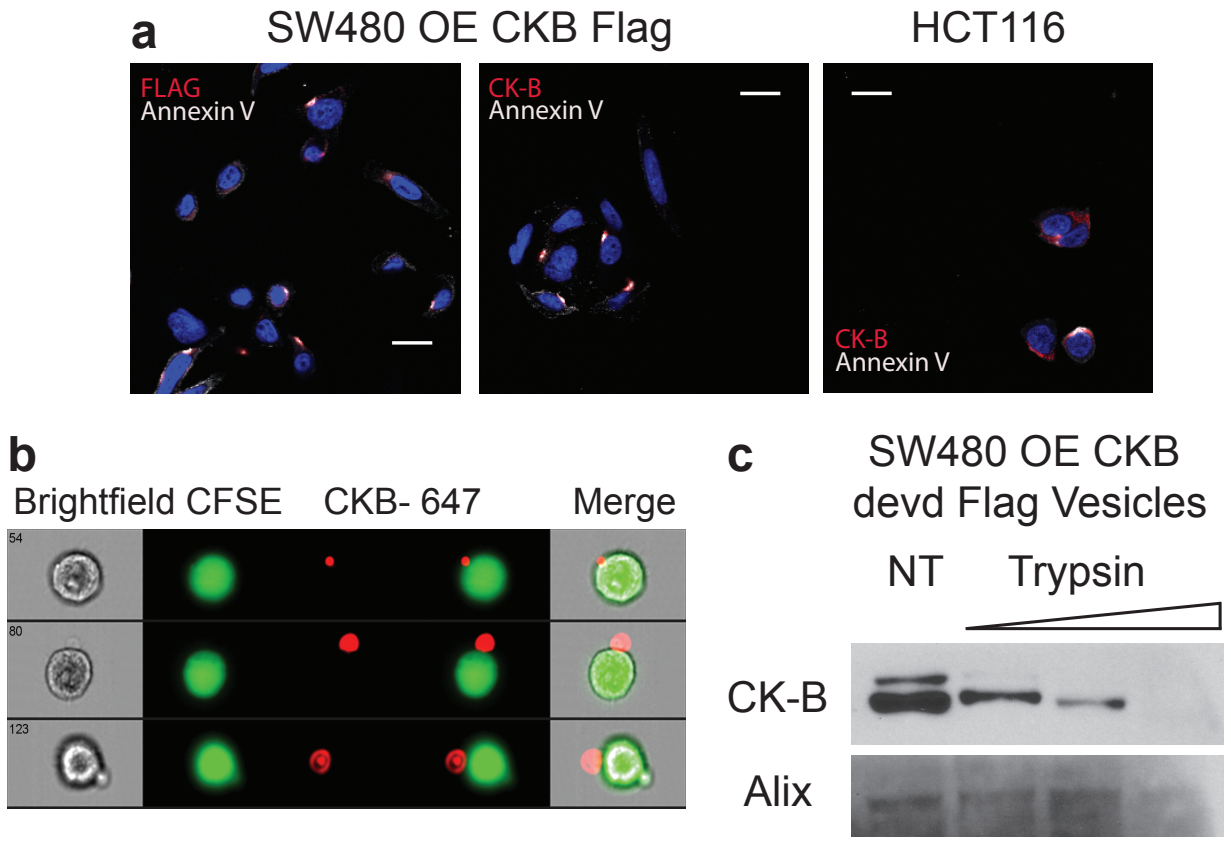

Figure 2.14 | **CKB is exposed on the extracellular surface of colorectal cancer cells.** (a) Immunofluorescent staining of the extracellular surface of HCT116 cells, CK-B in red and Annexin V-biotin conjugates, targeting phosphatidylserine, shown in white. SW480 OE CK-B devd Flag cells stained for CK-B or Flag in red. Scale bars indicate 20μm. (b) Imagestream visualization of CKB -647 on live HCT116 counterstained with CFSE. (c) Western blot of trypsin treated vesicles isolated from SW480 OE CKB devd flag cells.

to the extracellular facing surface of the plasma membrane within phosphatidylserine rich domains. These observations reveal the basis for the ability of CKB to modulate extracellular ATP/ADP levels since both the plasma membrane pool of CKB and the ectosomal pool are exposed to the extracellular space. Moreover, our ability to detect CKB in the supernatant of cells likely results from detection of CKB in released or ruptured ectosomes.

We next performed mutagenesis studies to identify a domain of CKB required for secretion. Creatine Kinase Muscle (CKM) is a homolog of CKB that localizes to the sarcoplasmic reticulum. We reasoned that CKB and CKM must have a divergent sequence that mediates their distinct cellular localizations. The N-terminus of CKM is most divergent from CKB and is required for localization of CKM to the sarcoplasmic reticulum. We thus generated an N-terminal deletion of the first 19 amino acids of CK-B and over-expressed this variant as well as full-length CKB in CKB KO HCT116 cells. In contrast to full-length CKB, N-terminal deletion mutant CKB could not be detected in the conditioned media (Fig. 2.15a), revealing the N-terminus to be critical for CKB secretion. We identified several residues that were present in the N-terminus of CKB but absent from the N-terminus of CKM. Of these, we mutated the subset of residues that could potentially be post-translationally modified. Mutations of serine at position 6 or arginine at position 13 abolished CKB secretion (Fig. 2.15b), while mutations of serine 4, lysine 11,

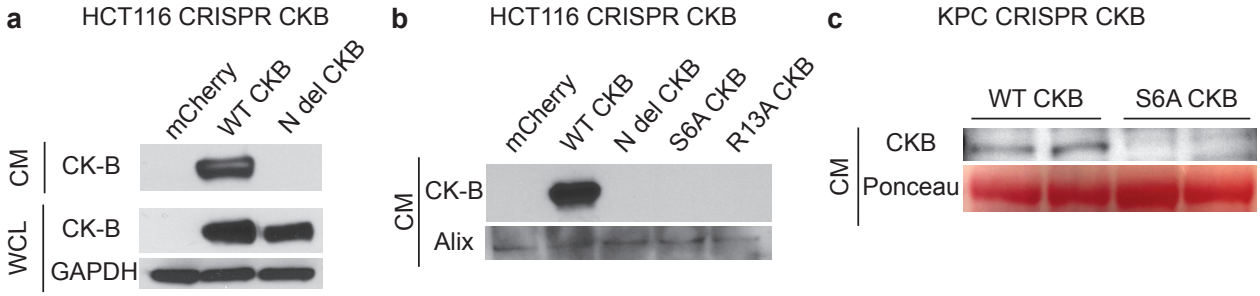

Figure 2.15 | **N terminal deletion of CKB prevents secretion.**
(a) Conditioned media collected at 6 hours with no serum from cultured HCT116 CRISPR clone with homozygous KO CKB transduced with either control, wildtype, or N terminal deletion (19AA) CKB.
(b) Conditioned media collected at 6 hours with no serum from cultured HCT116 CRISPR clone with homozygous KO CKB transduced with either control, wildtype, or N terminal deletion, or residue 6 and 13 mutations.
(c) Conditioned media collected at 6 hours with no serum from cultured KPC CRISPR clone with homozygous KO CKB transduced with either wildtype, or serine 6 mutation.

and proline 2 did not (data not shown). Mutation of serine 6 in murine CKB also abolished its secretion in the murine KPC pancreatic cancer line, revealing conserved significance of this residue (Fig. 2.15c). Our previous studies of CKB revealed that CKB promotes survival under hypoxia *in vitro*, an effect proposed to be due to its phosphorylation of creatine in the extracellular space. We thus tested N-terminal and S6A CKB mutant expressing colon cancer and pancreatic cancer cells in 0.5% oxygen for 4 days, and observed a significant reduction in survival of cells expressing secretion mutant CKB relative to WT CKB (Fig. 2.16a-c). We next tested whether the S6A mutant exhibits impaired growth at a subcutaneous tumour site, where CKB was observed to impart enhanced growth in an immune-dependent manner. Subcutaneous injections of KPC CKB KO cells over-expressing either wildtype CKB or the S6A CKB mutant revealed significantly reduced tumour growth and more efficient regression in the S6A mutant (Fig. 2.16d). These studies reveal that specific residues in the N-terminal region of CKB mediate its cellular release, which enables metabolic and tumourigenic progression phenotypes.

Our identification of CKB as an extracellular acting kinase that suppresses anti-tumour immunity in gastrointestinal cancer models via metabolic shifting of the extracellular microenvironment provides a unique therapeutic opportunity that may enhance innate and adaptive anti-tumour immune responses in gastrointestinal cancers.

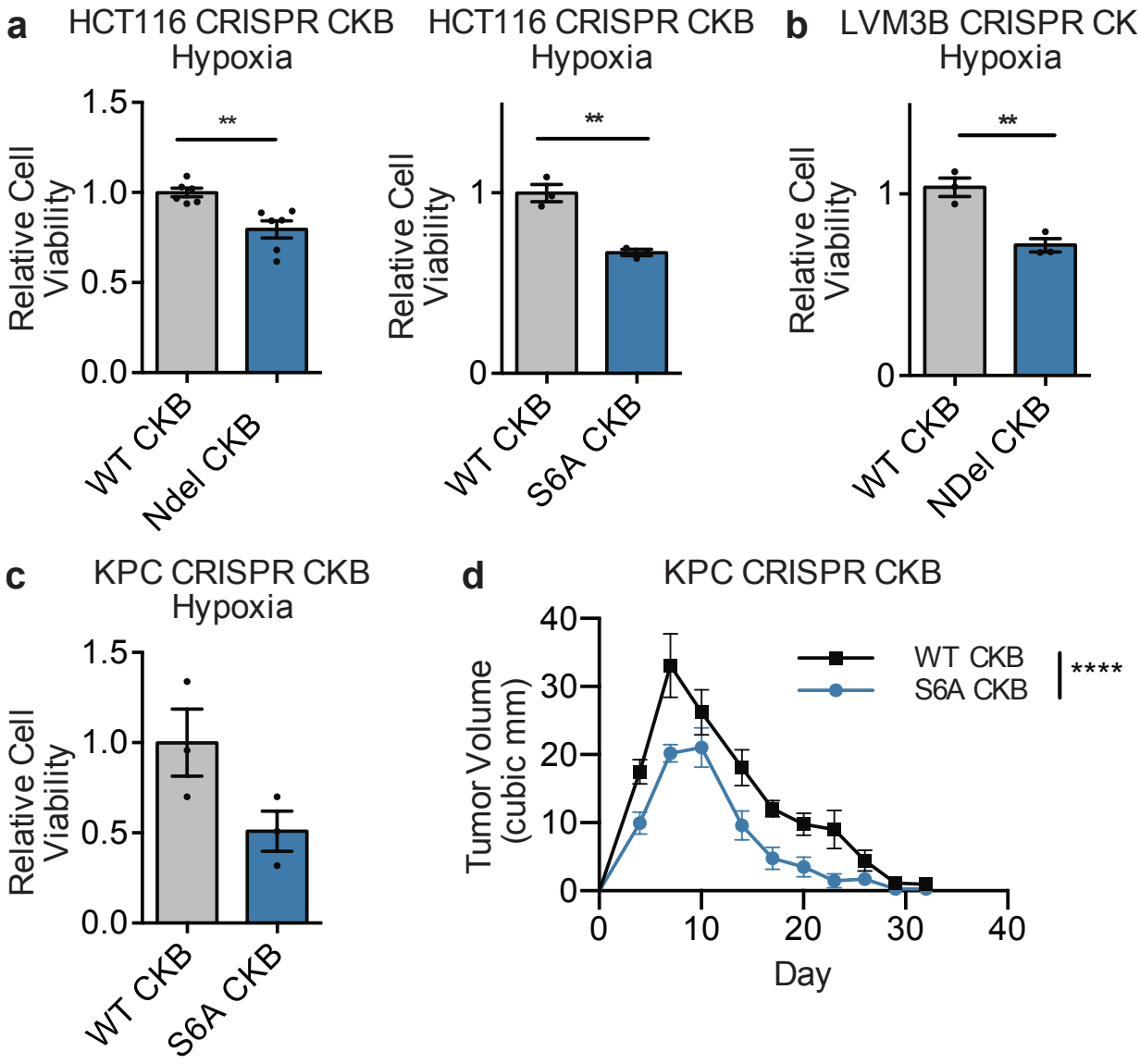

Figure 2.16 | **CKB Secretion Mutants have impaired survival *in vitro* and growth *in vivo*.**
(a) Relative cell viability of HCT116 CRISPR CKB KO cells with either WT, N-terminal deletion, or S6A mutant CKB rescue exposed to 0.5% hypoxia for 4 days. Cells measured via MTT viability assay.
(b) Same as (a) but with LS174T LVM3B CRISPR CKB KO cells with either WT or N-terminal deletion CKB rescue.
(c) Same as (a) with KPC CRISPR CKB KO cells with either wildtype or S6A mutant CKB rescue exposed to 0.5% hypoxia for 4 days.
(d) Tumor growth from subcutaneous injections of either 1 million KPC CRISPR CKB cells with either WT or S6A CKB rescue in immunocompetent mice (n=8).

Chapter III: Two isoleucyl tRNAs that decode 'synonymous' codons divergently regulate cancer progression

Divergent isoleucyl tRNA modulation in breast cancer

We sought to identify potential tRNAs that may become transcriptionally modulated during cancer progression. To do this, we performed chromatin immunoprecipitation sequencing (ChIP-seq) in poorly and highly metastatic human breast cancer cells using an antibody targeting the DNA binding subunit of Polymerase III, POLR3A (Fig. 3.1a). Enrichment of tRNA loci was confirmed by successful pull-down of Pol III genomic target loci through quantitative real-time PCR (qPCR) (Fig. 3.1b), as well as significant enrichment of ChIP-seq reads for tRNA Box A and Box B gene regulatory sequences (Fig. 3.1c). We observed that an isoleucyl UAU tRNA isoacceptor locus was significantly more bound by Pol III in highly metastatic MDA-MB-231 LM2 cells relative to the isogenic parental poorly-metastatic MDA-MB-231 cells from which it was derived. To confirm these findings and to establish that mature $tRNA^{Ile}_{UAU}$ levels are upregulated in metastatic cells, we performed targeted tRNA profiling by tRNA Capture-seq[72] of all human tRNA isoleucyl isoacceptors. Targeted tRNA quantification in the MDA-MB-231 poorly/highly

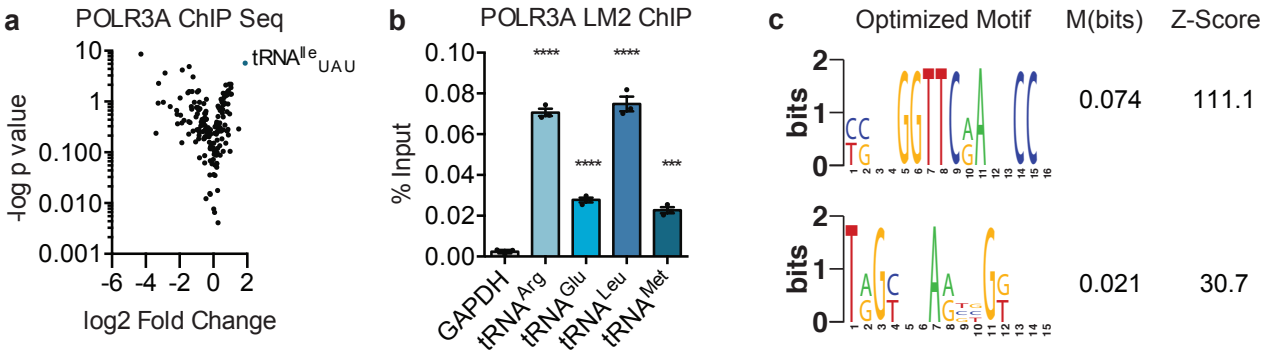

Figure 3.1 | **POLR3A ChIP Sequencing reveals differential occupancy in isogenic poorly and highly metastatic breast cancer pairs.**
(a) Volcano plot representing log2 fold change vs. –log p value of POL3RA ChIP sequencing analysis of MDA LM2 cells vs. MDA MB 231 Parental cells.
(b) tRNA genomic loci abundance measured as % Input using RT-qPCR of POLR3A IP cDNA with GAPDH as a negative control. Two-sided un-paired student's t-tests performed, p-values represented ***, **** as $p<0.001$ and $p<0.0001$ respectively.
(c) Motif analysis of POLR3A IP normalized to input sequences using FIRE analysis.

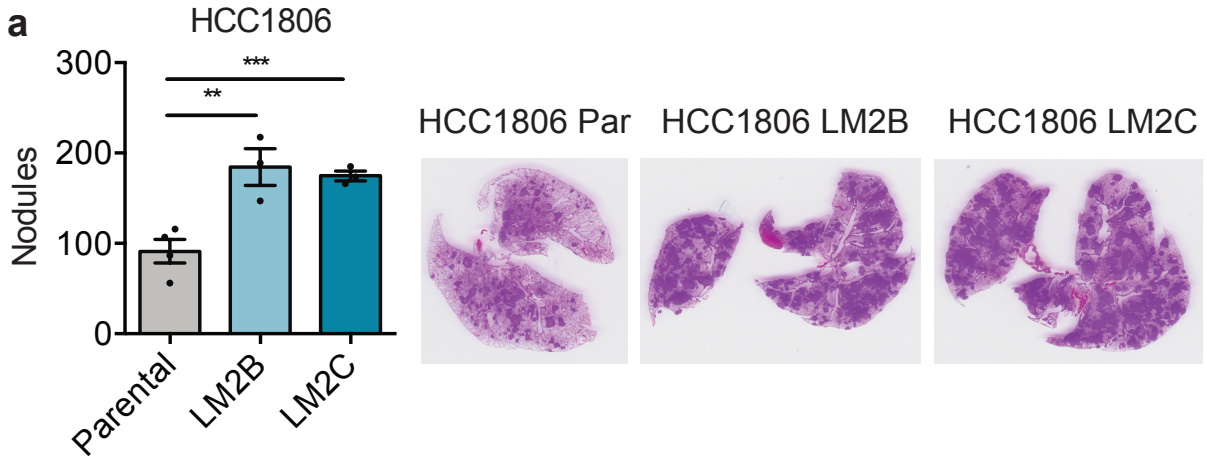

Figure 3.2 | **In vivo selection of HCC1806 breast cancer increases metastatic capacity.** (a) Quantification of lung metastatic nodules post extraction after tail vein injection of $1.5x10^5$ HCC1806 Parental or highly metastatic derivatives LM2B or LM2C, with representative histology; n=3-4 in each cohort. Two-sided un-paired student's t-tests performed, p-values **, *** represented as $p<0.01$, and $p<0.001$, respectively.

metastatic pair as well as an independent poorly/highly metastatic isogenic human breast cancer line pair (HCC1806-Par and HCC1806-LM2C, Figure 3.2) confirmed that mature $tRNA^{Ile}_{UAU}$ is upregulated in highly metastatic breast cancer cells relative to isogenic poorly metastatic cells (Fig. 3.3a). Northern blot analysis confirmed the observations of $tRNA^{Ile}_{UAU}$ over-expression in highly metastatic breast cancer cells (Fig. 3.3b). We made the surprising observation that one of the other isoacceptors of isoleucine, $tRNA^{Ile}_{GAU}$, became significantly repressed in patients' highly metastatic sublines relative to their isogenic poorly metastatic parental cells (Fig 3.4a). The high sequence similarity between $tRNA^{Ile}_{GAU}$ and another isoleucine isoacceptor $tRNA^{Ile}_{AAU}$ precluded specific northern blot quantification for $tRNA^{Ile}_{GAU}$ as an independent tRNA quantification method. We thus employed pre-tRNA quantification as an orthogonal approach for assessing the levels of all three isoleucyl tRNA genes. Pre-tRNA qRT-PCR also revealed upregulation of multiple $tRNA^{Ile}_{UAU}$ loci genes and conversely, repression of $tRNA^{Ile}_{GAU}$ loci genes in highly metastatic breast cancer cells relative to poorly metastatic cells

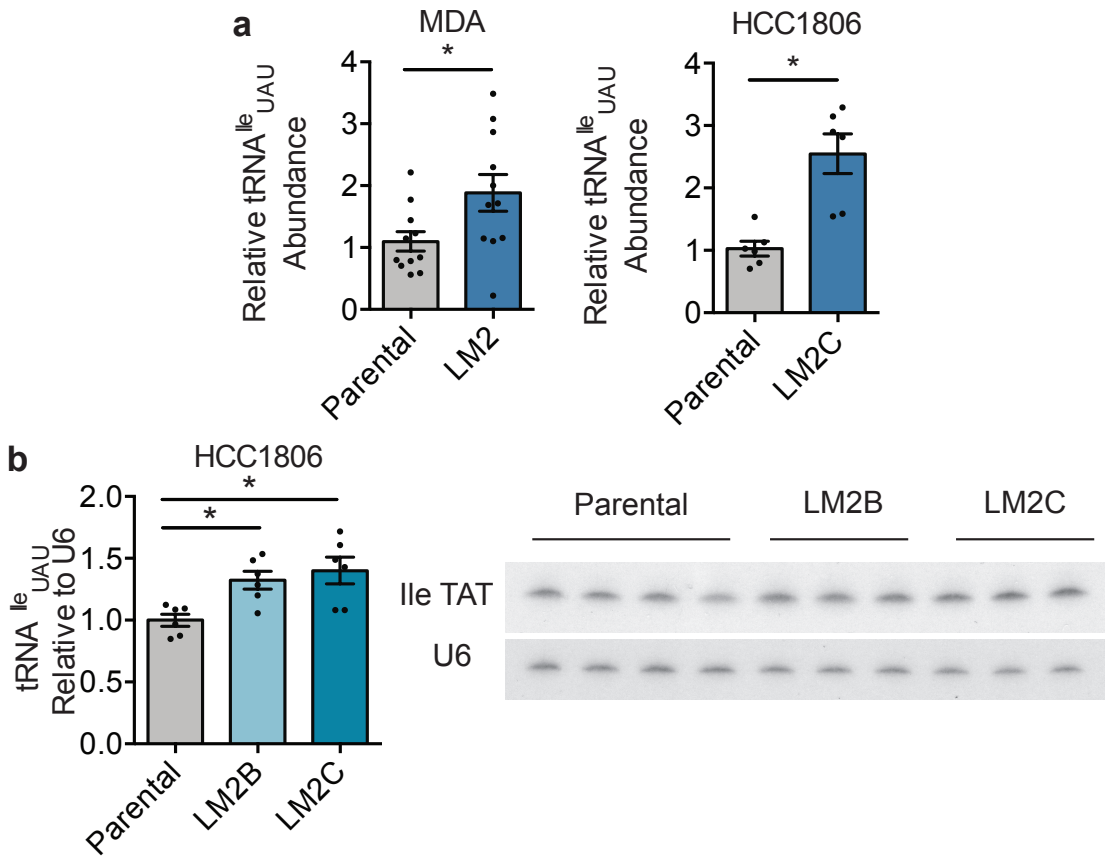

Figure 3.3 | **Mature tRNA$^{Ile}_{UAU}$ is differentially modulated in isogenic poorly and highly metastatic breast cancer pairs.**
(a) tRNA$^{Ile}_{UAU}$ quantification by specific tRNA$^{Ile}_{UAU}$ probe RT-qPCR normalized to 18S probes of highly metastatic LM2 lines relative to their parental MDA-MB-231 and HCC1806 cell lines.
(b) Northern blot quantification of tRNA$^{Ile}_{UAU}$ relative to U6 of two independently derived LM2 lines relative to HCC1806 Parental cells with representative blot to the right. Two-sided un-paired student's t-tests performed, p-values represented * as $p<0.05$.

(Fig 3.4b-c). We did not observe such global modulations of the third isoleucyl isoacceptor pre-tRNA$^{Ile}_{AAU}$ across the loci surveyed (7/14 loci, Fig. 3.4d). Furthermore, FISH staining with a locked nucleic acid targeting tRNA$^{Ile}_{UAU}$ on tissue microarrays of breast cancer patients revealed significantly increased tRNA$^{Ile}_{UAU}$ expression in breast tumours of patients with stage III & IV disease relative to stage I/II tumours or adjacent

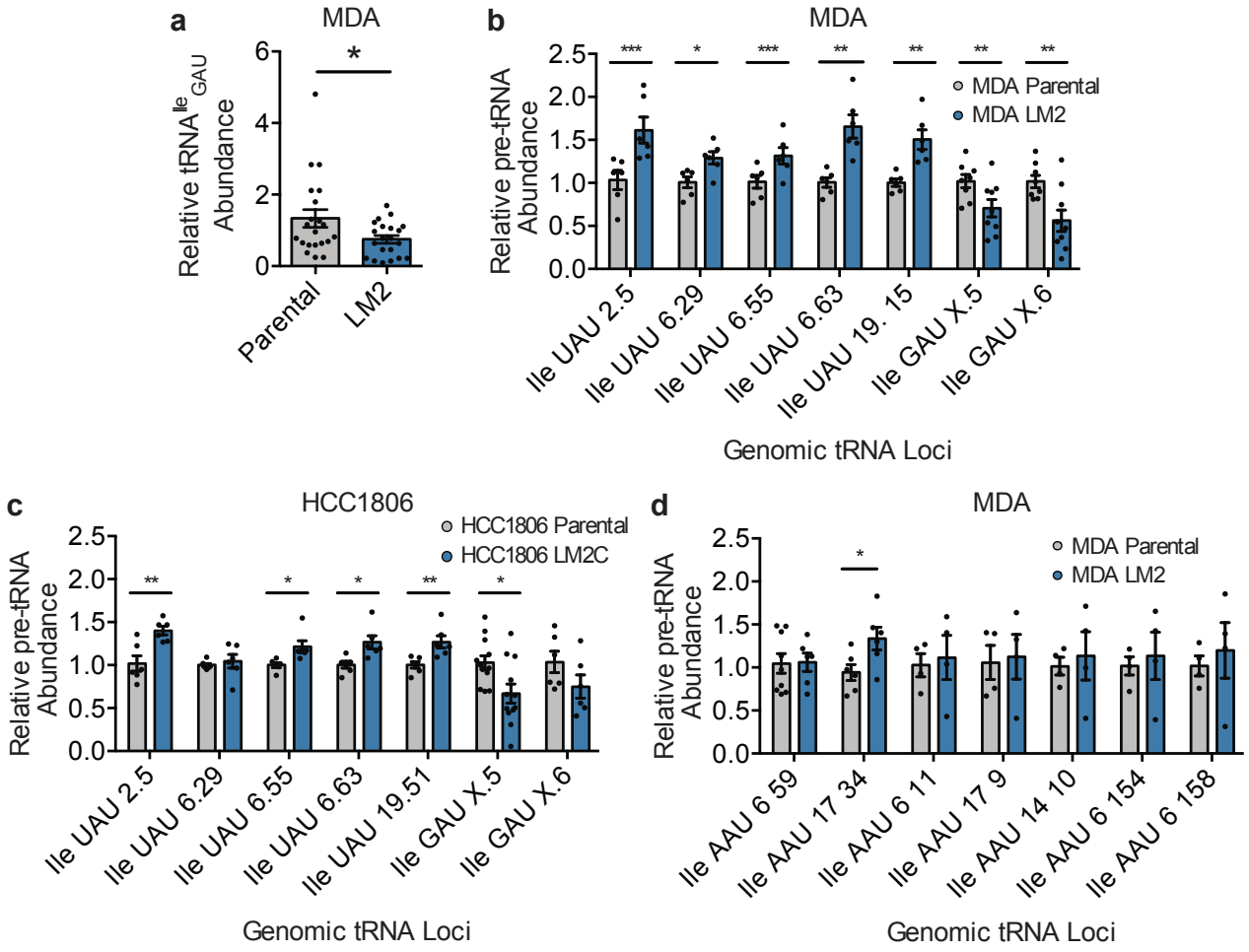

Figure 3.4 | **Differential abundance of pre-tRNA^{Ile} species in poorly & highly metastatic breast cancer MDA cells.**
(a) tRNA$^{Ile}_{GAU}$ quantification by specific tRNA$^{Ile}_{GAU}$ probe RT-qPCR normalized to 18S probes of highly metastatic LM2 lines relative to the parental MDA-MB-231 cell line.
(b,c) Relative pre-tRNA abundance of tRNA$^{Ile}_{UAU}$ and tRNA$^{Ile}_{GAU}$ across multiple primers covering distinct genetic loci using RT-qPCR of MDA LM2 vs. MDA-MB-231 (b) & HCC1806 LM2C vs. HCC1806 Parental cells (c), normalized to 18S levels.
(d) Relative pre-tRNA abundance of tRNA$^{Ile}_{AAU}$ across multiple primers covering distinct genetic loci using RT-qPCR of MDA LM2 vs. MDA-MB-231. Two-sided un-paired student's t-tests performed, p-values represented *, **, *** as $p<0.05$, $p<0.01$, and $p<0.001$, respectively.

normal tissues (Fig. 3.5a). Conversely, FISH analysis revealed significant repression of $tRNA^{Ile}_{GAU}$ expression in higher stage breast tumours relative to stage I breast tumours or adjacent normal tissues (Fig 3.5b). These findings reveal that breast cancer metastatic progression selects for upregulation of one isoleucyl tRNA isoacceptor and repression of another. This shift in tRNA isoleucyl isoacceptor levels upon this cellular state transition suggests differential roles for these tRNAs in breast cancer progression.

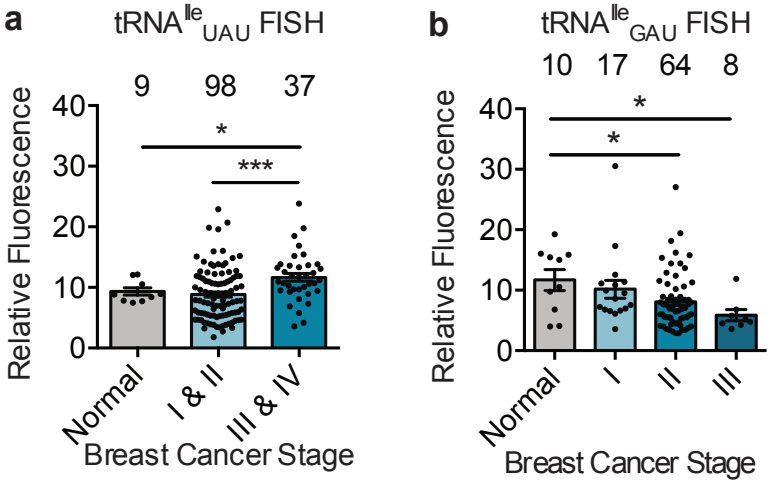

Figure 3.5 | **Clinical relevance of $tRNA^{Ile}$ isoacceptors.** (a,b) Relative fluorescent intensity normalized to DAPI of breast tissue microarrays, stratified by normal tissue or breast cancer stage I & II, III & IV, measured by FISH with LNA targeting $tRNA^{Ile}_{UAU}$ (a) or $tRNA^{Ile}_{GAU}$ (b). Two sided un-paired student's t-tests performed, p-values represented as *, *** as $p<0.05$, $p<0.001$, respectively.

$TRNA^{Ile}_{UAU}$ promotes breast cancer metastasis

To determine if the observed reciprocal tRNA isoleucyl isoacceptor modulations play causal roles in cancer progression, we performed loss-of-function and gain-of-function studies for these tRNA isoacceptors and assessed the organismal consequences on cancer progression. We first sought to overexpress $tRNA^{Ile}_{UAU}$ in poorly metastatic cells to assess whether its upregulation is sufficient to confer increased metastatic capacity (Fig 3.6a-b).

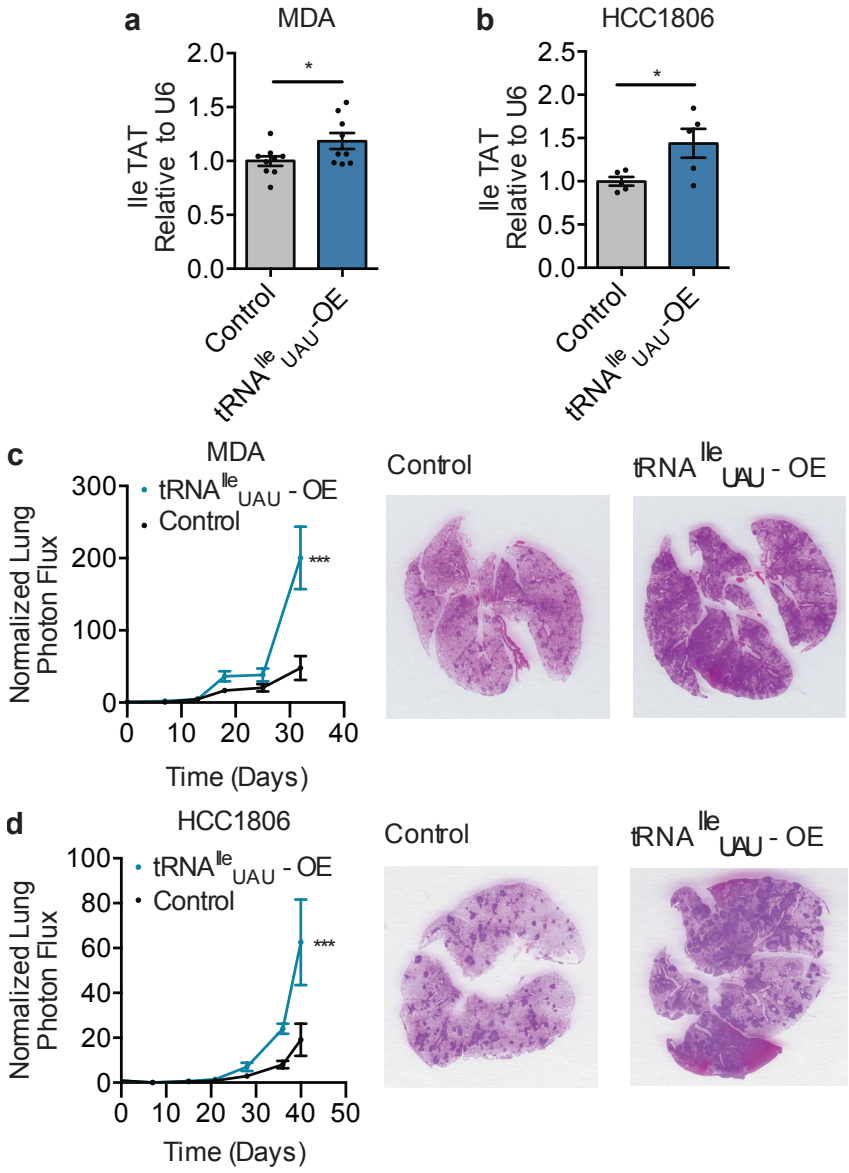

Figure 3.6 | **tRNA$^{Ile}_{UAU}$ promotes metastatic colonization.**
(a,b) Northern blot quantification of tRNA$^{Ile}_{UAU}$ relative to U6 of MDA (a) or HCC1806 (b) Parental cells with control or overexpression of tRNA$^{Ile}_{UAU}$.
(c) Bioluminescent imaging post tail vein injection of 1x10^5 of MDA Parental cells overexpressing tRNA$^{Ile}_{UAU}$ or control with representative lung histology stained with H&E; n=5 in each cohort.
(d) Same as (c) with 1.5x10^5 HCC1806 cells. Two-way unpaired student's's t-test and 2-way ANOVAs performed, p-value of *, *** indicated as $p<0.05$, $p<0.001$, respectively.

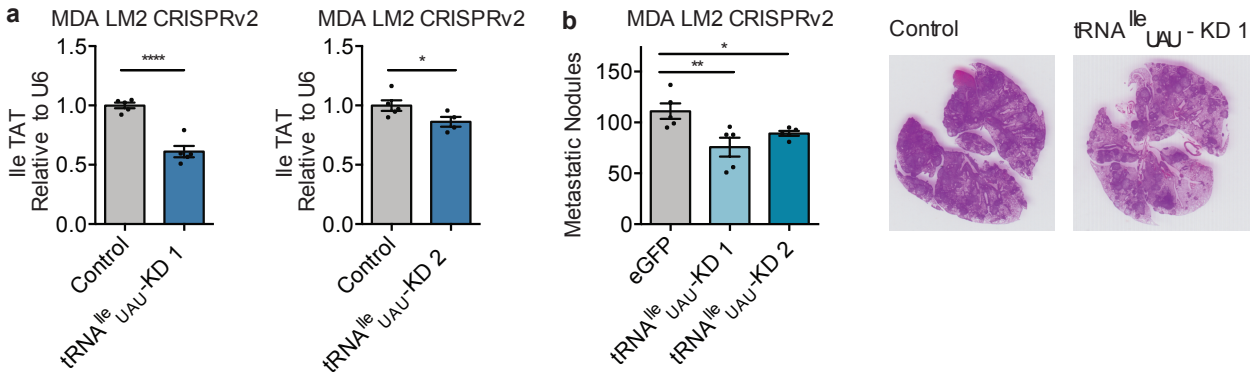

Figure 3.7 | Knockdown of $tRNA^{Ile}_{UAU}$ is sufficient to reduce lung metastatic colonization.
(a) Northern blot quantification of $tRNA^{Ile}_{UAU}$ relative to U6 of LM2 cells depleted of $tRNA^{Ile}_{UAU}$ via CRISPR with Guide 1 or 2 versus control.
(b) Quantification of lung metastatic nodules post extraction after tail vein injection of $5x10^4$ LM2 CRISPR cells with guides targeting eGFP or $tRNA^{Ile}_{UAU}$, with representative histology for control & $tRNA^{Ile}_{UAU}$ guide 1; n=5 in each cohort. Two sided un-paired student's t-tests performed, p-values represented as *, **, **** as $p<0.05$, $p<0.01$, $p< 0.0001$ respectively.

Stable over-expression of $tRNA^{Ile}_{UAU}$ to pathophysiologically relevant levels (~50% increase) in poorly metastatic MDA-MB-231 or HCC1806 human cell lines significantly increased lung metastatic colonization in tail-vein colonization assays as assessed by bioluminescence imaging and histological analyses (Fig. 3.6c-d). For loss-of-function studies, we employed CRISPR-Cas9 using two independent guides specific to $tRNA^{Ile}_{UAU}$ genomic loci (Fig. 3.7a). CRISPR-Cas9 mediated depletion of $tRNA^{Ile}_{UAU}$ in highly metastatic MDA-LM2 breast cancer cells to levels similar to poorly metastatic cells (~40% reduction by guide1 and 20% by guide 2) was sufficient to significantly impair breast cancer metastatic colonization (Fig. 3.7b). These findings reveal $tRNA^{Ile}_{UAU}$ to be a promoter of metastatic progression by these human breast cancer cells.

TRNA$^{Ile}_{GAU}$ suppresses breast cancer metastatic colonization

We next determined if tRNA$^{Ile}_{GAU}$, which became repressed in metastatic cells, plays a causal role in breast cancer progression. TRNA$^{Ile}_{GAU}$ was stably overexpressed in highly metastatic MDA-LM2 cells to levels similar to that observed in poorly metastatic MDA-231 parental cells (~1.8-fold over-expression) (Fig. 3.8a). Increasing tRNA$^{Ile}_{GAU}$ expression in highly metastatic MDA-LM2 cells substantially reduced the metastatic lung colonization capacity of MDA-LM2 cells (Fig. 3.8b). Given the high sequence similarity between tRNA$^{Ile}_{GAU}$ and tRNA$^{Ile}_{AAU}$, we employed two orthogonal approaches for tRNA$^{Ile}_{GAU}$ loss-of-function—CRISPRi and shRNA mediated interference. Firstly, MDA-231 cells were stably transduced with mutant Cas9-KRAB and a specific guide complementary to common sequences in tRNA$^{Ile}_{GAU}$ genomic loci. Reduced tRNA$^{Ile}_{GAU}$ was confirmed by targeted tRNA capture qPCR (Fig. 3.9a).

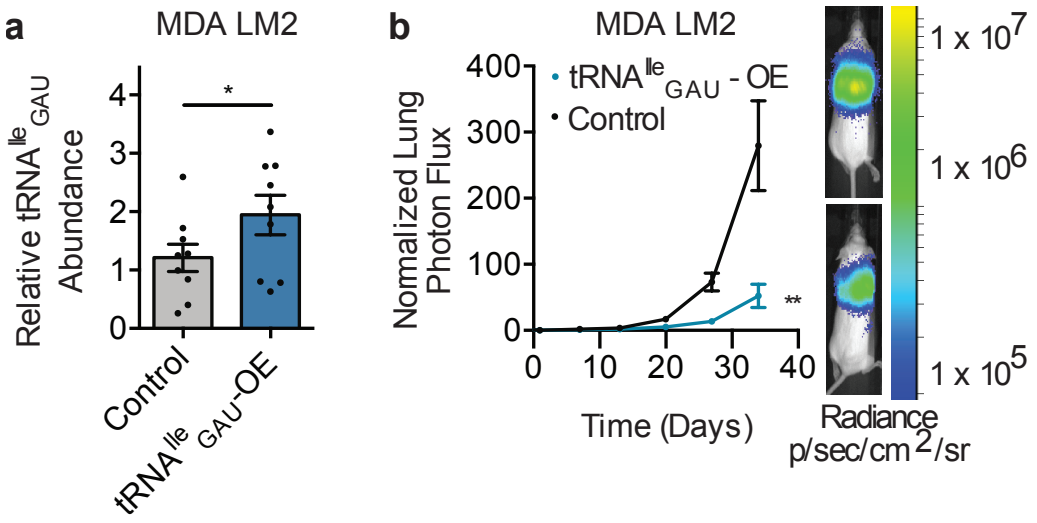

Figure 3.8 | **tRNA$^{Ile}_{GAU}$ suppresses metastatic colonization.**
(a) tRNA$^{Ile}_{GAU}$ quantification by specific tRNA$^{Ile}_{GAU}$ probe RT-qPCR normalized to 18S probes of LM2 cells with control or overexpression of tRNA$^{Ile}_{GAU}$.
(b) Bioluminescence imaging after tail vein injection of $1x10^5$ of MDA LM2 cells overexpressing tRNA$^{Ile}_{GAU}$ or control with representative images; luminescence expressed as Radiance p/sec/cm^2/sr; n=5 in each cohort. Two-way unpaired student's's t-test and 2-way ANOVA performed, p-value of *, ** indicated as $p<0.05$, $p<0.01$, respectively.

ShRNA-mediated interference was also employed using a hairpin specific to $tRNA^{Ile}_{GAU}$ (Fig. 3.9b). Depletion of $tRNA^{Ile}_{GAU}$ using both of these approaches enhanced lung metastatic colonization by poorly metastatic MDA-231 cells (Fig. 3.9c-d). These findings implicate $tRNA^{Ile}_{GAU}$ as a metastasis suppressor tRNA. These functional studies uncover two surprising findings: the first being demonstration of a gain-of-function organismal

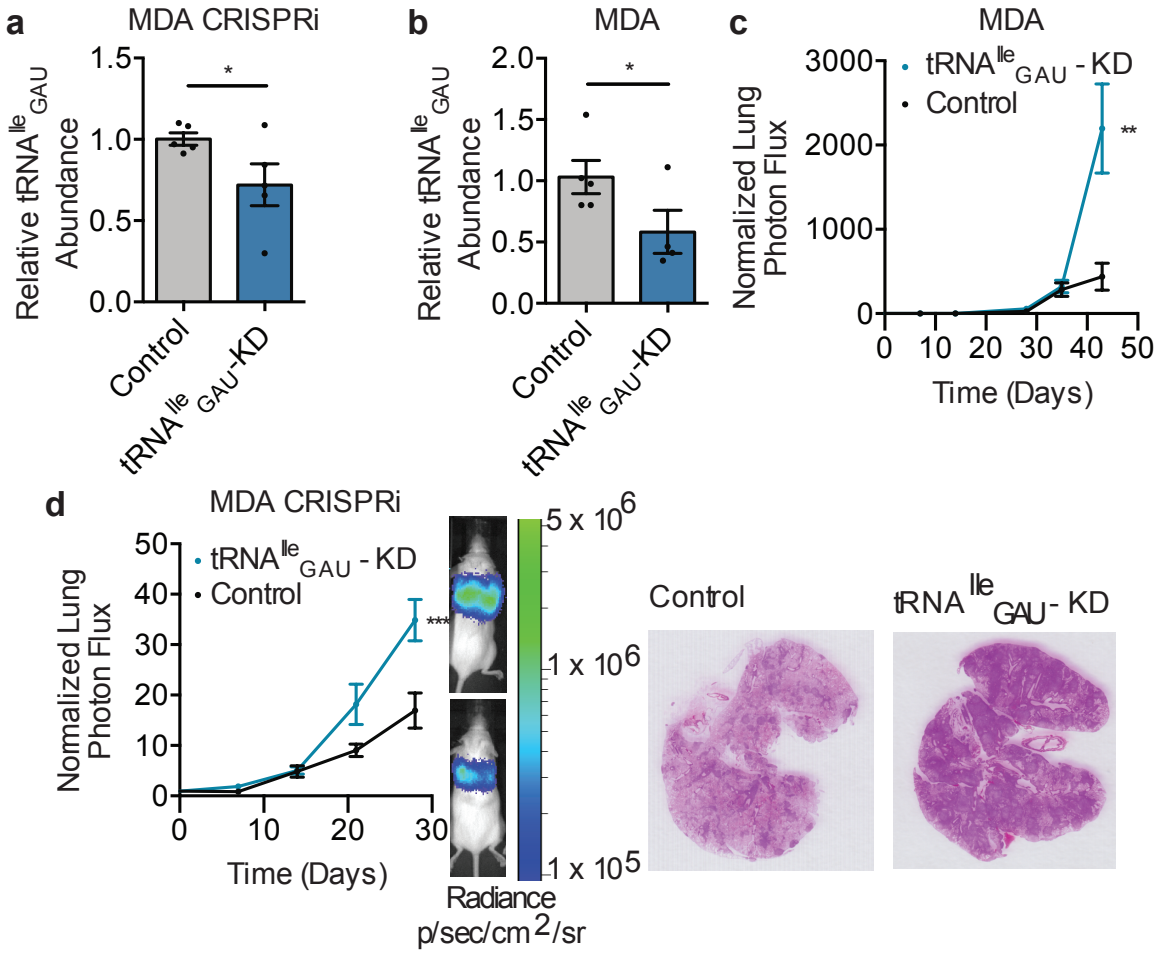

Figure 3.9 | Knockdown of $tRNA^{Ile}_{GAU}$ drives lung metastatic colonization.
(a,b) $tRNA^{Ile}_{GAU}$ quantification by specific $tRNA^{Ile}_{GAU}$ probe RT-qPCR normalized to 18S probes of MDA Parental CRISPRi cells with guides targeting either control (eGFP) or $tRNA^{Ile}_{GAU}$ (a) or shRNA targeting control or $tRNA^{Ile}_{GAU}$ (b).
(c,d) Bioluminesnce imaging of MDA Parental CRISPRi cells with guides targeting either control or $tRNA^{Ile}_{GAU}$ (c) or shRNA targeting control or $tRNA^{Ile}_{GAU}$ tail vein injected with representing H&E lung histology (d). Statistics utilized include 2-way ANOVA for imaging and unpaired student's t-test for nodule quantification, p-values represented as *, **, *** as $p<0.05$, $p<0.01$, $p<0.001$.

phenotype upon depletion of a tRNA ($tRNA^{Ile}_{GAU}$); the second being the observation of a dichotomy between two tRNA isoacceptors in regulation of a phenotype.

Divergent regulation of growth by isoacceptor tRNAs

We next sought to identify the cancer progression cellular phenotype regulated by $tRNA^{Ile}_{UAU}$ and $tRNA^{Ile}_{GAU}$. As a first step, we conducted ribosomal profiling of breast cancer cells in the context of $tRNA^{Ile}_{UAU}$ overexpression and $tRNA^{Ile}_{GAU}$ depletion (by

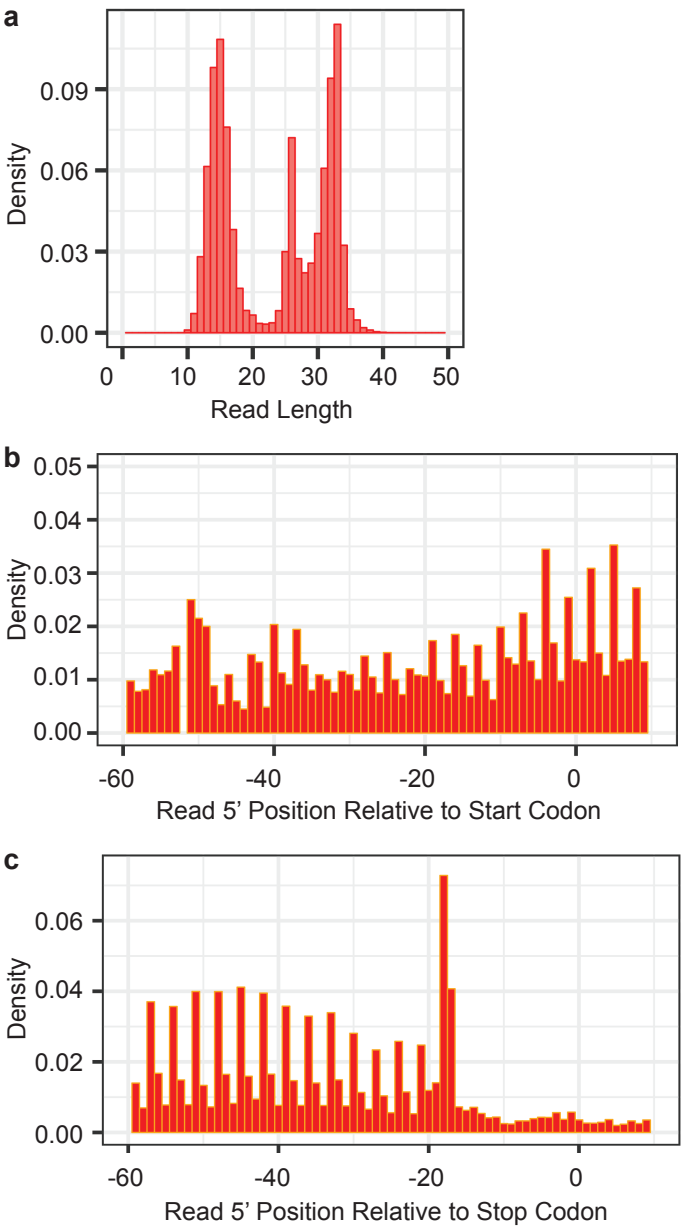

Figure 3.10 | **Length and periodicity of ribosomal protected fragments isolated from MDA-231 breast cancer cells.** (a) Histogram depicting distribution of read length of ribosomal protected fragments. (b,c). Histogram of read coverage to demonstrate 3 nucleotide periodicity of the coding sequence with respect to the start (b) and stop codon (c) of the reading frame

CRISPRi), mirroring the divergent $tRNA^{Ile}$ modulations observed in highly metastatic cells relative to poorly metastatic cells. Ribosomal protected fragments were sequenced, and conformed to the expected size and periodicity reported by other groups[93] (Fig. 3.10a-c). Ribosomal occupancy of transcripts was then quantified as a measure of translational efficiency. Genes enriched in GO terms such as cell cycle and mitosis exhibited enhanced translational efficiency (Fig. 3.11a). GO function analysis of proteins in $tRNA^{Ile}_{UAU}$/$tRNA^{Ile}_{GAU}$ modulated cells by label free mass spectrometric quantification revealed enrichment of similar gene sets including cell cycle, mitosis, as well as regulation of stress response relative to control cells (Fig. 3.11b). Consistent with these molecular observations, immunofluorescent staining of metastatic nodules for the proliferation marker Ki67 revealed that breast cancer cells concomitantly over-expressing $tRNA^{Ile}_{UAU}$ and depleted of $tRNA^{Ile}_{GAU}$ exhibited greater proliferation than control cells (Fig. 3.11c-d). Conversely, metastatic nodules formed by highly metastatic MDA-LM2 cells depleted of $tRNA^{Ile}_{UAU}$ (via CRISPR) exhibited reduced proliferation relative to control nodules (Fig. 3.11e). To determine if these *in vivo* observations could be recapitulated *in vitro*, growth assays were performed under normal tissue culture conditions or under

conditions of hypoxic and oxidative stress, since such stresses occur in the metastatic microenvironment and can restrict proliferation[39,50-52,71,94]. Concomitant $tRNA^{Ile}_{UAU}$ upregulation/$tRNA^{Ile}_{GAU}$ depletion enhanced the *in vitro* growth of MDA-MB-231 breast cancer cells relative to control cells in the context of hypoxia (Fig. 3.12a) and oxidative stress (Fig. 3.12b). Importantly, growth effects were more pronounced under these stress conditions than under normoxic basal *in vitro* conditions (Supplementary Fig. 3f). This findings reveal that divergent modulation of these isoleucyl tRNA isoacceptors promotes growth in these breast cancer cells *in vitro* and *in vivo*.

a

GO Term	p-value
RNA Processing	8.97 e-08
Posttranscriptional Regulation	2.58 e-07
Cell Cycle	2.77 e-07
Regulation of Transferase Act.	2.51 e-06
Regulation of Organelle Organiz.	3.32 e-06
ncRNA Processing	1.15 e-05
DNA Metabolic Process	1.85 e-05
Mitotic Cell Cycle	2.01 e-05
Cell Cycle Phase Transition	1.51 e-04

b

GO Term	p-value
Cell Cycle	5.44 e-11
Mitotic Cell Cycle	2.34 e-10
Chromosome Organization	6.71 e-08
RNA Processing	5.99 e-07
Regulation of Response to Stress	7.67 e-07
Regulation of Cell. Response to Stress	8.71 e-07
Membrane Disassembly	2.10 e-06
RNP Complex Biogenesis	2.18 e-06
Posttranscriptional Regulation	2.49 e-06

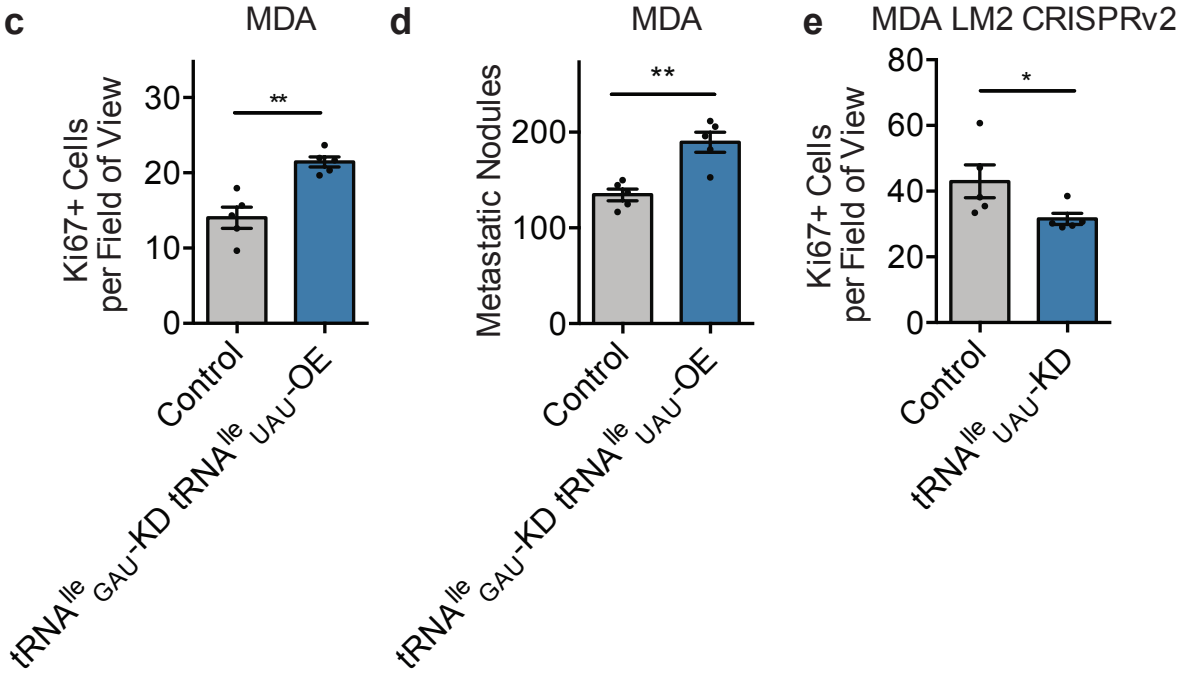

Figure 3.11 | **Cell Cycle and Response to Stress gene expression and phenotypes characterize tRNA^{Ile} modulations.**
(a,b) GO function terms for positive and significant TE changes from ribosomal profiling (a) or label free quantification by mass spectrometry (b) in tRNA$^{Ile}_{GAU}$ depletion and tRNA$^{Ile}_{UAU}$ overexpression cells versus control.
(c) Quantification of Ki67 immunofluorescence staining in tRNA$^{Ile}_{GAU}$ depletion and tRNA$^{Ile}_{UAU}$ overexpression cells versus control.
(d) Quantification of lung metastatic nodules post extraction after tail vein injection of $1x10^5$ MDA tRNA$^{Ile}_{GAU}$ depleted and tRNA$^{Ile}_{UAU}$ overexpression cells versus control.
(e) Quantification of Ki67 immunofluorescence staining in LM2 CRISPR cells with guides targeting either control or tRNA$^{Ile}_{UAU}$ loci. Two-sided un-paired student's t-tests performed, p-values represented as *, ** as $p<0.05$, $p<0.01$, respectively.

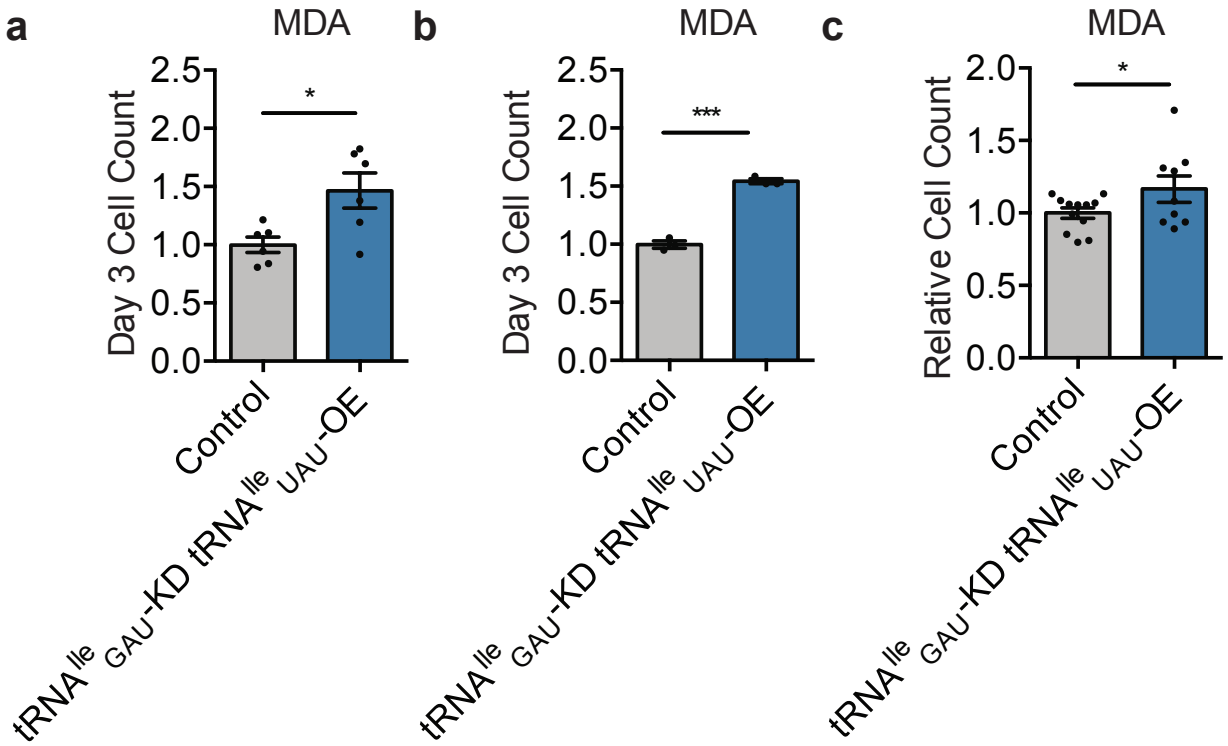

Figure 3.12 | **tRNA$^{Ile}_{UAU}$ overexpression and tRNA$^{Ile}_{GAU}$ knockdown promotes growth under hypoxia & oxidative stress.**
(a,b) Relative cell counts of MDA MB 231 control & tRNA$^{Ile}_{GAU}$ depletion tRNA$^{Ile}_{UAU}$ overexpression cells exposed to 0.5% hypoxia (a) or treated with 200uM H202 (b) for 3 days.
(c) Relative cell counts of MDA MB 231 control & tRNA$^{Ile}_{GAU}$ depletion tRNA$^{Ile}_{UAU}$ overexpression cells after 5 days. Two sided un-paired student's's t-tests performed, p-values represented as *, *** as $p<0.05$, $p<0.001$, respectively.

Distinct isoleucyl tRNA growth regulatory networks

We next sought to define downstream effector genes that mediate metastatic cell growth downstream of tRNA$^{Ile}_{UAU}$/tRNA$^{Ile}_{GAU}$ modulation. We first hypothesized that tRNA$^{Ile}_{UAU}$ enhances translation of a set of growth promoting genes. To this end, we identified the set of genes that exhibited enhanced translational efficiency as well as enhanced mass-spectrometric protein abundances upon concurrent tRNA$^{Ile}_{UAU}$/tRNA$^{Ile}_{GAU}$ modulation, and exhibited a high relative synonymous codon usage score for tRNA$^{Ile}_{UAU}$, which becomes upregulated. The ten genes that fulfilled these criteria were further restricted to

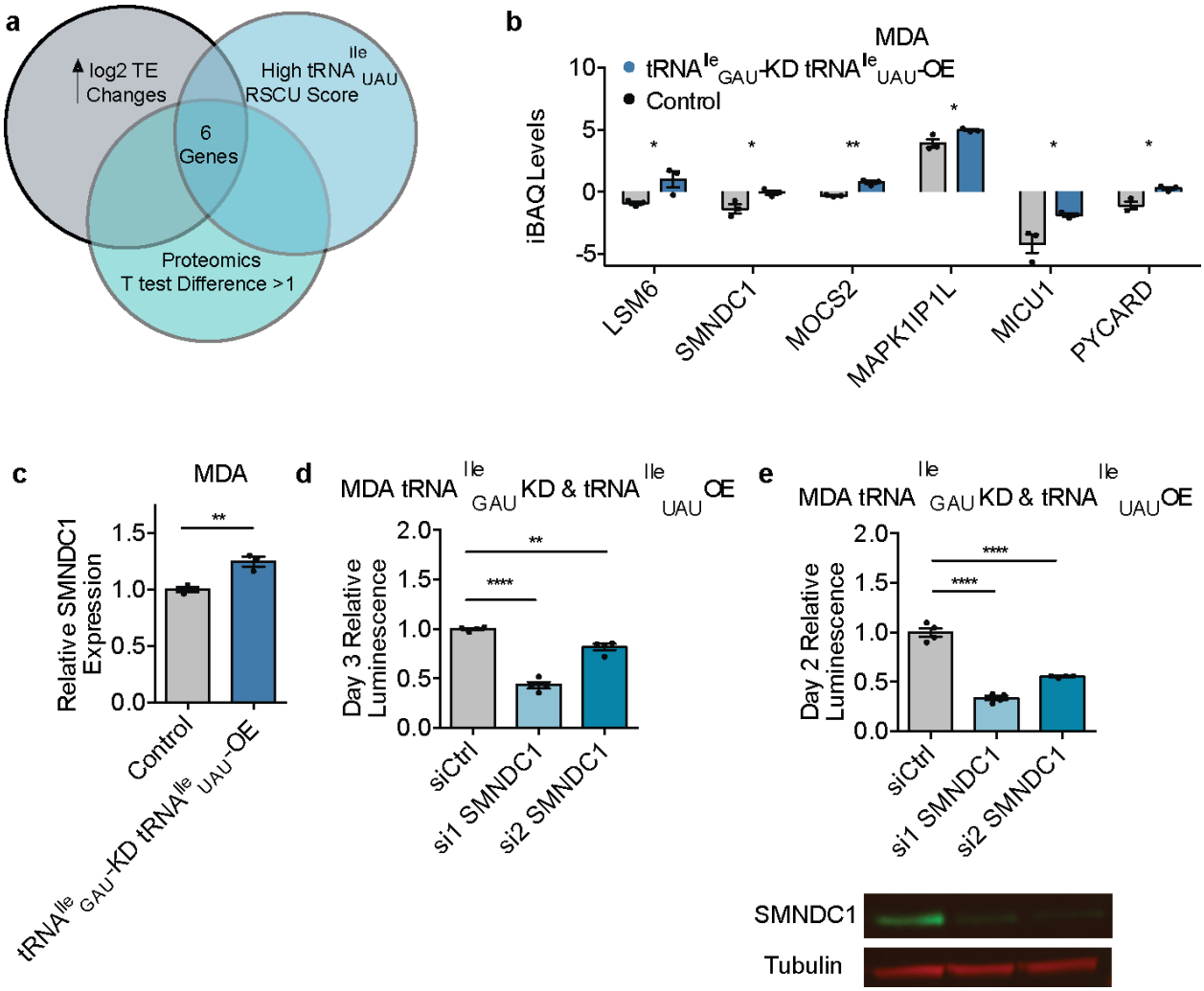

Figure 3.13 | **Downstream effector with high tRNA$^{Ile}_{UAU}$ RSCU SMNDC1 promotes growth.**
(a) Venn Diagram of overlapping datasets to identify downstream effectors – includes high RSCU tRNA$^{Ile}_{UAU}$ score, and genes with significantly positive changes in TE and proteomics in both MDA LM2 vs. MDA Parental cells and tRNA$^{Ile}_{GAU}$ depletion tRNA$^{Ile}_{UAU}$ overexpression cells vs. control.
(b) iBAQ values of six candidate downstream effectors, measured by label free quantification mass spectrometry; 3 biological replicates each.
(c) Relative SMNDC1 protein expression measured by LICOR western in control vs. tRNA$^{Ile}_{GAU}$ depletion tRNA$^{Ile}_{UAU}$ overexpression cells, normalized to α-tubulin.
(d,e) Relative cell count of MDA tRNA$^{Ile}_{GAU}$ depletion tRNA$^{Ile}_{UAU}$ overexpression cells treated with control or SMNDC1 siRNA for 3 days (d) or in 0.5% hypoxia for 2 days (e). Western performed on siRNA cells on day 3. Two-sided un-paired student's's t-tests performed, p-values *, **, **** indicated as $p<0.05$, $p<0.01$, and $p<0.0001$, respectively.

those that exhibited enhanced translational efficiencies and protein abundances in highly metastatic MDA-LM2 cells, which endogenously modulate these tRNAs relative to the isogenic parental MDA-231 population (Fig. 3.13a). This process yielded six genes as candidate downstream growth-promoting effectors (Fig. 3.13b). Quantitative LICOR

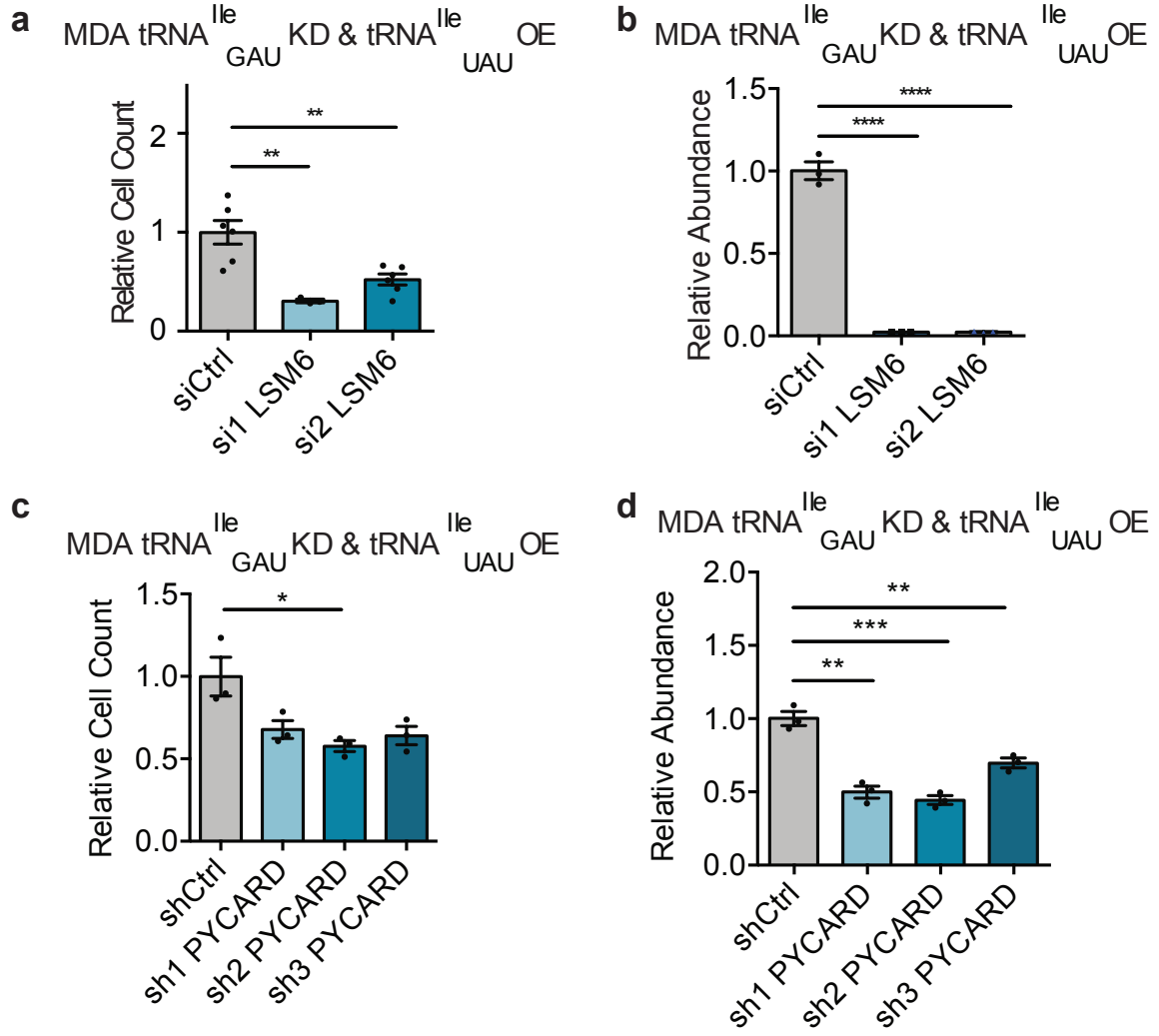

Figure 3.14 | **Knockdown of downstream effectors LSM6 & PYCARD reduces growth.**
(a) Relative cell counts of MDA $tRNA^{Ile}_{GAU}$ depletion $tRNA^{Ile}_{UAU}$ overexpression cells treated with control or LSM6 siRNA for 3 days.
(b) RT-qPCR quantification of LSM6 cDNA levels normalized to GAPDH on Day 2 of siRNA transfection.
(c) Relative cell counts of MDA $tRNA^{Ile}_{GAU}$ depletion $tRNA^{Ile}_{UAU}$ overexpression cells transduced with shRNA targeting either control or PYCARD for 3 days.
(d) RT-qPCR quantification of PYCARD cDNA levels normalized to GAPDH. Two-sided un-paired student's's t-tests performed, p-values represented as *, **, ***, **** as $p<0.05$, $p<0.01$, $p<0.001$, p,0.0001, respectively.

western blotting of one such gene, survival motor neuron domain containing (SMNDC1), confirmed that concurrent $tRNA^{Ile}_{UAU}$/$tRNA^{Ile}_{GAU}$ modulation increased its protein levels in breast cancer cells (Fig. 3.13c). Moreover, RNAi-mediated depletion of SMNDC1 in these breast cancer cells significantly decreased *in vitro* growth under basal (Fig. 3.13d) and hypoxic conditions (Fig. 3.13e). Depletion of two additional candidate genes, LSM6 and PYCARD, also significantly reduced breast cancer cell growth (Fig. 3.14a-d).

To determine if isoleucyl tRNA modulation directly enhances translation of a growth-promoting gene in a codon-dependent manner, we performed mutagenesis studies by developing an SMNDC1 reporter gene. We constructed a reporter in which AUA codons in SMNDC1 were mutated to synonymous AUC codons. While the wildtype SMNDC1 protein became upregulated upon dual tRNA modulation, synonymous codon mutant SMNDC1 protein levels remained unchanged (Fig. 3.15a-b)—consistent with codon-dependent $tRNA^{Ile}_{UAU}$-driven enhancement of translation of this growth-promoting gene.

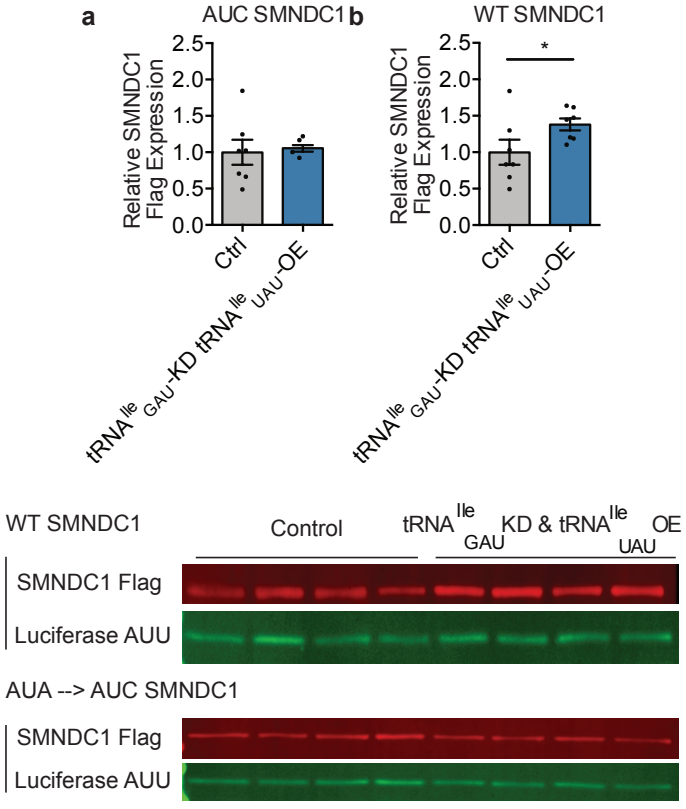

Figure 3.15 | **Increased expression of SMNDC1 protein levels is AUA codon dependent.**
(a,b) LICOR Western quantification of either Flag tagged all AUA to AUC codons (a) or wildtype (b) SMNDC1 expression relative to reporter control luciferase (all Ile AUU) 24 hours post transfection in either MDA control or $tRNA^{Ile}_{GAU}$ depletion $tRNA^{Ile}_{UAU}$ overexpression cells. Two-sided un-paired student's t-tests performed, p-values represented as * $p<0.05$.

Divergent isoleucyl tRNA modulation thus enhances the translation of a set of growth-promoting genes with high $tRNA^{Ile}_{UAU}$ synonymous codon usage scores.

We next hypothesized that there may exist a set of growth-suppressive genes that become repressed upon $tRNA^{Ile}_{GAU}$ depletion. We thus performed a similar analysis that integrated ribosomal profiling, proteomics, and relative AUC codon usage to identify $tRNA^{Ile}_{GAU}$-dependent genes. This identified four candidate genes that became repressed at the protein level upon dual $tRNA^{Ile}_{UAU}$/$tRNA^{Ile}_{GAU}$ modulation (Fig 3.16a). Of these candidates, RNAi-mediated depletion of two of these genes (EPHX1 and SIL1) significantly enhanced growth (Fig. 3.16b-e). These findings reveal a set of growth-suppressive genes that become repressed upon $tRNA^{Ile}_{GAU}$ depletion/$tRNA^{Ile}_{UAU}$ induction and uncover growth promoting and growth suppressive sub-networks downstream of these tRNAs.

Translational antagonism by isoleucyl tRNAs

We next sought to better understand the interaction of these isoleucyl tRNAs on codon-dependent translation. To do this, we performed polysome profiling studies (Fig. 3.17a). Polysome profiling revealed that relative to control cells, concurrent $tRNA^{ile}_{GAU}$ depletion and $tRNA^{ile}_{GAU}$ over-expression elicited a significant reduction in actively translating transcripts enriched in the AUC codon, which is cognate to the depleted $tRNA^{ile}_{GAU}$ (z-score 44.8 Fig. 3.17b) and an increase in polysome occupancy of transcripts enriched in the AUA codon, which is cognate to the over-expressed $tRNA^{ile}_{UAU}$ (z-score 23.6; robustness 10/10; Fig. 3.17c). Consistent with this, analysis of the aforementioned ribosomal profiling data revealed that upon dual $tRNA^{ile}_{UAU}$/$tRNA^{ile}_{GAU}$ modulation, there was a significant enrichment of ribosomal occupancy of AUA-containing transcripts and reduced occupancy of AUC-containing transcripts (Fig. 3.17d-e).

These concordant observations of global shifts in isoleucine codon enrichments and depletions in polysome profiling and ribosomal profiling studies support direct codon-dependent effects on translation.

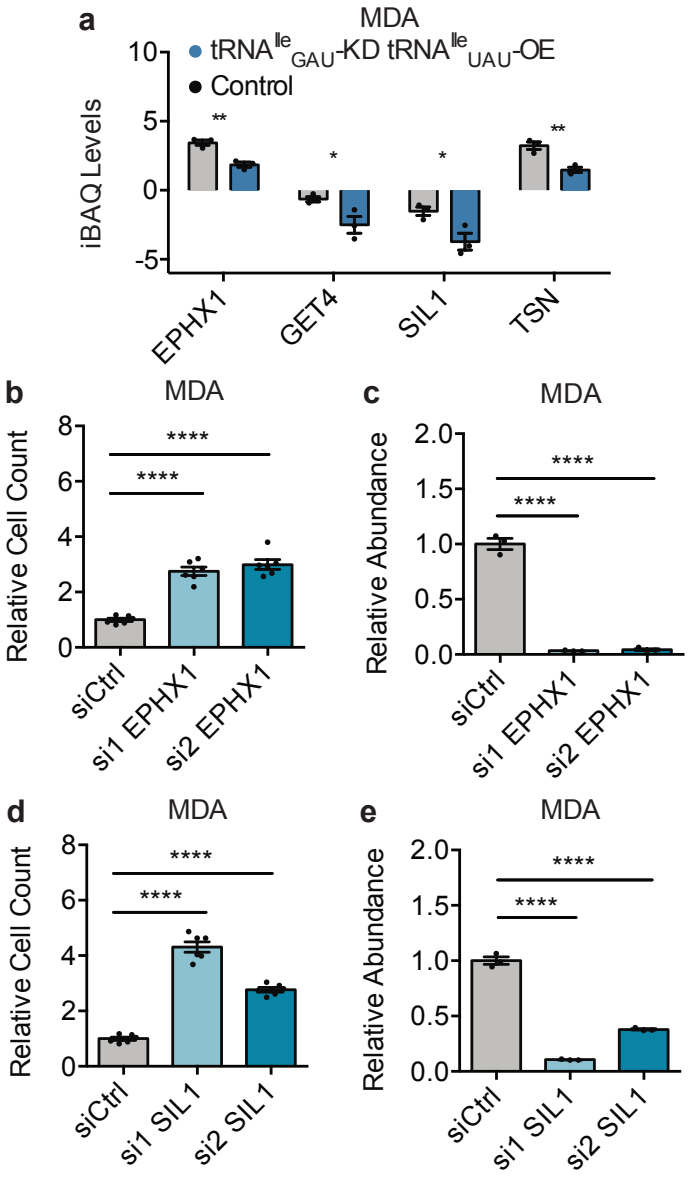

Figure 3.16 | **AUC enriched EPHX1 & SIL1 suppress breast cancer growth.**
(a) iBAQ values of four candidate downstream suppressor effectors, measured by label free quantification mass spectrometry, 3 biological replicates each.
(b) Relative cell count of MDA cells treated with control or EPHX1 siRNA for 3 days.
(c) RT-qPCR quantification of EPHX1 cDNA levels normalized to GAPDH on Day 2 of siRNA transfection.
(d) Relative cell count of MDA cells treated with control or SIL1 siRNA for 3 days.
(e) RT-qPCR quantification of SIL1 cDNA levels normalized to GAPDH on Day 2 of siRNA transfection.
Two-sided un-paired student's's t-tests performed, p-values represented as *, **, ***, **** as $p<0.05$, $p<0.01$, $p<0.001$, $p<0.0001$ respectively.

Importantly, polysome profiling revealed that over-expression of tRNA$^{ile}_{UAU}$ in tRNA$^{ile}_{GAU}$ depleted cells repressed translation of non-cognate AUC-containing transcripts and increased translation of AUA-enriched transcripts (Fig. 3.18a-b). This could be consistent with antagonism of AUA-enriched transcripts' translation by non-cognate tRNA$^{ile}_{GAU}$, which is relieved upon tRNA$^{ile}_{GAU}$ depletion. If our model of antagonism by these tRNAs

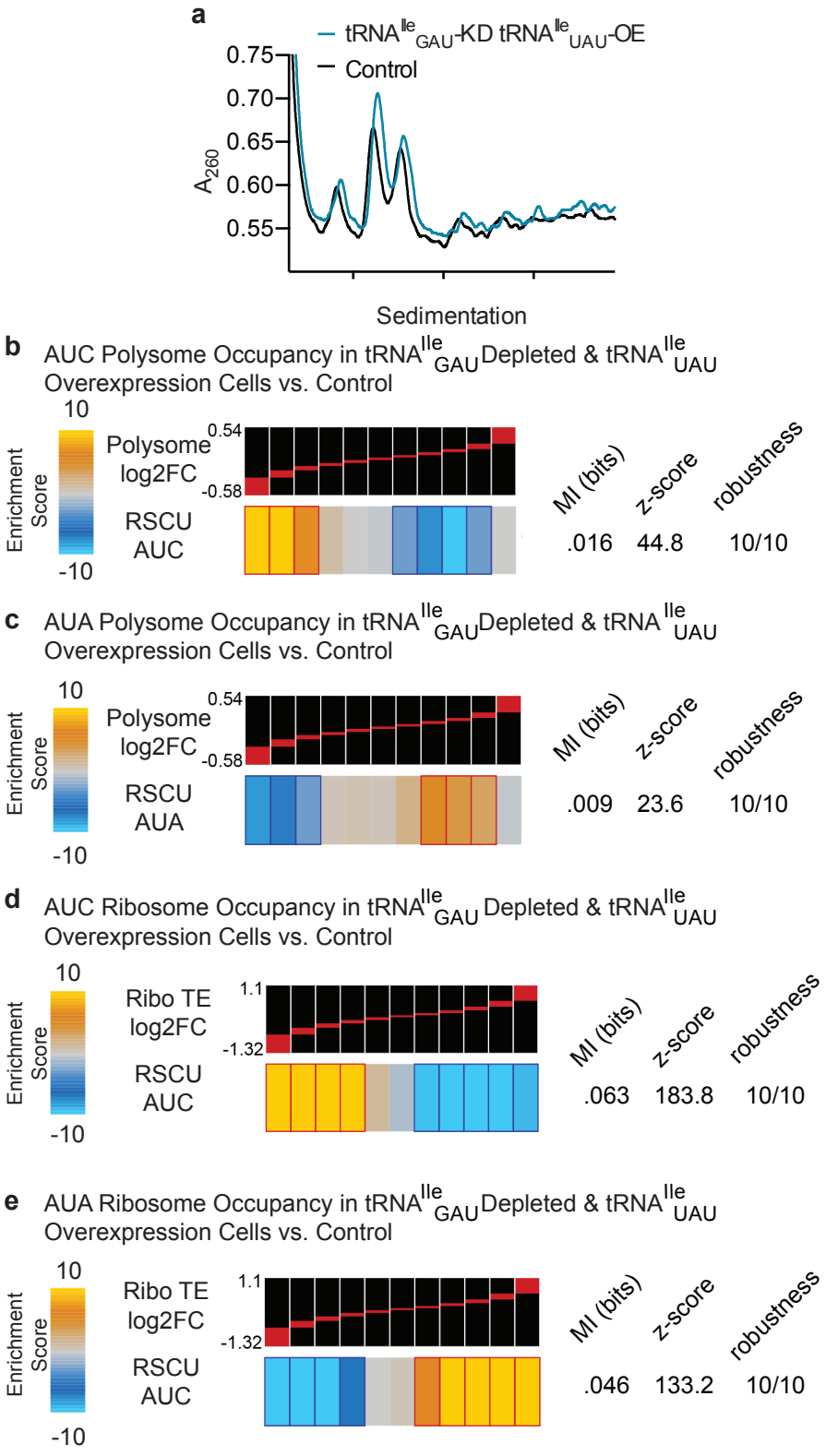

Figure 3.17 | **Codon dependent shifts in translational efficiency.** (a) Polysome traces of two samples, measured by UV spectrometry. (b)Hypergeometric distribution shown as a z-score of AUC codon enrichment of polysome transcripts represented as log2 fold change of $tRNA^{Ile}_{GAU}$ depleted $tRNA^{Ile}_{UAU}$ overexpression cells versus control MDA MB 231 cells, stratified in bins of 10, increased log2 FC from left to right. AUC codon representation visualized as a value ranging from -10 to 10 relative to the average. (c) Same as (b) except analyzed for AUA codon enrichment. (d) Hypergeometric distribution of log2 fold change translational efficiency values for $tRNA^{Ile}_{GAU}$ depleted and $tRNA^{Ile}_{UAU}$ overexpression cells versus control MDA MB 231 cells and enrichment of AUC codon content. (e) Same as (d) except analyzed for AUA codon enrichment. Codon content scored for by relative synonymous codon usage score.

at the ribosome is correct, we would expect that over-expression of $tRNA^{ile}_{UAU}$ may impair ribosome occupancy by $tRNA^{ile}_{GAU}$ in the context of reduced cellular $tRNA^{ile}_{GAU}$ abundance but not in the case of basal $tRNA^{ile}_{GAU}$ abundance, which would be consistent with a competitive inhibitor paradigm. To examine this, we quantified the polysomal ribosome-associated abundances of $tRNA^{ile}_{UAU}$ and $tRNA^{ile}_{GAU}$ as well as their cellular abundances. We reasoned that if these tRNAs are competing at the ribosome, then we

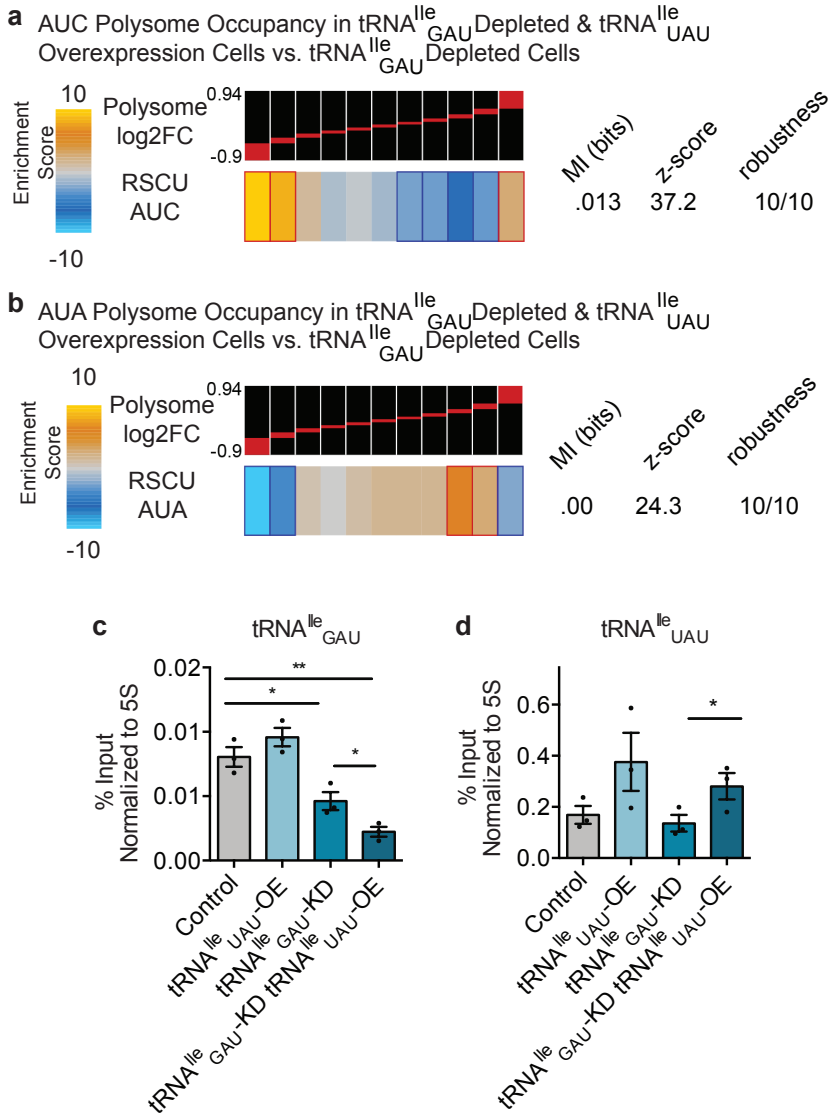

Figure 3.18 | **Polysome fractionation reveals $tRNA^{Ile}$ competition at the ribosome.** (a) Hypergeometric distribution shown as a z-score of AUC codon enrichment of polysome transcripts represented as log2 fold change of $tRNA^{Ile}_{GAU}$ depleted $tRNA^{Ile}_{UAU}$ overexpression cells versus $tRNA^{Ile}_{GAU}$ depleted MDA MB 231 cells, stratified in bins of 10, increased log2 FC from left to right. AUC codon representation visualized as a value ranging from -10 to 10 relative to the average. (b) Same as (a) except analyzed for AUA codon enrichment. (c,d) $tRNA^{Ile}$ quantification by specific $tRNA^{Ile}_{GAU}$ probe (c) or $tRNA^{Ile}_{UAU}$ probe (d) RT-qPCR normalized to 5S probes of $tRNA^{Ile}$ modulated MDA cells from polysome fractions, measured as % Input. Two-sided un-paired student's's t-tests performed, p-values represented as *, ** as $p<0.05$, $p<0.01$ respectively.

should observe reduced occupancy of one tRNA in the ribosome when the other tRNA translationally outcompetes it. We observed significantly reduced ribosomal occupancy of $tRNA^{ile}_{GAU}$ upon $tRNA^{ile}_{GAU}$ depletion and importantly, consistent with our model, observed a further reduction of ribosomal $tRNA^{ile}_{GAU}$ occupancy upon $tRNA^{ile}_{UAU}$ over-expression (Fig. 3.18c). $TRNA^{ile}_{UAU}$ over-expression did not reduce ribosomal occupancy of $tRNA^{Ile}_{GAU}$ in cells expressing basal levels of $tRNA^{ile}_{GAU}$ (Fig. 3.18c). We also saw a significant increase in $tRNA^{ile}_{UAU}$ occupany in dual modulated cells compared to $tRNA^{ile}_{GAU}$ depleted cells (Fig. 3.18d). These findings in sum are consistent with translational and phenotypic antagonism by these isoleucyl tRNAs.

Given our observed functional roles for these isoacceptor tRNAs in divergently regulating breast cancer cell growth, we reasoned that there may be a genetic signature of enrichment or depletion of codons cognate to these tRNAs in growth related genes within the human genome. To assess this, we performed computational analyses using the iPAGE pathway analysis algorithm—assessing significant genome-wide abundances for the codons cognate to $tRNA^{Ile}_{UAU}$ and $tRNA^{Ile}_{GAU}$ in gene sets in an unbiased manner. All coding transcripts in the human genome were ranked and binned by AUA or AUC relative synonymous codon usage (RSCU). Pathways that were significantly enriched ($p<10^{-3}$) in discrete bins were identified using the iPAGE mutual information framework (Fig. 3.19)[95]. Interestingly, transcripts most signficantly enriched in AUA codons (cognate to $tRNA^{Ile}_{UAU}$) were enriched in mitosis related gene sets such as metaphase, anaphase, and chromatid separation (Fig. 3.19a). Conversely, AUC codons (cognate to $tRNA^{Ile}_{GAU}$) were most significantly depleted from such mitosis related gene sets (Fig. 3.19b). We hereby propose a model in which isoleucyl isoacceptor relative abundances shift during metastatic progression, impacting competition of these tRNAs at the ribosome, which has

functional consequences through metastatic promoters and repressors on cellular growth phenotypes (Fig. 3.20).

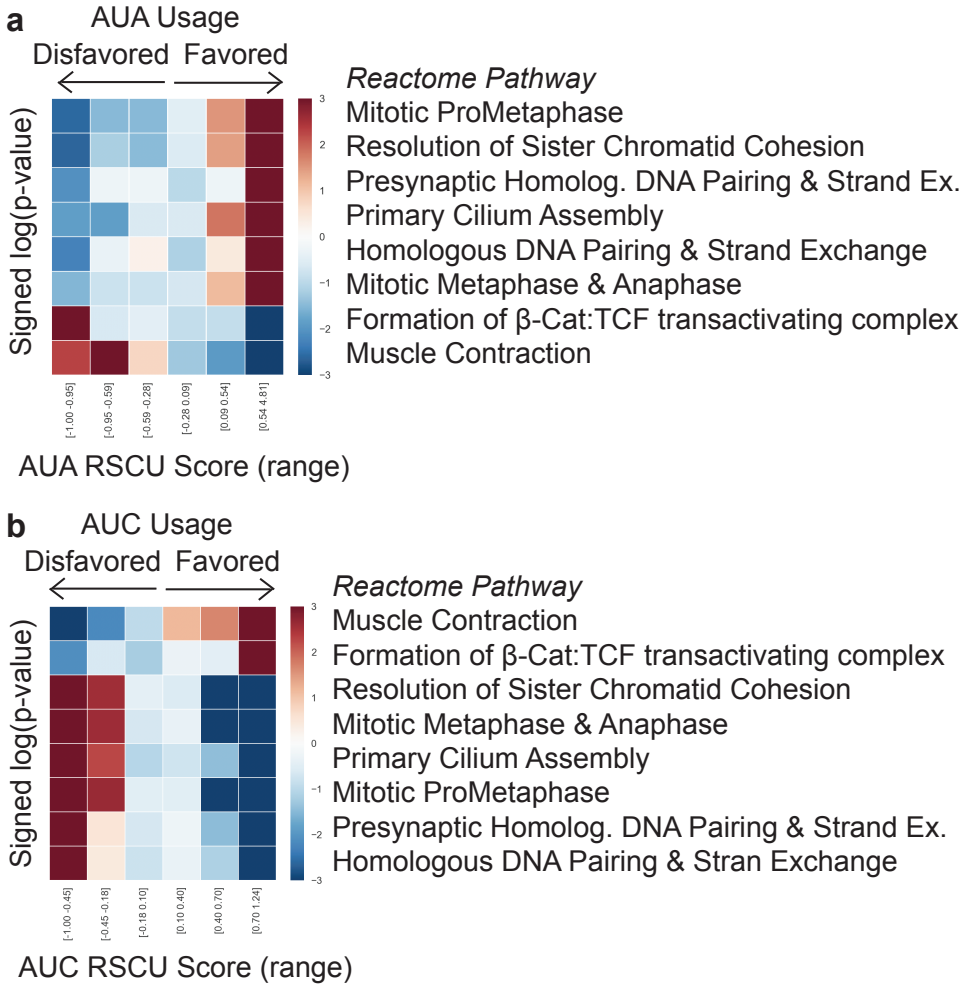

Figure 3.19 | **iPAGE identifies AUA enrichment & AUC depletion of mitosis-related pathways.**
(a,b) Reactome pathways significantly enriched in AUA (a) or AUC (b) by relative synonymous codon usage (RSCU) using iPAGE.

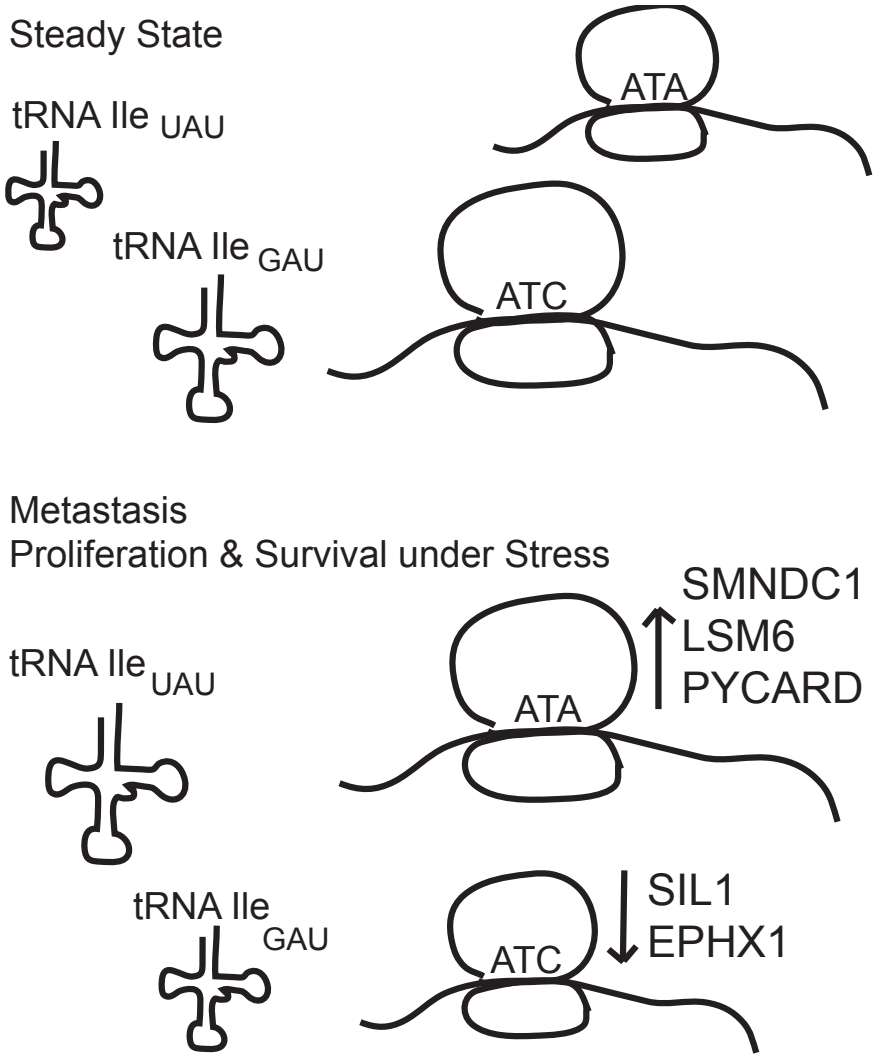

Figure 3.20 | **tRNA^{Ile} abundance shifts alter translational dynamics and metastatic phenotypes.**

Chapter IV: Discussion & Perspectives

Creatine Kinase, Brain has a dual role in promoting colorectal metastasis: the previously described survival benefit through increase of extracellular phosphocreatine in hypoxia, and modulation of immune cell activation and infiltration in gastrointestinal syngeneic models. The significance of secretion of Creatine Kinase Brain (CK-B) under conditions of hepatic hypoxia lies within an overall survival advantage for a heterogeneous population of cancer cells with variable capacity to survive in a hostile environment. Under physiological conditions, the release of CK-B from tumor cells with decreased expression of microRNAs 483-5p and 551a could increase in fitness for other disseminated colorectal cancer cells. Experiments to test whether the benefits of CK-B to tumor cells is primarily local or disseminated could be performed by simultaneous injections of tumors with normal or overexpression of CKB. The immunosuppressive effects through CKB's depletion of ATP could be studied in this way to determine whether anti-tumor immunity is affected at distant sites or in a systemic manner.

With the clinical challenges to therapy discussed previously in mind, Creatine Kinase Brain is a strong candidate for therapeutic benefit from multiple perspectives. Identified as a novel driver of metastatic progression in the liver[6], CK-B represents a target that is distinct from the "pipeline" of oncogenes that effect AKT signaling. Targeted therapy of CKB is therefore less complicated than EGFR patient stratification as discussed above. As CK-B is released into the extracellular space and mediates metastatic progression from this compartment, it is accessible in the blood for both therapeutic targeting and diagnostic purposes. CK-B was found to be significantly increased at the RNA and protein levels in advanced stage colorectal cancer patient samples compared to primary cancers in two independent cohorts, indicating the biology described in xenograft colorectal cancer cell lines is significant in human biology of metastasis. A therapeutically effective antibody for Creatine Kinase, Brain in the adjuvant setting or treatment of

colorectal cancer metastasis would block the enzymatic activity of extracellular CK-B to reduce the production of the metabolite phosphocreatine and the immunosuppressive molecule ADP. The inhibition of CK-B would reduce survival of metastatic colorectal cancer cells arriving at the metastatic site, and tip the balance of immune activation at the metastatic site, enabling the possibility of anti-tumor immunity. In the laboratory, we have performed a proof of principle inhibition experiment in vivo with the CKB inhibitor cyclocreatine. Treatment of mice with cyclocreatine for 2 weeks after intrasplenic injection of metastatic colorectal cancer cells decreased metastatic burden in the liver. Metastatic burden could also be significantly decreased with a single dose of adenoviral-associated virus packaged with miR-483-p and miR-551a. Current efforts in collaboration with the Tri-Institutional Therapeutics Discovery Institute are ongoing to develop a specific humanized antibody that enzymatically inhibits CKB. Current lead neutralizing antibodies are being tested *in vitro* using hypoxia survival assays with metastatic colorectal cancer cell lines that have high CKB expression, namely HCT116, LST174T LVM3B and the mouse syngeneic KPC cell lines. Initial tests suggest strong reduction in cell survival under 0.5% oxygen for 4 days, and *in vivo* studies will be performed in xenograft systems to understand the potential to reduce metastatic burden. We are optimistic that this strategy will lead to an effective therapeutic option for patients with metastatic gastrointestinal cancer.

Identifying specific residues that confer secretion of CKB is an important step in elucidating CKB's extracellular role. Our studies have all been conducting in the context of tumor progression in transplant and xenograft models, however CKB's extracellular role in cancer begs the question whether CKB is extracellular in physiological conditions. CKB has been shown to be involved directly in the differentiation and activation of immune cells, although whether this involves extracellular CKB it remains unknown[96].

We developed a mutant CKB mouse in which serine 6 is mutated to an alanine. Subsequent studies of the S6A CKB mutation *in vivo* will provide insight into whether CKB is normally secreted from tissues, and whether this lack of CKB secretion perturbs immune responses in other disease states, such as in intestinal inflammation.

Our observations in Chapter III reveal opposing roles for two isoleucyl tRNAs in the regulation of breast cancer metastatic colonization and cancer cell growth. We implicate $tRNA^{Ile}_{UAU}$ as a metastasis promoter tRNA and $tRNA^{Ile}_{GAU}$ as a metastasis suppressor tRNA in breast cancer. These tRNAs enhance or repress, respectively, the translation of growth-promoting and growth-suppressive genes. Our work uncovers the existence of growth-promoting and growth-repressive networks regulated by transcriptional modulation of specific isoleucyl isoacceptor tRNAs. Several of these genes have already been implicated in correlating with patient outcomes in breast cancer databases via RNA expression level. Investigating whether protein levels of these genes correlate with breast cancer stage and outcomes in patients is an important next step. Such growth promoting genes, such as SMNDC1 and LSM6, have been identified as proteins within the splicesome complex. Altering their protein expression through $tRNA^{Ile}_{UAU}$ abundance levels could enable distinct changes in isoform splicing, creating further downstream consequences for gene expression. Further study of these genes is warranted to uncover new facets of metastatic biology, and indirect effects of $tRNA^{Ile}$ modulation. We also provide evidence in support of competitive interference of translation by these isoacceptors at the ribosome. These molecular and functional studies implicating growth as a phenotype divergently impacted by the modulation of these tRNAs is supported by genome sequence analyses that reveal significant enrichment of the AUA codon cognate to the growth-promoting $tRNA^{Ile}_{UAU}$ in mitotic gene sets and depletion of the AUC codon, which is cognate to $tRNA^{Ile}_{GAU}$. Future studies are needed to discern the molecular basis

of isoleucyl-tRNA based competitive interference at the ribosome. A natural question that arises is the molecular basis of such interference at the ribosome. We speculate that structural constraints that preclude specific wobble base-pairing may be the basis for repression of decoding of non-cognate synonymous codons by a specific tRNA isoacceptor. In the context of reduced abundance of the cognate tRNA for such a codon, such as in the context of stress or disease, a non-cognate tRNA with disfavored base-pairing could occupy the ribosome at the non-cognate codon but not enable amino acid incorporation—competitively occluding access by the proper tRNA. Molecular and structural studies have expanded upon the Crick wobble hypothesis, describing the pairing between a single base at the first anticodon position and the multiple base types allowed at the third position of the codon[97,98]. While, $tRNA^{Ile}_{UAU}$ can decode its cognate AUA codons through Watson-Crick pairing, its proper pairing with its non-cognate AUC codon would be predicted to be impaired due to unfavourability of U-C wobbling[99,100]. Similarly, while $tRNA^{Ile}_{GAU}$ can decode cognate AUC codons through Watson-Crick pairing, its pairing with non-cognate AUC codons would be impaired since G-A wobbling is not allowed; the guanosine at the first position of the anticodon cannot base-pair with A, since the 2-amino group of G precludes G-A pairing[99]. We speculate that these antagonistic tRNAs can compete with the each other for binding to non-cognate codons, competitively impairing access and translational decoding by the other tRNA. Future biophysical studies are needed to determine the structural basis for such interference. Such isoacceptor antagonism can be biologically exploited. Over evolutionary time-scales, such isoacceptor antagonism could be used via enrichment or depletion of a given isoacceptor's codon in genes opposingly regulating a common phenotype. Future studies are warranted to search for additional potential examples of such antagonistic isoacceptor tRNA pairs in health and disease.

Materials & Methods

Cell Culture

MDA-MB-231, LS-174T LVM3B, KPC and their highly metastatic derivatives were cultured with DMEM media supplemented with 10% FBS, sodium pyruvate, and L-glutamine. HCC1806 Parental and derivate cell lines were cultured in 1x RPMI supplemented with 10% FBS, sodium pyruvate, 1mM HEPES as specified by ATCC. HCT116 and derivative cell lines were cultured in McCoy's Media with L-glutamine supplemented with 10% FBS and sodium pyruvate. All cell lines were regularly tested for mycoplasma infection and were negative. Each cell line was verified using STR testing, performed by the Integrated Genomics Operation at MSKCC. Hydrogen peroxide exposure was conducted by addition of 200uM hydrogen peroxide. Antibiotics, pen-strep and Fungizone were used temporarily after isolation of in vivo selected cell lines to prevent contamination.

Viral Production & Stable Cell Line Generation

Stable generation of cell lines was performed as described previously[1,6,7]. Lentivirus was generated using the ViraSafe lentiviral packaging system (Cell Biolabs) with Lipofectamine 2000 (Invitrogen) in HEK293T cells. Transductions were performed with 8ug/mL polybrene. Plasmids to overexpress $tRNA^{Ile}$ or with shRNAs targeting $tRNA^{Ile}_{GAU}$, , CKB, or PYCARD were cloned into the plko.1 puromycin (Addgene # 8453) or blasticidin (Addgene #26655) backbone with AgeI/EcoRI restriction sites[101,102]. shRNA sequences are in Table 2. CRISPRi stable cells lines were generated with lentiviral transduction of dCas9-KRAB (Addgene # 110820) and pSLQ plasmid (Addgene # 51024) cloned with a $tRNA^{Ile}_{GAU}$ targeting guide (5' TGAGCTAACCGGCCGCCCGA 3'), and then flow sorted for positive BFP+ and mCherry+ cells[103,104]. CRISPR generated cells were transduced with lentiCRISPRv2 (Addgene # 98290) cloned with specific guides targeting $tRNA^{Ile}_{UAU}$ loci (Guide 1: 5' GCGCTAACCGATTGCGCCAC 3', Guide 2: 5'

TGGCGCAATCGGTTAGCGCG 3′), or human CKB exon 1 (5′ CACCGCAGGTCGGGGAACTCGTCCT 3′) or mouse CKB (5′ CACCGAAAGCCGCTCGGCGTGCACT 3′) or eGFP sequence (5′ GGGGCGAGGAGCTGTTCACCG 3′). Cells were then either selected with 2ug/mL puromycin or 7.5ug/mL Blasticidin (Thermo Fisher Scientific).

Histology

Lungs were prepared by perfusion fixation with 4% paraformaldehyde through the circulation via the right ventricle. Lungs or extracted livers were then fixed in 4% paraformaldehyde overnight at 4°C. The samples were then embedded in paraffin and sectioned in 5 μm slices that were used for immunostaining. 5 μm sections at different depths were stained with hematoxylin and eosin (H&E).

Animal Studies

For lung metastasis assays, tail veins injections were performed in 5-6 weeks age matched female NOD SCID Gamma mice (The Jackson Laboratory #005557). Mice used for liver metastasis and CKB studies are male C57BL/6, and B6SF129 from The Jackson Laboratory, ages 6-8 weeks old. Subcutaneous tumor volume was measured using digital calipers and tumour volume was calculated as (small diameter)^2 x (large diameter) x π / 6. All graphs represent standard error of the mean of all tumor measurements. All animal work was conducted in accordance with protocols approved by the Institutional Animal Care and Use Committee at The Rockefeller University.

Serum Collection, Metabolite Extraction, & Mass Spectrometry

Mice previously intrasplenically injected with $5x10^5$ syngeneic pancreatic KPC cells were euthanized via cervical dislocation and then blood was extracted via intracardiac puncture in EDTA collection tubes to prevent clotting. Metabolite extraction and

subsequent Liquid-Chromatography coupled to High Resolution Mass Spectrometry (LC-HRMS) for polar metabolites of plasma was carried out using a Q Exactive Plus. For plasma, 5 µL was transferred to a new Eppendorf tube containing 45µL of ice cold 75:25:0.2 acetonitrile:methanol:formic acid *(v/v/v)* (Fisher Scientific) extraction solvent. Samples were vigorously vortexed and incubated on ice for 10 min. Samples were then centrifuged at 20,000 *g* at 4°C for 10 min and supernatants were transferred to LC vials. The injection volume for polar metabolite analysis and selected ion monitoring (SIM) was 5µl. A ZIC-pHILIC 150 × 2.1 mm (5 µm particle size) column (EMD Millipore) was employed on a Vanquish Horizon UHPLC system for compound separation at 25 °C. The autosampler tray was held at 4 °C. Mobile phase A is water with 20mM Ammonium Carbonate, pH 9.3, and mobile phase B is 100% Acetonitrile. The gradient is linear as follows: 0 min, 90% B; 22 min, 40% B; 24 min, 40% B; 24.1 min, 90% B; 30 min, 90% B. The follow rate was 0.15 ml/min. All solvents are LC-MS grade and purchased from Fisher Scientific. The Q Exactive Plus MS (Thermo Scientific) is equipped with a heated electrospray ionization probe (HESI) and the relevant parameters are as listed: heated capillary, 275°C; HESI probe, 350°C; sheath gas, 40; auxillary gas, 15; sweep gas, 1; spray voltage, 3.0 kV. A full scan range from 70 to 1000 (*m/z*) was used. For SIM acquisition method of ATP, 500-550 *(m/z)* was used. The resolution was set at 70,000. The maximum injection time was 200 ms. Automated gain control (AGC) was targeted at $10x10^6$ ions. Maximum injection time was 20 msec. Raw data collected from LC-Q Exactive Plus MS was processed on Skyline (https://skyline.ms/project/home/software/Skyline/begin.view) using a 5 ppm mass tolerance and an input file of *m/z* and detected retention time of metabolites from an in-

house library of chemical standards. The output file including detected *m*/*z* and relative intensities in different samples was obtained after data processing.

Immune Infiltrate Isolation and Profiling

Tumor bearing mice were euthanized via cervical dislocation and either subcutaneous tumors, metastatic livers, or draining lymph nodes were extracted and placed on ice in 6 well or 24 well plates (Corning). Lymph nodes were minced with two glass slides and resuspended in HBSS-2 media (Gibco) and kept on ice. Isolated tumor or metastatic liver tissues were place in 6 well plates and minced with scalpels. Digestion HBSS-2+ media (HBSS-2 with Ca^{2+} and Mg^{2+} (Gibco) supplemented with 2% FBS, 1mM sodium pyruvate, 25mM HEPES (Gibco #15630), 2mg/mL Collagenase VIII (Sigma #C2139) and 2mg/mL DNase I (Roche #10104159001), was added to minced tissues and incubated at 37°C for 45-50 minutes shaking at 80rpm. After digestion, 6 well plates are placed on ice and 10mL HBSS-2 media (**without** Ca^{2+} and Mg^{2+} supplemented with 2% FBS, sodium pyruvate, and 25mM HEPES) is added to triturate tissue, and then filtered with a 70um cell strainer (Corning) into a 50mL Falcon tube. The back of a 5mL syringe plunger was used to mesh aggregates through the filter, which was then rinsed with 5mL HBSS-2 media. Isolated heterogenous cells were then centrifuged at 1000rpm for 5 minutes. Percoll (Fisher) solutions were then prepared. The stock Percoll solution is 9:1 Percoll and 10x PBS. 70% and 35% Percoll solutions were the prepared with stock Percoll and HBSS-2 media. Cell pellets were resuspended in 5-6mL 35% Percoll, and transferred to 15mL Falcon tubes at room temperature. Glass Pasteur pipettes were then used to underlay 1-1.5mL 70% Percoll as 35% Percoll cell suspension rises slightly. Percoll gradients are then centrifuged at 2100rpm for 20 minutes **without deceleration brake** to ensure proper separation of immune cells from tumor and other cell types. Carefully, the top layer (~1-2mL) is

removed above the lymphocyte ring at the 70%/35% interface. A 200uL pipette was used to remove the red blood cell populations at the bottom, below the lymphocyte ring, carefully as to not disturb the lymphocytes. 8mL HBSS-2 media was then added and the isolated lymphocytes pellet after centrifugation of 1000rpm for 5 minutes. Cells are again washed with 8mL HBBS-2 to remove all Percoll. Cells are again spun and resuspended in 200-600uL HBSS-2 media depending on how many antibody panels will be utilized. Isolated tumor-infiltrating lymphocytes were then split into three equal volumes for myeloid staining, adaptive staining, and ex vivo stimulation. Stimulation media was comprised of HBSS-2 supplemented with 2% FBS, sodium pyruvate, HEPES, and 1:50 Brefeldin A (Sigma #B7651), 1:1000 Phorbol 12-myristate 13-acetate, i.e. PMA (Sigma #P8139), and 1:1000 Ionomycin (Sigma #I0634). Stimulation was added to lymphocytes as 200uL in a 96 well U-bottom plate and incubated at 37°C in a tissue culture incubator for ~2.5 hours. Isolated lymphocytes were washed once with FACS buffer (25mM HEPES, 2% FBS, 10mM EDTA (Quality Biological #351-027), and 0.1% sodium azide (Ricca #7144.8-16) in PBS). Cells were resuspended in 50uL Fc Block (anti-mouse CD16/32 1:200 in FACS buffer, clone 93; 101320, BioLegend) by gentle vortexing. 50uL 2x staining flow antibodies were added after 15-minute block, and then incubated for 20 minutes on ice. For the antibody panels pertaining to certain staining (myeloid, adaptive, stimulation, lymph node), please refer to Table 1 and 2. Cells were washed and then incubated with 1:7500 Zombie NIR at room temperature for 20 minutes to exclude dead cells during analysis. Cells were permeabilized with 1x permeabilization buffer (eBioscience) for 20 minutes and then incubated with intracellular antibodies (see Tables 1 & 2) in intracellular fixation buffer (eBioscience) for 20 minutes on ice. Cells were then washed with FACS buffer twice and resuspended in 200uL FACS buffer for analysis on a BD LSR-

Fortessa Flow Analyzer at the Flow Cytometry Resource Center at Rockefeller University. Flow antibodies were compensated using single stained UltraComp eBeads Compensations beads (Invitrogen) after 20-minute incubation and multiple washes. Myeloid antibody panels were compensated with single staining of each antibody with isolated tumor-infiltrating lymphocytes to better accommodate autofluorescence. For cell quantification, Count Bright counting beads (Thermo Fisher #C36950) were used according to the manufacturer's instructions to calculate cells/mg tumor tissue.

In Vitro BMDC Co-Culture

For isolation of bone marrow cells, wildtype mice were euthanized via cervical dislocation, and both legs were exposed and isolated, removing as much muscle and connective tissues as possible. The hind legs were cut at the hip to keep the femur bone intact. Leg bones were then incubated in 70% ethanol for 10 seconds for sterilization. Legs were then transferred into PBS in sterile dishes on ice in the tissue culture hood. Scalpels were used to brush off remaining muscle tissue. The proximal and distal ends of each bone were cut with autoclaved sterile scissors. Holding the open bone with fine forceps, HBSS2 media was flushed through the bone with a 10mL syringe and 27G needle into an open 50mL falcon tube until the bone was translucent. Bone marrow cells were then filtered with a 70uM filter (Corning) and the back of a 5mL syringe plunger was used to mesh aggregates through the filter. The filter was then rinsed with 5mL HBSS2 media. The suspension was then centrifuged at 1500rpm for 5 minutes and resuspended in RPMI -1640 supplemented with L-glutamine, Pen/Strep, and 1.95uL β-mercaptoethanol. Cells were then counted with a hemocytometer and plates $1x10^7$ per 10cm sterile petri dish (non-tissue culture treated) with 10mL RPMI supplemented media with 200ng GM-CSF () and cultured for several days. On Day 4, 5mL more media supplemented with GM-CSF

was added. On Day 7, bone marrow culture cells were harvested carefully with a cell scraper. Cells were centrifuged for 10 minutes at 1000rpm and then counted in a smaller volume of media. Split bone marrow derived cells into one tube ($1x10^6$ cells) per experimental conditions, and spin for 10 minutes at 1000rpm. At this day, GM-CSF treated bone marrow should be a mixed population of dendritic cells and macrophages. In parallel, colorectal cancer cells were seed $3x10^6$ cell per 10cm plate on Day 5. Their supernatant was collected on Day 7, 48 hours later, and spun down at 2000rpm for 5 minutes. The tumor conditioned media (T-CM) was then filtered through a 0.44μm filter. Remove supernatant from BMDC falcon tubes and resuspend in tumor conditioned media at a density of $1x10^6$/mL. Then plate BMDCs in T-CM 100uL/well in 96 U-bottom well plate. 24 or 48 hours later, Brefeldin A was added to samples 1:50 4 hours before isolation and analysis. 100uL Media with 1:25 Brefeldin A was added to each well. For isolation, cells were resuspended by pipetting and transferred to Eppendorf tubes. FACS buffer was added and cells were spun 1000rpm for 5minutes. Cells were washed once more FACS buffer. Cells were resuspended in 50uL Fc Block (anti-mouse CD16/32 1:200 in FACS buffer) by gentle vortexing. 50uL 2x staining flow antibodies were added after 15-minute block, and then incubated for 20 minutes on ice. For in-vitro experiments of dendritic cell activation the following antibodies were used: CD11c-FITC, CD40-PerCP-Cy5.5, MHCII-BV421, CD11b-BV605, CD45-BV785, CD86-PE-Cy7 – see Table M.3 for details. Cells were washed and then incubated with 1:7500 Zombie NIR at room temperature for 20 minutes to nullify dead cells. Cells were permeabilized with 1x permeabilization buffer (eBioscience) for 20 minutes and then incubated with intracellular antibodies (IL-12-APC, IL-10-PE) in intracellular fixation buffer (eBioscience) for 20 minutes on ice. Cells were then washed with FACS buffer twice and

resuspended in 200uL FACS buffer for analysis on a BD LSR-Fortessa Flow Analyzer at the Flow Cytometry Resource Center at Rockefeller University. Flow antibodies were compensated using single stained UltraComp eBeads Compensations beads (Invitrogen) after 20-minute incubation and multiple washes.

Immunofluorescence of Cells *In Vitro*

CKB Immunofluorescence studies were performed a day after plates $5x10^4$ colorectal cancer cells on a glass slide in a 6 well plate. Cells were washed with 1x PBS and then fixed with 4% paraformaldehyde for 15 minutes. For intracellular staining, cells were washed with 1x PBS three times, then permeabilized with previously chilled acetone (at -20°C) for 5 minutes. Cells with washed 1x PBS 3x and then incubated with 1% BSA in PBS for 30 minutes. Cells were then incubated with mouse anti-Flag M2 antibody (Sigma Cat. F3165), 1:500 in 1% BSA for 1 hour. Slides were then washed 3x with 1x PBS. Secondary antibody anti-mouse IgG-AF647 at a 1:1000 dilution was incubated in 1% BSA in PBS for 45 minutes. Slides were washed with PBS 3x and then incubated with either Phalloidin 565 at 1:20 in 1% BSA for 25 minutes at RT, or with anti-LAMP1 1 (Abcam ab24170). Slides were washed and then incubated with DAPI 1:1000 in PBS for 5 minutes at RT. Coverslips were mounted onto glass slides with Prolong Gold.

For extracellular immunofluorescent studies, cells were fixed with 4% PFA was mentioned above but were not treated with acetone. Cells were instead blocked with 1% BSA for 30 minutes in PBS. Slides were then washed with 1x Annexin V Binding Buffer (100mM HEPES pH 7.4, 140mM NaCl, 25mM $CaCl_2$) twice, and incubated with Annexin V Biotin 1:100 in Annexin V Binding Buffer for 30 minutes. Cells were then washed with Annexin V Binding Buffer three times. The secondary antibody Streptavidin-Alexa Fluor 647 was incubated at a 1:1000 dilution in ABB for 45 minutes. Slides were again washed

with ABB three times, followed by primary incubation with anti-CKB or anti-Flag M2 antibody at 1:100 for 1 hour in 1% BSA, followed by secondary incubation with anti-mouse/rabbit IgG Alexa Fluor 555 1:1000 for 45 minutes after washes. Cells were also counterstained with DAPI 1:1000 for 5 minutes and mounted on glass slides with Prolong Gold (Thermo Fisher). Fluorescent intensity was measured on Inverted TCS SP8 laser scanning confocal microscope (Leica) at 60x magnification with DAPI, 555 and 647 default settings at the Bioimaging Resource Center at Rockefeller University.

Western Blot

Cells seeded a day previously were washed with 1x PBS and then lysed with either RIPA buffer or 20mM Tris HCl pH 8.0, 1% NP-40, 2mM EDTA with 1x protease inhibitors (Roche). Protein concentrations were quantified with a BCA Kit (Thermo Fisher) and normalized. Protein lysates were run at 200V for an hour through either a 4-12% Bis-Tris or 3-8% Tris Acetate gel (Invitrogen), and then transferred at 300mA for one hour in 15% methanol 1x Transfer Buffer on a methanol activated PVDF membrane. Membranes were then stained with Ponceau and blocked for one hour in Odyssey® Blocking Buffer. Primary antibody incubations occurred overnight at 4^{o}C on a rocker at the following concentrations: alpha tubulin 1:1000, (Proteintech) SMNDC1 1:500 (Proteintech), CKB (Abcam #ab38212), CKB (Proteintech #151357), Alix (Cell Signaling 3A9 #2171), TSG101 (Abcam #30871), HSP70 (Cell Signaling #4876), GAPDH (Genetex GTX100118), Renilla luciferase, Flag (. Membranes are then washed with 0.05% Tween 20 PBS three time and incubated with mouse or rabbit fluorescent IRDye® conjugated secondary antibodies 1:20,000 (LI-COR Biosciences), or horseradish peroxidase (HRP, GE Health Sciences) conjugates 1:1000 for one hour. Membranes were subsequently washed three times and imaged and quantified using the Odyssey® Sa Infrared Imaging System at the Rockefeller

University Center for High Throughput Screening or a developer using Pierce ECL plus kit. LICOR Quantification was done using the Image Studio LiteTM software.

Conditioned Media Studies

Colorectal or pancreatic cancer cells were plated in equal numbers (~ 3 million cells) in 10cm plates and left overnight. Media was then aspirated, and the cells were washed with 1x PBS three times, before addition of serum free (FBS free) DMEM supplemented with sodium pyruvate and glutamate. Conditioned media was collected after 6 hours, and spun down at 2000rpm for 10 minutes to remove debris and cells. Supernatant was moved carefully to another 15mL Falcon and kept on ice. Supernatant was then concentrated in 10K Millipore filters up to 15mL Media. Filters were spun at 4000rpm for 25-30 minutes to concentrate to ~1mL. Media was then collected after washing walls to collect all proteins. Concentrated supernatant was then transferred to 0.5mL 10K Millipore filters and spun at top speed in a cold tabletop centrifuge for 20 minutes. Supernatant was then run for Western blot analysis or stored temporarily at -20^{o}C.

Annexin V Biotin Immunoprecipitation

Colorectal cancer HCT116 cells were plated in equal numbers (~ 7.5 million cells) in 15cm plates and left overnight. Media was then aspirated, and the cells were washed with 1x PBS three times, before addition of serum free (FBS free) McCoy's Media supplemented with sodium pyruvate. Conditioned media was collected after 6 hours, and spun down at 2000rpm for 10 minutes to remove debris and cells. Supernatant was moved carefully to another 15mL Falcon and kept on ice. Filters were spun at 4000rpm for 25-30 minutes to concentrate to ~1mL. Media was then collected after washing walls to collect all proteins. 0.5 volumes of Total Exosome Isolation Reagent (Life Technologies) was added to the concentrated media and rocked overnight at 4^{o}C. The CM/Reagent was spun at 10,000g for 1 hour with vesicles now pelleted. Vesicle pellet was then resuspended in PBS

with 1x protease inhibitors and kept on ice. Annexin V binding buffer with Ca^{2+} (100mM HEPES pH7.4, 140mM NaCl, 25mM $CaCl_2$) swas added to a total volume of 500uL. 1uL Annexin-V Biotin per 100uL and incubated on a rocker for 15 minutes at RT. Streptavidin Dynabeads M-270 (Invitrogen) were resuspended and 100uL dynabeads was washed 3x with binding and wash buffer (B&W: 5mM Tris HCl pH 7.5, 0.5mM EDTA, 1mM NaCl). B&W final wash was removed from the beads using the magnet, and 500uL Annexin V Biotin vesicle solution was added to the streptavidin beads, and incubated for 30 minutes at RT. A magnet was used to separate beads from the solution, and the flow through was collected for downstream analysis. Beads were then washed 5x with 0.1% BSA PBS. To remove vesicles, 10mM EDTA pH 8.2 with 95% formamide was added incubated at 65°C for 5 minutes to dissociate biotin-streptavidin. For direct Western analysis, samples were boiled at 95°C for 5 minutes with 1x SDS buffer.

Imagestream

Colorectal cancer cells were trypsinized, neutralized, and then resuspended in PBS with 1:1000 CFSE dye. Incubate at room temperature rocking for 20 minutes. Cells were then spun down and resuspended in normal media to quench any extracellular CFSE dye. Incubate resuspended cells with anti-CKB 1:100 for 20 minutes, then spin down in 4°C tabletop centrifuge at 1500 rpm for 5 minutes. Cells were washed briefly with PBS then respun. Incubate cells with secondary rabbit Alexa Fluor 647 antibody for 15 minutes. Spin cells and then resuspend in FACS Buffer (25mM HEPES, 2% FBS, 10mM EDTA (Quality Biological #351-027), and 0.1% sodium azide (Ricca #7144.8-16) in PBS). Cells were then analyzed on the Amnis ImageStream-X at the Flow Cytometry Resource Center at Rockefeller University.

Chromatin Immunoprecipitation

MDA-MB-231 and LM2 cells were plated in 15cm plates (approx. 12 million cells) in biological replicate. 1% formaldehyde was added to cells to crosslink at 37oC for 10 minutes, and quenched with glycine at a final concentration of 0.14M for 30 minutes at room temperature. The plates were put on ice, the media was removed and cells were washed with ice cold PBS twice. 500uL PBS with 1x HALT protease inhibitors (Thermo) were added and cells were scraped and put in an Eppendorf on ice. Cells were pelleted at 4000rpm in a refrigerated centrifuge for 4 minutes. The cell pellets were resuspended in 400uL Lysis buffer (1% SDS, 50mM Tris HCl pH 8.0 20mM EDTA, protease inhibitors (Roche)) and incubated on ice for 10 minutes. Lysates were then sonicated to produce DNA fragments between 200 – 1000bp with settings Amplitude 70, 10 sec on 30 sec rest for three repetitions on Sonicator S-4000 (Branson) with Microtip and Ultrasonic Liquid Processor (Misonix). Lysates were kept on ice during sonication to prevent protein degradation. Lysates were then clarified by centrifugation at max speed at 4oC for 10 minutes. Equivalent amounts of lysate were added to separate eppendorfs, saving some lysate for input samples. Either 5ug rabbit IgG or 5ug POLR3A (Cell Signaling #12825S) were added, with a final volume of 1ml with protease inhibitors of dilution buffer (16.7mM Tris HCl pH 8.0, 0.01% SDS, 1.1% Triton X-100, 1.2mM EDTA, 167mM NaCl). Lysate and antibody mixtures were incubated overnight at 4oC with rotation. 50uL Protein G Dynabeads were added to each sample after washing and incubated at 4oC for 2 hours with rotation. Tubes were then placed on a magnet for 2 minutes, discarding the supernatant. The following washes were performed, twice each for 5 minutes at 4oC in the following order – low salt (140mM NaCl, 50mM HEPES, 0.1% SDS, 1% Triton X-100, 0.1% deoxycholate, 1mM EDTA) high salt (500mM NaCl, 50mM HEPES, 0.1% SDS, 1% Triton X-100, 0.1% deoxycholate, 1mM EDTA), LiCl (250mM LiCl, 20mM Tris HCl pH

8.0, 0.5% NP-40, 0.5% deoxycholate, 1mM EDTA) and TE Buffer (10mM Tris HCl pH8.0, 1mM EDTA). 100uL Elution buffer (50mM Tris HCl pH8.0, 1mM EDTA) was then added to the beads and incubated at 65oC overnight shaking to enable elution. Elution was transferred to a new tube and repeated for a final volume of 200uL per sample. 1uL of 10mg/mL RNase A was added to each sample (including input samples) and incubated at 37oC for 30 minutes. 2uL of Proteinase K was added (10mg/mL) and incubated for 2 hours at 56oC. DNA was then purified using the DNA Clean and Concentrator Kit (Zymo Research). Enrichment of Polymerase III bound loci was confirmed with genomic tRNA qPCR primers and quantified as Percent Input over IgG. The Input and IP DNA samples were then PCR amplified with Illumina barcodes to construct a multiplexed library. The library was quantified using TapeStation and sequenced on the 50 SR HiSeq at the Rockefeller Genomics Resource Center. Analysis description TBD.

In Vivo Selection

Several female Nod SCID Gamma (NSG) (Jackson # 005557) mice were injected at 5 weeks of age intravenously via tail vein with 150,000 parental HCC1806 cells and monitored via bioluminescence for variable number of weeks. Once photon flux of these lungs reached 10^7 or 10^8 via bioluminescence IVIS imaging (IVIS Lumina II), the lungs were extracted post euthanasia under sterile conditions and according to IACUC protocol and guidelines. The lungs were put on a sterile 6cm tissue culture dish and minced with razor blades. Lung tissue extracts were re-suspended in 20mL RPMI Media supplemented with FBS, sodium pyruvate and HEPES with 15mg/mL Collagenase IV (Worthington). Cells were incubated at 37oC for 30 minutes with shaking to allow for digestion. Tissue extracts were then spun down at 1000rpm for 5 minutes at 4oC and resuspended in RPMI media without Collagenase IV. Cells were filtered with an 100um filter (Corning) and spun down again. Cells were then treated with 5mL ACK Lysis Buffer and left at room

temperature for 5 minutes. Cells were spun again and resuspended in 1mL Optiprep solution 1 (2:1, Optiprep:Media). A gradient was constructed with an additional 4mL Solution 1, overlain by 3mL Optiprep Solution 2 (2.2:1, Solution1: Media). 1mL Media was overlain and the gradient was spun down for 20 minutes at 1000rpm 4oC. Viable cells were collected from the top of the gradient and washed twice with RPMI media. Cells were then plated in 75cm filtered flasks with PenStrep and Fungizone added to the RPMI Media. The cells were cultured for approximately a week to reduce stromal cell survival and then tested for mycoplasma. To generate an in vivo selected line twice, these lung metastatic 1 (LM1) generation cells were then re-injected at 150,000 tail vein and the process was repeated.

tRNA Capture qPCR

tRNA quantification by RT-qPCR was performed as described previously1.RNA purified with Norgen Total Purification Kit was quantified using a Nanodrop. Normalized RNA across samples is added to a hybridization mixture (final concentration 10mM Tris HCl pH 7.4, 50mM NaCl, 1mM EGTA pH 8.0) with 2uM Hybridization probes. Hybridization probes specific for the following tRNA were used: Ile TAT Left 5' /5Phos/AAGTACCGCGCGCTACCGATTGCGCCACTGGAGCGATCGTCGGACTGT AGAA, Ile TAT Right 5 CGTGTGCTCTTCCGATCTTGCTCCAGGTGAGGCTCGAACTCACACCTCGGCATTA T', Ile GAT Left 5' /5Phos/CAGCACCACGCTCTACCAACTGAGCTAACCGGCCGATCGTCGGACTGT AGAA, Ile GAT R 5' CGTGTGCTCTTCCGATCTTGGCCGGTGCGGGAGTCGAGCCCGCGCCTTGGTGTTA T 3'. Each 'left' probe has a 5' phosphate to enable subsequent ligation. RNA and probe mixture is hybridized using a thermocycler and brought to RT. 1x SplintR ligase buffer,

SplintR Ligase (NEB) and RNase Inhibitor (Promega) are added and incubated at room temperature for 2 hours. An additional ligation step with T4 Ligase is performed overnight at 16oC. The RNA is then degraded with RNase A (Thermo Fisher) & H (NEB) for 30 minutes at 37oC. The ligated probe reaction is then diluted 1:50 and quantified using primers (Forward 5′ CGTGTGCTCTTCCGATCT 3′ & Reverse 5′ GATCGTCGGACTGTAGAA 3′) specific to the probe backbone by RT-qPCR. 5S and 18S probes were used as loading controls: 5S Left 5′ 5PHOS/CTGCTTAGCTTCCGAGATCAGACGAGATCGGGCGCGATCGTCGGACTG TAGAA 3′ 5S Right 5′ CGTGTGCTCTTCCGATCTCCAGGCGGTCTCCCATCCAAGTACTAACCAGGCCCG ACC 3′ or 18S Left 5′ 5PHOS/CCTAGTAGCGACGGGCGGTGTGTACAAAGGGCGCCGATCGTCGGACTG TAG 3′ 18S Right 5′ CGTGTGCTCTTCCGATCTCCGATCCGAGGGCCTCACTAAACCATCCAATC 3′.

Northern Blot

RNA was purified using Norgen total RNA Purification kits according to manufacturer's instructions. 5ug purified RNA was run on 10% TBE-Urea gels at 200V for 1 hour, and transferred to a Hybond-N+ membrane (GE) at 150A for 1 hour. RNA was then crosslinked to the membrane at 240mJ/cm2, and blocked with Oligo Hybridization Buffer (Ambion) for 1 hour at 42oC. Northern probes were labeled with 32P ATP with T4 PNK (NEB), purified with a G25 column (GE Healthcare), and hybridized in Oligo Hybridization Buffer overnight at 42oC. Membranes were washed with 2X SSC 0.1% SDS Buffer, then with 1X SSC 0.1% SDS Buffer. Films were developed at varying times subject to radioactivity of membrane. Probe oligo sequences for Ile TAT Intron: 5′ ACUGCUGUAUAAGUACCGCGCGC 3′ and Ile TAT 5′ cucggcauuauaaguaccgcgcgc 3′

and U6 5′ CACGAATTTGCGTGTCATCCTT 3′. Membranes were stripped with 0.1% SDS in boiling water and allowed to cool to room temperature. Quantification was performed with ImageJ and normalized to U6 levels.

tRNA Sequencing with TGIRT

Sequencing of tRNAs using the TGIRT enzyme was a modified version of the protocol described in11,12. Small RNAs were isolated using Norgen microRNA Purification kit according to manufacturer's instructions. R1R2 comp DNA Oligo (5′ GAT CGT CGG ACT GTA GAA CTA GAC GTG TGC TCT TCC GAT CTN 3′) was labeled with radioactive P32 using T4 PNK (NEB). The R1R2 radioactive DNA oligo was then annealed to the R1R2 RNA (5′- rArGrA rUrCrG rGrArA rGrArG rCrArC rArCrG rUrCrU rArGrU rUrCrU rArCrA rGrUrC rCrGrA rCrGrA rUrC/3SpC3/ 3′) with a final concentration of 10mM Tris HCl pH 7.5 & 1mM EDTA and brought to room temperature. 300ng of each RNA sample was then reverse transcribed with the TGIRT®-III enzyme (InGex, 10uM) with the lableled R1R2 RNA/comp DNA heteroduplex for 1 hour and was terminated with 2.5uL 2M NaOH. RT reactions were then neutralized with varying amount of 5M HCl and size selected on a 10% TBE Urea gel. A radioactive ladder was used to determine size, and products above 100nt were excised and eluted overnight in DNA extraction buffer (300mM NaCl, 10mM Tris HCl pH 8.0, 1mM EDTA), and then precipitated overnight and resuspended in 10mM Tris HCl pH 8.0. The RT products were then circularized using Circ Ligase II (Epicentre) overnight at 60oC. Circularized DNA was then PCR amplified with Pfusion with 2.5uL cDNA as Input with 15 cycles. PCR products were size selected after polyacrylamide gel separation around 140bp. Samples were then pooled and sequenced on a MiSeq 150 SR at the Rockefeller University Genomics Resource Center. Analysis description TBD.

RT qPCR

RNA was purified using Norgen total RNA Purification kits according to manufacturer's instructions. 1ug purified RNA was used for cDNA production with Superscript III reverse transcriptase (Thermo Fisher Scientific) using oligo dT or random hexamer (for pre-tRNA experiments) as a template. cDNA was diluted 1:5 and quantified with Sybr Green Master Mix (Thermo). ddCT levels were quantified through normalization to GAPDH or 18S with biological replicates. Primer sequences are available in the Supplemental Material.

tRNA Fluorescence In Situ Hybridization

Breast tissue microarrays were obtained from Biomax (BC08118 & BR1005b). Slides underwent deparaffination via 5 minute incubations in xylene 2x, 100% Ethanol, 2x, 70% Ethanol, 50% Ethanol, and subsequently molecular grade water. Antigen retrieval was performed with 1x Citrate Buffer pH 6.0 in a microwave for 20 minutes. Slides were cooled to room temperature, then tissue regions were isolated with a PAP pen. Slides were incubated in 0.13M 1-methylimidizaole 300mM NaCl pH 8.0 solution twice for 10 minutes each. Next slides were incubated with 0.16M N-(3-Dimethylaminopropyl)-N-ethylcarbodiimide hydrochloride (EDC) (Sigma Aldrich) in the 1-methylimidazole solution for 1 hour at RT to preserve small RNAs[105]. Slides were then washed with 0.2% Glycine in Tris buffered saline (TBS) pH 7.4, then in TBS twice. Pre-hybridization of slides occurred with 1X ISH (Exiqon) buffer at 53°C for 1 hour. 40nM tRNA double DIG labeled LNA Probe targeting against $tRNA^{Ile}_{UAU}$ (Sequence 5′ CA+GGTGAGGCTCGAACTCACAC+C+TCGGCAT+T+A 3′ with +N indicating LNA at that nucleotide) (Qiagen) in 1X ISH buffer was denatured at 95°C for 5 minutes followed by cooling on ice for 1 minute. The LNA probe was added to the slide (and covered with a glass coverslip to prevent evaporation) and hybridized overnight at 52°C.

Slides were then washed with 4X SSC, 2X SSC, 1X SSC, and 0.5X SSC in 50% formamide for 20 minutes each, then washed with 100mM Tris-HCl pH 7.4 150mM NaCl (TN buffer) for 5 minutes. Slides were blocked with 1X Blocking Reagent (Roche) in TN buffer for 1 hour at RT. Anti-DIG POD in TN blocking buffer was added 1:100 and incubated for 2 hrs. Slides were washed 3x for 5 minutes in TN buffer with 0.05% Tween-20 (TNT). FITC-tyramide solution 1:100 in 1x amplification reagent (TSA) was incubated on slides for 10 minutes at RT. Slides were subsequently washed 3x 5min with TNT buffer. Samples were washed with PBS and stained with DAPI for 5 minutes, then mounted with Prolong Gold anti-fade solution (Thermo Fisher). Fluorescent intensity was measured on Inverted TCS SP8 laser scanning confocal microscope (Leica) at the Bioimaging Resource Center at Rockefeller University and quantified by mean fluorescence intensity relative to DAPI. Quantification was performed blind.

Ribosomal Profiling

Ribosomal profiling was performed based on the McGlincy & Ingolia protocol. Briefly, cells were plated in 15cm dishes at 50% confluency the day before collection. The media was aspirated, and the cells were washed 5mL ice cold PBS, and aspirated. The plate was then submerged in liquid nitrogen to freeze the cells. 400uL ice cold lysis buffer was added to the plate, and scraped immediately. Each lysate was kept on ice until all plates were collected. Several plates were combined with lysis buffer totaling 1mL per biological replicate. Lysates were then triturated ten times with a 26 gauge needle. Lysates were clarified at top speed for 10 mins in a cold bench top centrifuge and the supernatant was recovered and snap frozen in liquid nitrogen, then stored at -80 oC. Lysates were quantified with Quant-iT Ribogreen assay (Life Technologies) and 60ug total RNA per sample was incubated with 3uL RNAse I (Epicentre #N6901K) for 45 minutes at RT with light shaking. 10uL SUPERase*In RNase Inhibitor (Invitrogen) was added to stop

digestion, and the RNA was transferred to a 13mm x 51mm polycarbonate ultracentrifuge tube. 900uL Sucrose cushion (1M Sucrose with 20U/mL SUPERase*In in polysome buffer4) was underlayed and spun at 100,000 RPM at 4oC for 1 hour. With ribosomes pelleted, the supernatant was pipetted out of the tube. 300uL Trizol was added to the pellet and resuspended. RNA was subsequently purified with the Direct-zol kit (Zymo). RNA was then precipitated overnight and resuspended after ethanol washes in 5uL 10mM Tris HCl pH 8.0. Ribosome footprints were isolated after running a 15% TBE-Urea gel and the RNA was excised within the range of 17nt – 34nt and then precipitated overnight. RNA fragments were then dephosphorylated with T4 PNK and ligated to a DNA linker with T4 Rnl2(tr) K227Q (NEB #M0351S) for 3 hours with distinct linker barcodes. Unligated linkers were depleted with yeast 5′-deadenylase (NEB #M0331S) and RecJ exonuclease (Epicentre #RJ411250) at 30oC for 45 minutes. Ligations were then purified with the Oligo Clean & Concentrater kit (Zymo) and samples were pooled. Ribo Zero Gold was then used to deplete ribosomal RNAs (2 reactions were used, and the 50oC step was omitted, Illumina). RNA was then purified using Oligo Clean & Concentration kit. The pooled ligations were then reverse transcribed using Superscript III at 55oC for 30 minutes, with RNA templates hydrolyzed by 2.2uL 1M NaOH. Samples were purified with the Oligo Clean & Concentrator kit and run on a polyacrylamide gel and the RT product was excised above 76nt. Gel slices were incubated with DNA gel extraction buffer overnight after gel was broken up with gel breaker tubes (IST Engineering) and precipitated overnight. The RT product was resuspended in 10mM Tris HCl pH 8.0 and circularized with CircLigase II at 60oC for 1 hour. qPCR quantification of circulization products were performed to quantify number of cycles sufficient for library preparation, with the concentration estimated at 713pM. 8 cycles were used to amplify the library with Pfusion with the primers indicated, NI-799 and NI-7984. Products were purified and size

selected at >136bp, primarily at 160bp. The library was then precipitated, quality checked with Tapestation and sequenced on the NextSeq High Output 75 Single Read at the Rockefeller University Genomics Resource Center. Concurrently 1ug total RNA was prepped for RNA sequencing according to the manufacturer's instructions (Illumina. Analysis was performed as described previously[72].

Polysome Profiling

Polysome profiling was adapted from Gandin et. al.'s protocol and with direction and assistance from Dr. Alison Ashbrook in Dr. Charlie Rice's laboratory[106]. The day before cell collection, 7.5 million MDA-231 were plated in 15cm plates (2 plates per experimental biological replicate) in normal DMEM media supplemented with 10% FBS. Cells were plated to achieve approximately 80% confluency at collection time to optimize polysome content. Each plate was treated for 5 minutes at 37oC with DMEM with 100ug/mL cycloheximide (). The plate was then transferred to ice and the cycloheximide media was aspirated. Cells were washed twice with ice cold 1x PBS with 100ug/mL cycloheximide. All PBS was then aspirated carefully and the 15cm plate was flash frozen in liquid nitrogen. 425uL Lysis Buffer (5mM Tris HCl pH 7.5, 2.5mM MgCl2, 1.5mM KCl, 100ug/mL cycloheximide, 2mM DTT, 0.5% Triton X-100, 0.5% sodium deoxycholate, and 100 units of SUPERase*In RNase Inhibitor (Invitrogen)1x Protease Inhibitors EDTA-free) was then added to the plate and cells were scraped and transferred to an eppendorf on ice. Lysates were then spun at high speed at 4^{o}C for 7 minutes to pellet nuclei. Supernatant was transferred to a new tube and the RNA concentration was measured using the Quant-iT Ribogreen assay (Life Technologies). 64ug RNA lysate was used for polysome fractionation. 10-50% Sucrose gradients were prepared the day before ultracentrifugation. Ultracentrifuge polyallomer tubes (Beckman Coulter, Cat #331372) were marked halfway and ~5.5mL 10% sucrose polysome gradient buffer (20mM Tris

HCl pH 7.5, 140mM KCl, 5mM MgCl2, 10% Sucrose, 100ug/mL cycloheximide, 0.5mM DTT, 20U/mL SUPERase*In) was added with a 10mL sterile syringe to 1/8 inch above the line. 50% sucrose polysome gradient buffer (20mM Tris HCl pH 7.5, 140mM KCl, 5mM MgCl2, 50% Sucrose, 100ug/mL cycloheximide, 0.5mM DTT, 20U/mL SUPERase*In) was then underlain until 10% sucrose layer was pushed above the marked line. The syringe was wiped with a Kimwipe prior to addition of 50% sucrose buffer to maintain separation between buffers. Black caps were added carefully to prevent bubbles to each ultracentrifuge tube. The Biocomp gradient master was then used at the following conditions: Long Cap 10% - 50% WV Step 1, 1:50 minutes, 80^{o} angle, 21 speed. Gradients were then sealed with parafilm and incubated at 4^{o}C overnight. Gradients were then balanced to within 10mg of each other. Normalized cell lysates were added (500uL volume) and spun in a SW41 ultracentrifuge rotor at 38,000rpm for 2 hours at 4^{o}C. 60% sucrose was then used to fractionate spun lysates into 1mL fractions and polysome peaks were measured with a Combi Flash UV-vis detector (Brandel) and TracerDAQ software. Polysome fractions were then pooled into appropriate groups: highly translated (Higher than 3 ribosomes, past the 1st peak), and lowly translated (1-2 ribosomes and 80s) based on A280 UV peaks. The pooled fractions were then incubated with 3:1 Trizol LS Reagent, vortexed thoroughly, and incubated at RT for 5 minutes. RNA was then extracted following the instructions of the Direct-zol Miniprep Ki (Zymo Research), and eluted in 50uL. RNA was quantified and normalized for input into either tRNACapture-seq qPCR with 5S, $tRNA^{Ile}_{GAU}$, or $tRNA^{Ile}_{UAU}$ probes (250ng) or as Input into the QuantSeq 3′ mRNA-Seq Library Prep Kit (Lexogen) kit. 500ng RNA was used as input and samples were processed according to QuantSeq (Lexogen) instructions. A pooled library was compiled using manufacturer's primers and 10nM Pool was quality checked with Tapestation and

sequenced on the NextSeq High Output 75 Single Read at the Rockefeller University Genomics Resource Center.

Proteomics

Cells were lysed in 20mM Tris HCl pH 8.0, 1% NP-40, 2mM EDTA with 1x protease inhibitors (Roche). 50ug lysate was used for label free quantification at the Rockefeller University Proteomics Core Facility.

Immunofluorescence of Histology Sections

Paraffin embedded histology slides from metastatic nodules were used. Slides underwent deparaffination via 5-minute incubations in xylene 2x, 100% Ethanol, 2x, 70% Ethanol, 50% Ethanol, and subsequently 1x PBS. Antigen retrieval was performed with 1x Citrate Buffer pH 6.0 in a microwave for 20 minutes. Slides were cooled to room temperature, then tissue regions were isolated with a PAP pen. Slides were then blocked with 10% Goat Serum (Sigma Aldrich) for 30 minutes at room temperature. Primary antibodies were incubated overnight at 4^{o}C in a moist chamber (Vimentin V9 mouse (Abcam ab8069) 1:50), or for 2 hours at room temperature (Ki67 (Abcam ab927420) 1:200). Slides were washed with 0.5% Tween 20 PBS then incubated with secondary antibody for 1 hour at RT (1:200). Slides were then stained with DAPI for 5 minutes, and sealed with Prolong Gold anti-fade solution (Thermo Fisher). Fluorescent intensity was measured on Inverted TCS SP8 laser scanning confocal microscope (Leica) at the Bioimaging Resource Center at Rockefeller University and quantified by number of positive cells per field of view. Quantification was performed blind.

In Vitro Growth Assays

Cells at visual equal confluency were resuspended in new DMEM media and counted with a hemacytometer. Cells were then seeded in equal numbers (100K for stress conditions, 50K for normal in vitro conditions) in 6 well plates in triplicate. Cells were

then counted at endpoint day with a hemacytometer. Each experiment was conducted three times. Cells treated with 200uM H202 were counted on Day 3. Cells exposed to 0.5% hypoxia in an InvivO2 chamber (Baker Ruskinn) were counted on Day 3 or 4. Growth assays in normal in vitro conditions were counted on Day 5.

Cell Viability Assays

For all cell lines, 2x103 cells/well were seeded in triplicate a 96-well plate and allowed to adhere for 24 hr. The following day, media was aspirated and replaced with fresh media and cells were placed into a 0.5% O2 hypoxic chamber (INVIVO) for 4 days. After, the media was aspirated and replaced with 100 µL phenol-red free DMEM (GIBCO) and 12mM 3-[4,5-Dimethylthiazol-2-yl]-2,5-diphenyltetrazolium (MTT) (Thermo Fisher Scientific, #M6494) was added to the cells. After 4 hr, the media containing MTT was aspirated and 50 µL DMSO was added to dissolve the formazan and read at 540nm.

Codon Reporters

Wildtype or codon mutant SMNDC1 (all AUA changed to AUC) coding sequence gene blocks were designed with NheI & XhoI restriction sites and a N-terminal flag tag and ordered from IDT. SMDNC1 gene blocks were cloned into the psiCheck 2 vector. The firefly luciferase was removed and replaced with a renilla luciferase with only AUU encoding isoleucines via restriction cutting with PspOMI & XbaI. This adapted SMNDC1 reporter was transfected with 2.5ug plasmid and 10uL Lipofectamine 2000 (Thermo Fisher) in triplicate of MDA 231 cells with modulated $tRNA^{Ile}$ levels. Cells were lysed after 24 hours and protein was extracted with RIPA buffer with 1x protease inhibitors EDTA-free (Roche). Protein expression was measured via LICOR Western as described below.

RSCU and Pathway Enrichment Analyses

Gene filtering: The Homo sapiens GRCh38 CDS sequences were downloaded from the Ensembl database. To avoid multiple splice variants from the same gene affecting downstream analysis, principle splice isoforms were filtered using annotations from the APPRIS database and a custom Python script. For genes with multiple annotated isoforms, the transcript with the highest score was chosen as the representative.

RSCU calculation: To calculate the relative synonymous codon usage (RSCU) for a given codon in each gene, we first calculated the total abundances of each codon across our entire filtered CDS dataset and to determine the empiric distribution of synonymous codon usage for each amino acid. For each gene, the RSCU score was calculated as: [Observed_Codon_Usage – Expected_Codon_Usage] / Expected_codon_usage. The expected codon usage was defined as Observed_Amino_Acid_Usage * Pr(Codon_Usage | Amino_Acid) where the probability mass function was determined using the empiric codon distribution described above. For genes/transcripts in which a given amino acid appeared zero times, the RSCU score was set to 0.

Mutual Information/Pathway Enrichment: Genes were ranked by the RSCU score calculated above. Mutual information analyses to detected significantly over-represented and under-represented pathways in discrete bins were performed using the iPAGE mutual information framework with pathway annotations built from the Reactome database[107]. Heatmaps were generated with iPAGE. To determine pathways that were most likely to be divergently modulated by AUA or AUC over/under-expression, we additionally filtered the output to include pathway enrichments/depletions present in both AUC and AUA analyses with p value less than 10E-3 in the highest RSCU bin. Heatmaps were generated using Python software and the seaborn package.

Databases/Sites/Software used:

Ensembl: https://useast.ensembl.org/index.html

APPRIS: http://appris-tools.org/#/

iPAGE: https://tavazoielab.c2b2.columbia.edu/iPAGE/

Reactome: https://reactome.org

Python 3.6.0: https://www.python.org

Pandas: https://pandas.pydata.org

Seaborn: https://seaborn.pydata.org

Statistical analysis

Results are presented in dot-plot with dots representing individual values and bar-charts depicting average values with standard error of the mean (±s.e.m.). The number of samples for each group was chosen based on the expected levels of variation and consistency. Experiments were performed in a blinded fashion. Unless otherwise stated, statistical significance was assessed by a two-tailed Student's's t-test with P-value < 0.05 being considered statistically significant.

Table M.1 | Primer Sequences

Name	Sequence
CKB F	TGAGTTCATGTGGAACCCTCACCT
CKB R	AACTTCTCATGCTTGCCCAGGTTG
EPHX1 F	CTTTGCCATCTACTGGTTCATCT
EPHX1 R	TCTCCTCATCTGACGTTTCCA
GAPDH F	AGC CAC ATC GCT CAG ACA C
GAPDH R	GCC CAA TAC GAC CAA ATC C
LSM6 F	AAAGCAAATCATCGGACGACC
LSM6 R	GTACAACACATTGTTTCCTCGGA
PYCARD F	TGGATGCTCTGTACGGGAAG
PYCARD R	CCAGGCTGGTGTGAAACTGAA
SIL1 F	CTGCCTTCATCTAGGATGGCT
SIL1 R	GGGTTGGTCAGGGCAAACTC
SMNDC1 F	AGCGGAGATTGAGGAGATAGATG
SMNDC1 R	GGTTCAACAGTGGAGTCACTTC
mouse CKB Forward	AGTTCCCTGATCTGAGCAGC
mouse CKB Reverse	TTACTTTGGACGACGCCATTC
mouse GAPDH F	GAGAGTGTTTCCTCGTCCCG
mouse GADPH R	ACTGTGCCGTTGAATTTGCC
N terminal 19 del CKB F	GGGGACAAGTTTGTACAAAAAAGCAGGCTATGTTCCCCGACCTGAGCGCCCA
mouse CKB F	GGGGACAAGTTTGTACAAAAAAGCAGGCTATGCCCTTCTCCAACA
mouse CKB R	GGGGACCACTTTGTACAAGAAAGCTGGGTCTGCCTTCTGGGCCGGCATGAG
S6A CKB Mutagenesis F	CTTCAGTGCCTTGTGGGCCTTGGAGAAGGGCATG
S6A CKB Mutagenesis R	CATGCCCTTCTCCAACGCCCACAACGCACTGAAG
mouse S6A CKB Mutagenesis F	AGCTTCTGCGTATTATGGGCGTTGGAGAAGGGCATAGC
mouse S6A CKB Mutagenesis R	GCTATGCCCTTCTCCAACGCCCATAATACGCAGAAGCT
S4A CKB Mutagenesis F	GTTGGCATGCCCTTCGCCAACAGCCACAACG
S4A CKB Mutagenesis R	CGTTGTGGCTGTTGGCGAAGGCGATGCCAAC
R13A CKB Mutagenesis F	CTCGGCCGGGAAGGCCAGCTTCAGTGCG

R13A CKB Mutagenesis R	CGCACTGAAGCTGGCCTTCCCGGCCGAG
P2A CKB Mutagenesis F	GTGGCTGTTGGAGAAGGCCATGCCAACTTTTTTGT
P2A CKB Mutagenesis R	ACAAAAAAGTTGGCATGGCCTTCTCCAACAGCCAC
K11A CKB Mutagenesis F	CCGGGAAGCCGAGCGCCAGTGCGTTGTGGC
K11A CKB Mutagenesis R	GCCACAACGCACTGGCGCTGCGCTTCCCGG
genomic tRNAArg F	GTGCTATATAAGCATCTGTCTTTGG
genomic tRNAArg R	AAACGACGACCACGAAGG
genomic tRNAGlu F	TGGTCTAGTGGCTAGGATTCG
genomic tRNAGlu R	GGGAATCGAACCCGGGCCGCG
genomic tRNALeu F	GAGGACAACGGGGACACAA
genomic tRNALeu R	TCCACCAGAAAAACTCCAGC
genomic tRNAMet F	TAGCGGCATTCACCATGT
genomic tRNAMet R	TCTCACGGCTTTGTTAGACAC
genomic tRNAIle UAU 2.5 F	ATTCAGCAGAGCTCCAGTGG
genomic tRNAIle UAU 2.5 R	AAAAGGGTCTTGCTCCAGGT
genomic tRNAIle UAU 6.29 F	gaaactgggtGCTCCAGTGG
genomic tRNAIle UAU 6.29 R	TGGAAAACAATGCTCCAGGT
genomic tRNAIle UAU 6.55 F	aggaaagcatGCTCCAGTGG
genomic tRNAIle UAU 6.55 R	GAAGAAAACATGCTCCAGGT
genomic tRNAIle UAU 6.63 F	tatttctgtgGCTCCAGTGG
genomic tRNAIle UAU 6.63 R	ATAGTAAAACTGCTCCAGGT
genomic tRNAIle UAU 19.10 F	tgcggccggaGCTCCAGTGG
genomic tRNAIle UAU 19.10 R	GGAAAAAAAGTGCTCCAGGT
genomic tRNAIle GAU x.5 F	GAACACGGAGCCCTTTCA
genomic tRNAIle GAU x.5 R	CGACCATGGCGGTATCAG
genomic tRNAIle GAU x.6 F	CGAACGTGGAGCCCTTT
genomic tRNAIle GAU x.6 R	CCGCGACCTTGGTGTTAT

genomic tRNAIle AAU 6.59 F	CCTGTCATCCGGCCGGTTAG
genomic tRNAIle AAU 6.59 R	AGAGAATACTTGGCCAGTAC
genomic tRNAIle AAU 6.11 F	ggagacaggtGGCCGGTTAG
genomic tRNAIle AAU 6.11 R	AAAACAAAGTTGGCCCGTAC
genomic tRNAIle AAU 6.154 F	ttttccgggtGGCCGGTTAG
genomic tRNAIle AAU 6.154 R	AGAACCCTCGTGGCCCGTAC
genomic tRNAIle AAU 6.158 F	ccaccaaggaGGCCGGTTAG
genomic tRNAIle AAU 6.158 R	CCCACGGAAGTGGCCCGTAC
genomic tRNAIle AAU 14.10 F	aacgtcaggcGGCCGGTTAG
genomic tRNAIle AAU 14.10 R	AAAGTTAGCCTGGCCCGTAC
genomic tRNAIle AAU 17.34 F	gaaagttagtGGCCGGTTAG
genomic tRNAIle AAU 17.34 R	AGCCACCCACTGGCCCGTAC
genomic tRNAIle AAU 17.9 F	cgtagcaactGGCCGGTTAG
genomic tRNAIle AAU 17.9 R	GTTTCAATCCTGGCCCGTAC
18S F	GTAACCCGTTGAACCCCATT
18S R	CCATCCAATCGGTAGTAGCG
genomic GADPH F	GGCTGTTGTCATACTTCTCATGG
genomic GADPH R	GGAGCGAGATCCCTCCAAAAT
genomic Mycoplasma F	GGGAGCAAACAGGATTAGATACCCT
genomic Mycoplasma R	TGCACCATCTGTCACTCTGTTAACCTC
capture tRNA F	CGTGTGCTCTTCCGATCT
capture tRNA R	GATCGTCGGACTGTAGAA

Table M2 | shRNA Sequences

shRNA	Sequence
shCtrl	CCGGCAACAAGATGAAGAGCACCAACTCGAGTTGGTG CTCTTCATCTTGTTGTTTTTG
shCKB 3	CCGGCCCAGATTGAAACTCTCTTCACTCGAGTGAAGAG AGTTTCAATCTGGGTTTTTG
shCKB 60	CCGGCGAGGAGAGTTACGACGTATTCTCGAGAATACGTCGTAACTCTCCTCGTTTTTG
shCKB 63	CCGGGACGGAGTGAAACTACTCATTCTCGAGAATGAGTAGTTTCACTCCGTCTTTTTG
PYCARD 1	CCGGCGGAAGCTCTTCAGTTTCACACTCGAGTGTGAAACTGAAGAGCTTCCGTTTTTG
PYCARD 2	CCGGGAGGGTCACAAACGTTGAGTGCTCGAGCACTCAACGTTTGTGACCCTCTTTTTG
PYCARD 3	CCGGGCTTATCGCGAGGGTCACAAACTCGAGTTTGTGACCCTCGCGATAAGCTTTTTG

Table M.3 | Immune Flow Antibody Specifications

Antibody Target	Fluorophore	Company	Clone	Dilution
B220	PerCP-Cy5.5	BD Bioscience	RA3-6B2	500
B220	BUV395	BD Bioscience	RA3-6B2	400
B220	APC	BD Bioscience	RA3-6B2	400
CD103	APC	Biolegend	2E7	200
CD11b	BV605	Biolegend	M1/70	1000
CD11b	FITC	Biolegend	M1/70	1000
CD11c	PE-Cy7	Biolegend	N418	500
CD11c	FITC	Biolegend	N418	400
CD19	PB	Biolegend	1D3/CD19	200
CD24	PE	Biolegend	M1/69	4000
CD4	eVolve 605	Biolegend	GK1.5	200
CD40	PerCP-Cy5.5	Biolegend	3/23	400
CD45	BV785	Biolegend	30-F11	1000
CD49b	PE-Cy7	Biolegend	HMa2	200
CD69	PE	Biolegend	H1.F23	200
CD86	PE-Cy7	Biolegend	GL-1	4000
CD8α	AF 700	Biolegend	53-6.7	200
F4/80	FITC	Biolegend	BM8	250
F4/80	AF700	Biolegend	BM8	250
Gr1	PB	Biolegend	RB6-8C5	1000
Granzyme B	PE	Biolegend	QA16A02	500
I-A/I-E	BV421	Biolegend	M5/11.15.2	1000
IFNγ	PE-Cy7	Biolegend	XMG1.2	200
IL-10	PE	Biolegend	JES5-16E3	200
IL-12	APC	Biolegend	C15.6	200
Ly6C	BV711	Biolegend	HK1.4	3000
Ly6G	AF 700	BD Bioscience	1A8	200
NK1.1	FITC	Biolegend	PK136	200
PD-1	BV421	Biolegend	29F.1A12	50
TCRβ	APC 780	Biolegend	H57-957	200
TCRβ	PerCP-Cy5.5	Biolegend	H57-957	200
γδ TCR	PE	eBioscience	GL3	200

Table M.4 | Flow Cytometry Antibody Panels

Innate/Myeloid	
Antibody Target	Fluorophore
CD45	BV785
CD11b	BV605
TCRβ	PerCP-Cy5.5
B220	PerCP-Cy5.5
CD11c	PE-Cy7
Ly6C	BV711
Ly6G	AF 700
I-A/I-E	BV421
F4/80	FITC
CD24	PE
CD103	APC

Innate/Myeloid Activation	
Antibody Target	Fluorophore
CD45	BV785
CD11c	FITC
CD40	PerCP-Cy5.5
CD11b	BV605
CD86	PE-Cy7
CD24	PE
F4/80	AF 700
B220	BUV395

Adaptive Panel	
Antibody Target	Fluorophore
CD45	BV785
CD11b	FITC
TCRβ	APC 780
CD4	eVolve 605
CD8α	AF 700
B220	APC
CD49b	PE-Cy7
PD-1	BV421
CD69	PE

T cell Stimulation	
Antibody Target	Fluorophore
CD45	BV785
CD11b	FITC
TCRβ	APC 780
CD4	eVolve 605
CD8α	AF 700
Granzyme B	PE
IFNγ	PE-Cy7

Lymph Node	
Antibody Target	Fluorophore
CD45	BV785
CD11b	BV605
TCRβ	APC 780
B220	BUV395

I-A/I-E	BV421
CD11c	FITC
F4/80	AF700
CD24	PE
CD103	APC
CD86	PE-Cy7
CD40	PerCP-Cy5.5

M.5 Flow Cytometry Gating Strategies

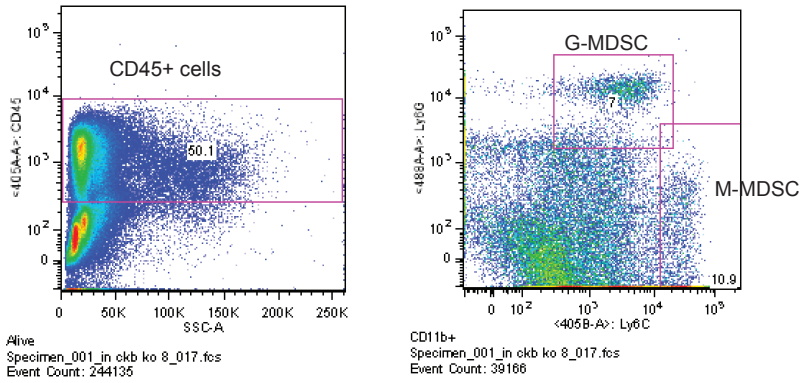

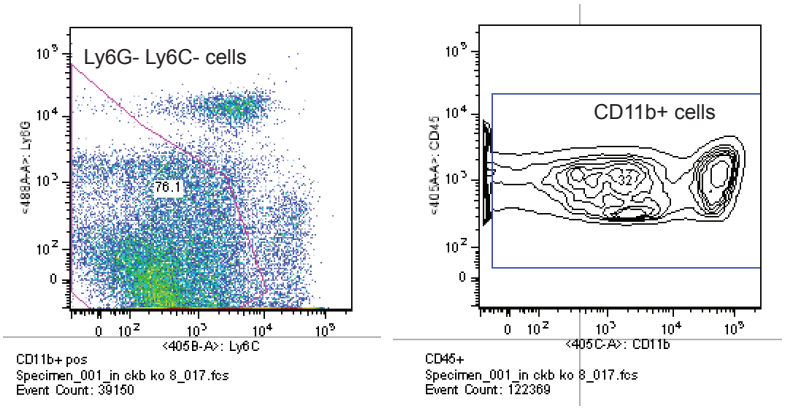

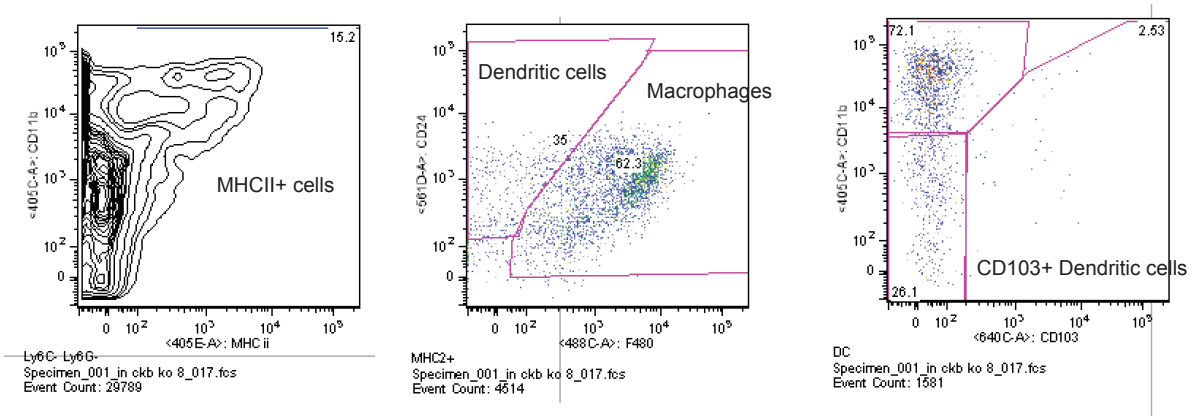

Myeloid and Innate Gating

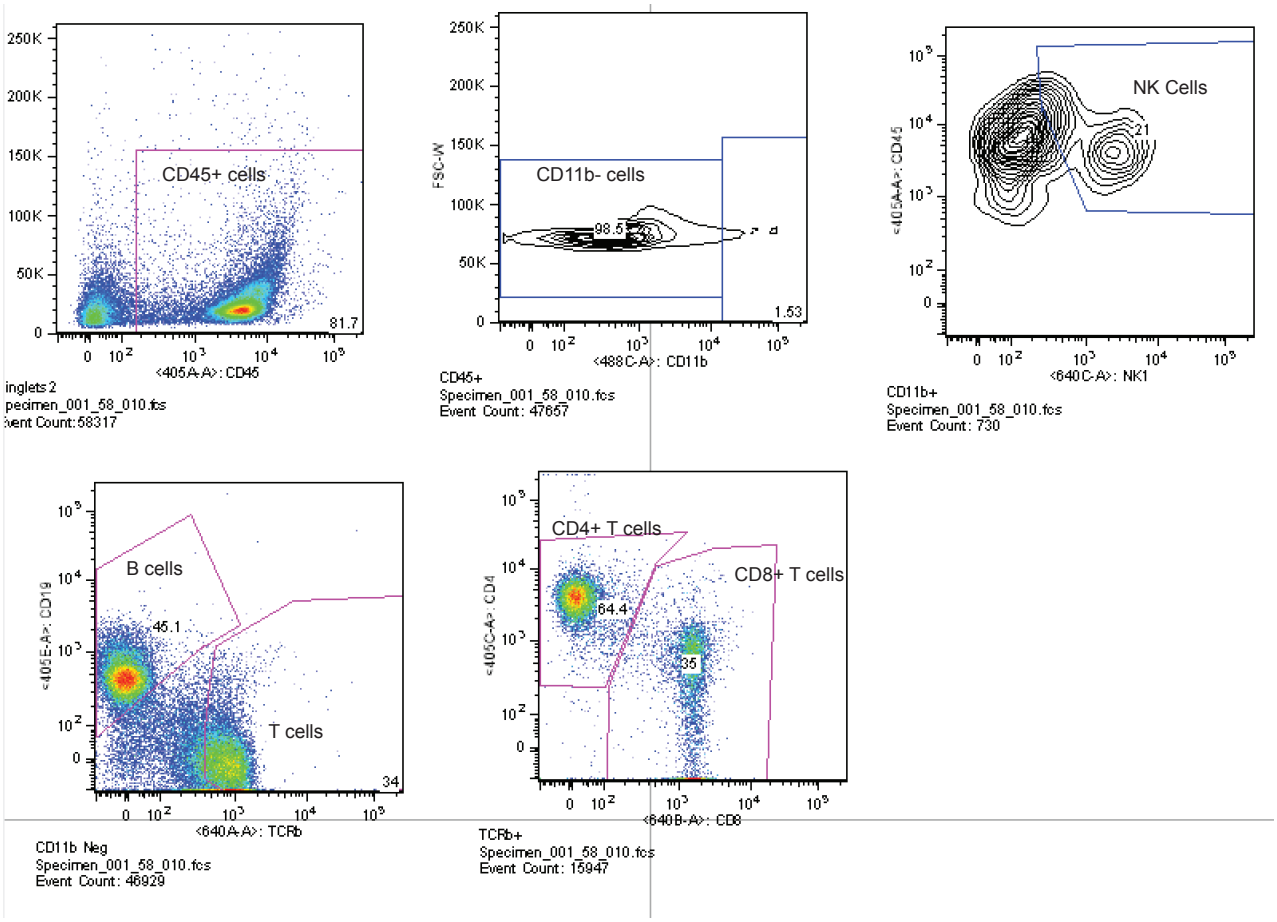

Adaptive Gating

References

1 Siegel, R. L., Miller, K. D. & Jemal, A. Cancer statistics, 2019. CA Cancer J Clin 69, 7-34, doi:10.3322/caac.21551 (2019).

2 Heinemann, V. et al. FOLFIRI plus cetuximab versus FOLFIRI plus bevacizumab as first-line treatment for patients with metastatic colorectal cancer (FIRE-3): a randomised, open-label, phase 3 trial. Lancet Oncol 15, 1065-1075, doi:10.1016/S1470-2045(14)70330-4 (2014).

3 Conroy, T. et al. FOLFIRINOX versus gemcitabine for metastatic pancreatic cancer. N Engl J Med 364, 1817-1825, doi:10.1056/NEJMoa1011923 (2011).

4 Normanno, N. et al. Heterogeneity of KRAS, NRAS, BRAF and PIK3CA mutations in metastatic colorectal cancer and potential effects on therapy in the CAPRI GOIM trial. Ann Oncol 26, 1710-1714, doi:10.1093/annonc/mdv176 (2015).

5 Lee, K. H., Kim, J. S., Lee, C. S. & Kim, J. Y. KRAS discordance between primary and recurrent tumors after radical resection of colorectal cancers. J Surg Oncol 111, 1059-1064, doi:10.1002/jso.23936 (2015).

6 Simmonds, P. C. et al. Surgical resection of hepatic metastases from colorectal cancer: a systematic review of published studies. Br J Cancer 94, 982-999, doi:10.1038/sj.bjc.6603033 (2006).

7 Cummings, L. C., Payes, J. D. & Cooper, G. S. Survival after hepatic resection in metastatic colorectal cancer: a population-based study. Cancer 109, 718-726, doi:10.1002/cncr.22448 (2007).

8 Rees, M., Tekkis, P. P., Welsh, F. K., O'Rourke, T. & John, T. G. Evaluation of long-term survival after hepatic resection for metastatic colorectal cancer: a multifactorial model of 929 patients. Ann Surg 247, 125-135, doi:10.1097/SLA.0b013e31815aa2c2 (2008).

9 Ferrarotto, R. et al. Durable complete responses in metastatic colorectal cancer treated with chemotherapy alone. Clin Colorectal Cancer 10, 178-182, doi:10.1016/j.clcc.2011.03.023 (2011).

10 Reddy, S. K. et al. Timing of multimodality therapy for resectable synchronous colorectal liver metastases: a retrospective multi-institutional analysis. Ann Surg Oncol 16, 1809-1819, doi:10.1245/s10434-008-0181-y (2009).

11 Dobry, A. S. et al. Management of metastatic melanoma: improved survival in a national cohort following the approvals of checkpoint blockade immunotherapies and targeted therapies. Cancer Immunol Immunother 67, 1833-1844, doi:10.1007/s00262-018-2241-x (2018).

12 Hodi, F. S. et al. Improved survival with ipilimumab in patients with metastatic melanoma. N Engl J Med 363, 711-723, doi:10.1056/NEJMoa1003466 (2010).

13 Peggs, K. S., Quezada, S. A., Chambers, C. A., Korman, A. J. & Allison, J. P. Blockade of CTLA-4 on both effector and regulatory T cell compartments contributes to the antitumor activity of anti-CTLA-4 antibodies. J Exp Med 206, 1717-1725, doi:10.1084/jem.20082492 (2009).

14 Alexandrov, L. B. et al. Signatures of mutational processes in human cancer. Nature 500, 415-421, doi:10.1038/nature12477 (2013).

15 Le, D. T. et al. PD-1 Blockade in Tumors with Mismatch-Repair Deficiency. N Engl J Med 372, 2509-2520, doi:10.1056/NEJMoa1500596 (2015).

16 Martinez-Bosch, N., Vinaixa, J. & Navarro, P. Immune Evasion in Pancreatic Cancer: From Mechanisms to Therapy. Cancers (Basel) 10, doi:10.3390/cancers10010006 (2018).

17 Blando, J. et al. Comparison of immune infiltrates in melanoma and pancreatic cancer highlights VISTA as a potential target in pancreatic cancer. Proc Natl Acad Sci U S A 116, 1692-1697, doi:10.1073/pnas.1811067116 (2019).

18 Balachandran, V. P. et al. Identification of unique neoantigen qualities in long-term survivors of pancreatic cancer. Nature 551, 512-516, doi:10.1038/nature24462 (2017).

19 Winograd, R. et al. Induction of T-cell Immunity Overcomes Complete Resistance to PD-1 and CTLA-4 Blockade and Improves Survival in Pancreatic Carcinoma. Cancer Immunol Res 3, 399-411, doi:10.1158/2326-6066.CIR-14-0215 (2015).

20 Dar, T. B., Henson, R. M. & Shiao, S. L. Targeting Innate Immunity to Enhance the Efficacy of Radiation Therapy. Front Immunol 9, 3077, doi:10.3389/fimmu.2018.03077 (2018).

21 Walle, T. et al. Radiation effects on antitumor immune responses: current perspectives and challenges. Ther Adv Med Oncol 10, 1758834017742575, doi:10.1177/1758834017742575 (2018).

22 Shabason, J. E. & Minn, A. J. Radiation and Immune Checkpoint Blockade: From Bench to Clinic. Semin Radiat Oncol 27, 289-298, doi:10.1016/j.semradonc.2017.03.002 (2017).

23 Greenberg, P. A. et al. Long-term follow-up of patients with complete remission following combination chemotherapy for metastatic breast cancer. J Clin Oncol 14, 2197-2205, doi:10.1200/JCO.1996.14.8.2197 (1996).

24 Gennari, A., Conte, P., Rosso, R., Orlandini, C. & Bruzzi, P. Survival of metastatic breast carcinoma patients over a 20-year period: a retrospective analysis based on individual

patient data from six consecutive studies. Cancer 104, 1742-1750, doi:10.1002/cncr.21359 (2005).

25 Chia, S. K. et al. The impact of new chemotherapeutic and hormone agents on survival in a population-based cohort of women with metastatic breast cancer. Cancer 110, 973-979, doi:10.1002/cncr.22867 (2007).

26 Hudis, C. A. & Gianni, L. Triple-negative breast cancer: an unmet medical need. Oncologist 16 Suppl 1, 1-11, doi:10.1634/theoncologist.2011-S1-01 (2011).

27 Schmid, P. et al. Atezolizumab and Nab-Paclitaxel in Advanced Triple-Negative Breast Cancer. N Engl J Med 379, 2108-2121, doi:10.1056/NEJMoa1809615 (2018).

28 Lien, E. C., Lyssiotis, C. A. & Cantley, L. C. Metabolic Reprogramming by the PI3K-Akt-mTOR Pathway in Cancer. Recent Results Cancer Res 207, 39-72, doi:10.1007/978-3-319-42118-6_3 (2016).

29 Hanahan, D. & Weinberg, R. A. Hallmarks of cancer: the next generation. Cell 144, 646-674, doi:10.1016/j.cell.2011.02.013 (2011).

30 Dow, L. E. et al. Apc Restoration Promotes Cellular Differentiation and Reestablishes Crypt Homeostasis in Colorectal Cancer. Cell 161, 1539-1552, doi:10.1016/j.cell.2015.05.033 (2015).

31 Manguso, R. T. et al. In vivo CRISPR screening identifies Ptpn2 as a cancer immunotherapy target. Nature 547, 413-418, doi:10.1038/nature23270 (2017).

32 van der Weyden, L. et al. Genome-wide in vivo screen identifies novel host regulators of metastatic colonization. Nature 541, 233-236, doi:10.1038/nature20792 (2017).

33 Fidler, I. J. Selection of successive tumour lines for metastasis. Nat New Biol 242, 148-149 (1973).

34 Lujambio, A. & Lowe, S. W. The microcosmos of cancer. Nature 482, 347-355, doi:10.1038/nature10888 (2012).

35 Ma, L., Teruya-Feldstein, J. & Weinberg, R. A. Tumour invasion and metastasis initiated by microRNA-10b in breast cancer. Nature 449, 682-688, doi:10.1038/nature06174 (2007).

36 Pencheva, N. & Tavazoie, S. F. Control of metastatic progression by microRNA regulatory networks. Nat Cell Biol 15, 546-554, doi:10.1038/ncb2769 (2013).

37 Pencheva, N. et al. Convergent multi-miRNA targeting of ApoE drives LRP1/LRP8-dependent melanoma metastasis and angiogenesis. Cell 151, 1068-1082, doi:10.1016/j.cell.2012.10.028 (2012).

38 Png, K. J., Halberg, N., Yoshida, M. & Tavazoie, S. F. A microRNA regulon that mediates endothelial recruitment and metastasis by cancer cells. Nature 481, 190-194, doi:10.1038/nature10661 (2011).

39 Nguyen, A., Yoshida, M., Goodarzi, H. & Tavazoie, S. F. Highly variable cancer subpopulations that exhibit enhanced transcriptome variability and metastatic fitness. Nat Commun 7, 11246, doi:10.1038/ncomms11246 (2016).

40 Kumar, V., Patel, S., Tcyganov, E. & Gabrilovich, D. I. The Nature of Myeloid-Derived Suppressor Cells in the Tumor Microenvironment. Trends Immunol 37, 208-220, doi:10.1016/j.it.2016.01.004 (2016).

41 Ouzounova, M. et al. Monocytic and granulocytic myeloid derived suppressor cells differentially regulate spatiotemporal tumour plasticity during metastatic cascade. Nat Commun 8, 14979, doi:10.1038/ncomms14979 (2017).

42 Ortiz, A. et al. An Interferon-Driven Oxysterol-Based Defense against Tumor-Derived Extracellular Vesicles. Cancer Cell 35, 33-45 e36, doi:10.1016/j.ccell.2018.12.001 (2019).

43 Kitamura, T., Qian, B. Z. & Pollard, J. W. Immune cell promotion of metastasis. Nat Rev Immunol 15, 73-86, doi:10.1038/nri3789 (2015).

44 Tavazoie, M. F. et al. LXR/ApoE Activation Restricts Innate Immune Suppression in Cancer. Cell 172, 825-840 e818, doi:10.1016/j.cell.2017.12.026 (2018).

45 Broz, M. L. et al. Dissecting the Tumor Myeloid Compartment Reveals Rare Activating Antigen-Presenting Cells Critical for T Cell Immunity. Cancer Cell 26, 938, doi:10.1016/j.ccell.2014.11.010 (2014).

46 Salmon, H. et al. Expansion and Activation of CD103(+) Dendritic Cell Progenitors at the Tumor Site Enhances Tumor Responses to Therapeutic PD-L1 and BRAF Inhibition. Immunity 44, 924-938, doi:10.1016/j.immuni.2016.03.012 (2016).

47 Gardner, A. & Ruffell, B. Dendritic Cells and Cancer Immunity. Trends Immunol 37, 855-865, doi:10.1016/j.it.2016.09.006 (2016).

48 Jin, K. et al. Mechanisms regulating colorectal cancer cell metastasis into liver (Review). Oncol Lett 3, 11-15, doi:10.3892/ol.2011.432 (2012).

49 Nguyen, A. et al. PKLR promotes colorectal cancer liver colonization through induction of glutathione synthesis. J Clin Invest 126, 681-694, doi:10.1172/JCI83587 (2016).

50 Gill, J. G., Piskounova, E. & Morrison, S. J. Cancer, Oxidative Stress, and Metastasis. Cold Spring Harb Symp Quant Biol 81, 163-175, doi:10.1101/sqb.2016.81.030791 (2016).

51 Piskounova, E. et al. Oxidative stress inhibits distant metastasis by human melanoma cells. Nature 527, 186-191, doi:10.1038/nature15726 (2015).

52 Loo, J. M. et al. Extracellular metabolic energetics can promote cancer progression. Cell 160, 393-406, doi:10.1016/j.cell.2014.12.018 (2015).

53 Bertout, J. A., Patel, S. A. & Simon, M. C. The impact of O2 availability on human cancer. Nat Rev Cancer 8, 967-975, doi:10.1038/nrc2540 (2008).

54 Semenza, G. L. HIF-1 mediates metabolic responses to intratumoral hypoxia and oncogenic mutations. J Clin Invest 123, 3664-3671, doi:10.1172/JCI67230 (2013).

55 Wheaton, W. W. & Chandel, N. S. Hypoxia. 2. Hypoxia regulates cellular metabolism. Am J Physiol Cell Physiol 300, C385-393, doi:10.1152/ajpcell.00485.2010 (2011).

56 Pellegatti, P. et al. Increased level of extracellular ATP at tumor sites: in vivo imaging with plasma membrane luciferase. PLoS One 3, e2599, doi:10.1371/journal.pone.0002599 (2008).

57 Stagg, J. & Smyth, M. J. Extracellular adenosine triphosphate and adenosine in cancer. Oncogene 29, 5346-5358, doi:10.1038/onc.2010.292 (2010).

58 Gorini, S., Gatta, L., Pontecorvo, L., Vitiello, L. & la Sala, A. Regulation of innate immunity by extracellular nucleotides. Am J Blood Res 3, 14-28 (2013).

59 Beavis, P. A., Stagg, J., Darcy, P. K. & Smyth, M. J. CD73: a potent suppressor of antitumor immune responses. Trends Immunol 33, 231-237, doi:10.1016/j.it.2012.02.009 (2012).

60 Tavazoie, S. F. et al. Endogenous human microRNAs that suppress breast cancer metastasis. Nature 451, 147-152, doi:10.1038/nature06487 (2008).

61 Fish, L. et al. Muscleblind-like 1 suppresses breast cancer metastatic colonization and stabilizes metastasis suppressor transcripts. Genes Dev 30, 386-398, doi:10.1101/gad.270645.115 (2016).

62 Halberg, N., Alarcon, C. & Tavazoie, S. F. microRNA regulation of cancer-endothelial interactions: vesicular microRNAs on the move. EMBO J 31, 3509-3510, doi:10.1038/emboj.2012.198 (2012).

63 Halberg, N. et al. PITPNC1 Recruits RAB1B to the Golgi Network to Drive Malignant Secretion. Cancer Cell 29, 339-353, doi:10.1016/j.ccell.2016.02.013 (2016).

64 Lee, H., Goodarzi, H., Tavazoie, S. F. & Alarcon, C. R. TMEM2 Is a SOX4-Regulated Gene That Mediates Metastatic Migration and Invasion in Breast Cancer. Cancer Res 76, 4994-5005, doi:10.1158/0008-5472.CAN-15-2322 (2016).

65 Png, K. J. et al. MicroRNA-335 inhibits tumor reinitiation and is silenced through genetic and epigenetic mechanisms in human breast cancer. Genes Dev 25, 226-231, doi:10.1101/gad.1974211 (2011).

66 Sengelaub, C. A., Navrazhina, K., Ross, J. B., Halberg, N. & Tavazoie, S. F. PTPRN2 and PLCbeta1 promote metastatic breast cancer cell migration through PI(4,5)P2-dependent actin remodeling. EMBO J 35, 62-76, doi:10.15252/embj.201591973 (2016).

67 Goodarzi, H. et al. Endogenous tRNA-Derived Fragments Suppress Breast Cancer Progression via YBX1 Displacement. Cell 161, 790-802, doi:10.1016/j.cell.2015.02.053 (2015).

68 Goncalves, K. A. et al. Angiogenin Promotes Hematopoietic Regeneration by Dichotomously Regulating Quiescence of Stem and Progenitor Cells. Cell 166, 894-906, doi:10.1016/j.cell.2016.06.042 (2016).

69 Thompson, D. M., Lu, C., Green, P. J. & Parker, R. tRNA cleavage is a conserved response to oxidative stress in eukaryotes. RNA 14, 2095-2103, doi:10.1261/rna.1232808 (2008).

70 Lee, S. R. & Collins, K. Starvation-induced cleavage of the tRNA anticodon loop in Tetrahymena thermophila. J Biol Chem 280, 42744-42749, doi:10.1074/jbc.M510356200 (2005).

71 Mohr, S. et al. Thermostable group II intron reverse transcriptase fusion proteins and their use in cDNA synthesis and next-generation RNA sequencing. RNA 19, 958-970, doi:10.1261/rna.039743.113 (2013).

72 Goodarzi, H. et al. Modulated Expression of Specific tRNAs Drives Gene Expression and Cancer Progression. Cell 165, 1416-1427, doi:10.1016/j.cell.2016.05.046 (2016).

73 Zheng, G. et al. Efficient and quantitative high-throughput tRNA sequencing. Nat Methods 12, 835-837, doi:10.1038/nmeth.3478 (2015).

74 Ogle, J. M., Carter, A. P. & Ramakrishnan, V. Insights into the decoding mechanism from recent ribosome structures. Trends Biochem Sci 28, 259-266, doi:10.1016/S0968-0004(03)00066-5 (2003).

75 Schmeing, T. M. & Ramakrishnan, V. What recent ribosome structures have revealed about the mechanism of translation. Nature 461, 1234-1242, doi:10.1038/nature08403 (2009).

76 Pavon-Eternod, M. et al. tRNA over-expression in breast cancer and functional consequences. Nucleic Acids Res 37, 7268-7280, doi:10.1093/nar/gkp787 (2009).

77 Gingold, H. et al. A dual program for translation regulation in cellular proliferation and differentiation. Cell 158, 1281-1292, doi:10.1016/j.cell.2014.08.011 (2014).

78 Vo, M. N. et al. ANKRD16 prevents neuron loss caused by an editing-defective tRNA synthetase. Nature 557, 510-515, doi:10.1038/s41586-018-0137-8 (2018).

79 Knott, S. R. V. et al. Asparagine bioavailability governs metastasis in a model of breast cancer. Nature 554, 378-381, doi:10.1038/nature25465 (2018).

80 Loayza-Puch, F. et al. Tumour-specific proline vulnerability uncovered by differential ribosome codon reading. Nature 530, 490-494, doi:10.1038/nature16982 (2016).

81 Lee, J. W., Komar, C. A., Bengsch, F., Graham, K. & Beatty, G. L. Genetically Engineered Mouse Models of Pancreatic Cancer: The KPC Model (LSL-Kras(G12D/+) ;LSL-Trp53(R172H/+) ;Pdx-1-Cre), Its Variants, and Their Application in Immuno-oncology Drug Discovery. Curr Protoc Pharmacol 73, 14 39 11-14 39 20, doi:10.1002/cpph.2 (2016).

82 Hingorani, S. R. et al. Trp53R172H and KrasG12D cooperate to promote chromosomal instability and widely metastatic pancreatic ductal adenocarcinoma in mice. Cancer Cell 7, 469-483, doi:10.1016/j.ccr.2005.04.023 (2005).

83 Woo, S. R., Corrales, L. & Gajewski, T. F. Innate immune recognition of cancer. Annu Rev Immunol 33, 445-474, doi:10.1146/annurev-immunol-032414-112043 (2015).

84 Aymeric, L. et al. Tumor cell death and ATP release prime dendritic cells and efficient anticancer immunity. Cancer Res 70, 855-858, doi:10.1158/0008-5472.CAN-09-3566 (2010).

85 Pellegatti, P., Falzoni, S., Pinton, P., Rizzuto, R. & Di Virgilio, F. A novel recombinant plasma membrane-targeted luciferase reveals a new pathway for ATP secretion. Mol Biol Cell 16, 3659-3665, doi:10.1091/mbc.e05-03-0222 (2005).

86 Schnurr, M. et al. Extracellular ATP and TNF-alpha synergize in the activation and maturation of human dendritic cells. J Immunol 165, 4704-4709 (2000).

87 Loo, J. Extracellular Metabolic Energetics Can Promote Cancer Progression 308 thesis, (2016).

88 Cocucci, E. & Meldolesi, J. Ectosomes and exosomes: shedding the confusion between extracellular vesicles. Trends Cell Biol 25, 364-372, doi:10.1016/j.tcb.2015.01.004 (2015).

89 Chen, Y. H. et al. Phosphatidylserine vesicles enable efficient en bloc transmission of enteroviruses. Cell 160, 619-630, doi:10.1016/j.cell.2015.01.032 (2015).

90 Hou, S. et al. Membrane phospholipid redistribution in cancer micro-particles and implications in the recruitment of cationic protein factors. J Extracell Vesicles 3, doi:10.3402/jev.v3.22653 (2014).

91 Sadallah, S., Eken, C., Martin, P. J. & Schifferli, J. A. Microparticles (ectosomes) shed by stored human platelets downregulate macrophages and modify the development of dendritic cells. J Immunol 186, 6543-6552, doi:10.4049/jimmunol.1002788 (2011).

92 Lima, L. G., Chammas, R., Monteiro, R. Q., Moreira, M. E. & Barcinski, M. A. Tumor-derived microvesicles modulate the establishment of metastatic melanoma in a phosphatidylserine-dependent manner. Cancer Lett 283, 168-175, doi:10.1016/j.canlet.2009.03.041 (2009).

93 McGlincy, N. J. & Ingolia, N. T. Transcriptome-wide measurement of translation by ribosome profiling. Methods 126, 112-129, doi:10.1016/j.ymeth.2017.05.028 (2017).

94 Katibah, G. E. et al. Broad and adaptable RNA structure recognition by the human interferon-induced tetratricopeptide repeat protein IFIT5. Proc Natl Acad Sci U S A 111, 12025-12030, doi:10.1073/pnas.1412842111 (2014).

95 Goodarzi, H., Elemento, O. & Tavazoie, S. Revealing global regulatory perturbations across human cancers. Mol Cell 36, 900-911, doi:10.1016/j.molcel.2009.11.016 (2009).

96 Zhang, Y., Li, H., Wang, X., Gao, X. & Liu, X. Regulation of T cell development and activation by creatine kinase B. PLoS One 4, e5000, doi:10.1371/journal.pone.0005000 (2009).

97 Agris, P. F. et al. Celebrating wobble decoding: Half a century and still much is new. RNA Biol 15, 537-553, doi:10.1080/15476286.2017.1356562 (2018).

98 Rozov, A. et al. Novel base-pairing interactions at the tRNA wobble position crucial for accurate reading of the genetic code. Nat Commun 7, 10457, doi:10.1038/ncomms10457 (2016).

99 Voorhees, R. M. et al. The structural basis for specific decoding of AUA by isoleucine tRNA on the ribosome. Nat Struct Mol Biol 20, 641-643, doi:10.1038/nsmb.2545 (2013).

100 Yokoyama, S. N., S. in tRNA: Structure, Biosynthesis and Function (ed D. Söll and U. RajBhandary) 207-223 (1995).

101 Stewart, S. A. et al. Lentivirus-delivered stable gene silencing by RNAi in primary cells. RNA 9, 493-501 (2003).

102 Bryant, D. M. et al. A molecular network for de novo generation of the apical surface and lumen. Nat Cell Biol 12, 1035-1045, doi:10.1038/ncb2106 (2010).

103 Chen, B. et al. Dynamic imaging of genomic loci in living human cells by an optimized CRISPR/Cas system. Cell 155, 1479-1491, doi:10.1016/j.cell.2013.12.001 (2013).

104 Yeo, N. C. et al. An enhanced CRISPR repressor for targeted mammalian gene regulation. Nat Methods 15, 611-616, doi:10.1038/s41592-018-0048-5 (2018).

105 Chaudhuri, A. D., Yelamanchili, S. V. & Fox, H. S. Combined fluorescent in situ hybridization for detection of microRNAs and immunofluorescent labeling for cell-type markers. Front Cell Neurosci 7, 160, doi:10.3389/fncel.2013.00160 (2013).

106 Gandin, V. et al. nanoCAGE reveals 5' UTR features that define specific modes of translation of functionally related MTOR-sensitive mRNAs. Genome Res 26, 636-648, doi:10.1101/gr.197566.115 (2016).

107 Goodarzi, H., Hottes, A. K. & Tavazoie, S. Global discovery of adaptive mutations. Nat Methods 6, 581-583, doi:10.1038/nmeth.1352 (2009).